Hexacopter-based Three-dimensional Measurements of Hydrometeorological Variables and Methane

Dissertation zur Erlangung des Doktorgrades an der
Fakultät für Angewandte Informatik der
Universität Augsburg

vorgelegt von

Caroline Brosy

2018

Erstes Gutachten: Prof. Dr. Harald Kunstmann
Zweites Gutachten: PD Dr. Andreas Philipp

Tag der mündlichen Prüfung: 2. Oktober 2019

Acknowledgments

This doctoral thesis would not have been possible without the help and support of a lot of people.

First of all, I would like to say thank you so much to my supervision-team Harald Kunstmann, Klaus Schäfer, Wolfgang Junkermann and Stefan Emeis. You supported me a lot during the different phases of my PhD and you gave me the opportunity to participate in field campaigns, conferences and a research stay at the Princeton University. I learned a lot and benefited so many times from your knowledge and experiences over the years. Many thanks also to the Graduate School for Climate and Environment (GRACE) of KIT for the scholarship as well as the financial support for traveling and courses.

I would also like to thank all my colleagues from IFU who made my three years in Garmisch-Partenkirchen an unforgettable great time. My thank goes especially to Cornelius who learned to fly the UAVs to support me during the field campaign and had coffee with me whenever it was necessary. I also want to thank Sina who shared an office with me for a long time and always had a good advice when I needed one. Karina, during your master thesis you helped me a lot and I want to thank you too for all the work you have done and the time we spent together. Felix and Elija, I will miss the discussions about PhD things and everything else, thanks a lot.

My deep gratitude also goes to Mark Zondlo and Levi Golston from Princeton University as well as to the whole group I was working with during my research stay. I enjoyed the three months so much and without it the second field campaign would not have been such a success.

A big thank you to all participants of the ScaleX campaign during summer, especially to the UAV group. We spent countless hours in the field and helped each other out with advice and experience or spare parts when something had to be fixed.

Last but not least, I thank my family and friends who were always there for me when I needed them the most.

Contents

List of Figures

List of Tables

Abstract

Unmanned aerial vehicles (UAVs) gained importance in atmospheric research over the last years. They provide a suitable alternative to well-known ground-based and airborne techniques for investigations in the planetary boundary layer (PBL). This is the part of the atmosphere which is mostly and directly influenced by the characteristics of the Earth's surface including cities, forests, wetlands, agricultural areas or water. Diurnal and seasonal variations within this layer can be traced back to interactions between the heterogeneous surface and differences in the energy input from the sun. The challenge of merging local- to regional-scale measurements of atmospheric compounds in the PBL is crucial, especially for the up- and down-scaling of processes in atmospheric modeling.

UAVs were chosen as flying platforms for small-scale vertical and horizontal investigations of the lower PBL and the surface. First, the feasibility of hydrometeorological, surface and methane measurements based on multicopter-platforms were demonstrated leading to reasonable results when comparing multicopter-derived data to data acquired by instrumented towers, remote sensing methods and other airborne measurements. Based on the feasibility, two main scientific objectives were addressed: 1) investigating the applicability of multicopter-based measurements for the spatial and temporal estimation of evapotranspiration (ET) above an agricultural area and the identification of driving variables, and 2) determining the benefits of using instrumented multicopters as platforms for methane emission rates during nighttime instead of ground-based instrumentation.

These investigations of atmosphere-land surface interactions were embedded into the ScaleX campaigns in June and July 2015 and 2016, which took place at the main investigation area Fendt of the TERENO (TERrestrial ENvironmental Observatories) pre-Alpine Observatory and were organized by the Institute of Meteorology and Climate Research (IMK-IFU) of the Karlsruhe Institute of Technology (KIT). The site provided permanent instrumentation as reference and a good infrastructure for additional measurements.

With regard to the first scientific topic, estimation of *ET* rates based on multicopter data was focused. For this, horizontal variability of hydrometeorological variables was investigated above a grassland site, which was assumed to be homogeneous. In a second step, important variables for estimation of the surface energy balance were identified and finally the energy balance components including *ET* were determined. Results showed that the horizontal variability of hydrometeorological variables was mainly influenced by incoming radiation and vegetation cover. Those two were also the most important variables in estimating the energy balance. Spatial heterogeneities were observed because the measurements took place below the blending height. It could also be shown that the determination of *ET* was possible by using mainly multicopter-derived data. This allows the usage of such a system for other ecosystems and land use types without installation of instruments at the site.

The second addressed topic focused on nocturnal agricultural methane emission estimates. To this end, vertical profiles of both methane concentrations and meteorological variables were measured throughout the whole nocturnal boundary layer (NBL) at the same time. One aim was to demonstrate the benefits of using multicopter-based measurements instead of ground-based instrumentation. This led to the result that information about the whole vertical profiles within the NBL is necessary to estimate methane fluxes and that surface methane concentrations are not representative for the NBL. The other aim was to identify the influences of meteorological conditions and transport processes on nocturnal methane concentrations. Results showed that those conditions were highly affecting the estimated methane fluxes and that the combination of methane and meteorological measurements is essential for information about local and regional methane sources. The emission estimates were in the same order of magnitude as in emission inventories.

Altogether, it could be shown that multicopter platforms provide a high flexibility in application and operation for atmospheric research. This is especially the case for small-scale investigations in the lower PBL and for interrelations between land surface and atmosphere as seen on the basis of *ET* and methane emission estimates. The most important advantages of using multicopters were the flexibility of measurements with high spatial and temporal resolution as well as the repeatable investigations in stationary atmospheric conditions without influencing the ecosystem itself. The integration of additional sensors would be useful depending on scientific tasks. In addition, scale-crossing multicopter-based measurements provide data for model evaluations.

Zusammenfassung

Unbemannte Luftfahrtsysteme (UAVs) wurden in den letzten Jahren immer wichtiger für die Atmosphärenforschung. Sie stellen eine gute Alternative zu bekannten boden- und luftgestützten Techniken für die Untersuchung der planetaren Grenzschicht (PBL) dar. Dies ist der Teil der Atmosphäre, der direkt von unterschiedlichen Oberflächeneigenschaften wie Städte, Wälder, Feuchtgebiete, landwirtschaftliche Flächen, Gewässer, etc. beeinflusst wird. Tägliche und jahreszeitliche Änderungen in dieser Schicht können auf Wechselwirkungen zwischen der heterogenen Landoberfläche und der schwankenden Sonneneinstrahlung zurückgeführt werden. Die Herausforderung lokale bis regionale Messungen der Atmosphärenzusammensetzung in der PBL miteinander zu verbinden ist wesentlich für die Beschreibung skalenübergreifender Prozesse in der Modellierung.

Für kleinskalige vertikale und horizontale Untersuchungen der unteren PBL und der Erdoberfläche wurden UAVs als fliegende Messplattformen verwendet. Zunächst wurde die Machbarkeit von hydrometeorologischen, Oberflächen- und Methanmessungen mit Multikoptern demonstriert, wobei ein Vergleich zu instrumentierten Messtürmen, Fernerkundungsmethoden und anderen luftgestützten Messungen gute Ergebnisse lieferte. Darauf aufbauend wurden zwei wissenschaftliche Fragestellungen bearbeitet: 1) die Untersuchung der Anwendbarkeit von Multikoptern für die räumliche und zeitliche Abschätzung von Evapotranspiration (ET) über einer Grasfläche einschließlich der Identifikation von entscheidenden Variablen sowie 2) die Bestimmung der Vorteile der Verwendung von instrumentierten Multikoptern anstatt von bodengestützten Messinstrumenten für nächtliche Methanemissionsraten.

Diese Untersuchungen wurden in den ScaleX Kampagnen eingebettet, die im Juni und Juli 2015 und 1016 auf dem Hauptmessstandort Fendt des TERENO (TERrestrial ENvironmental Observatories) Observatoriums im Alpenvorland stattfanden und vom Institut für Meteorologie und Klimaforschung (KIT/IMK-IFU) organisiert wurden. An diesem Messstandort waren sowohl permanente Messinstrumente als Referenz als auch eine gute Infrastruktur für weitere Messungen vorhanden.

Das erste Schwerpunktthema fokussiert die Abschätzung der *ET* basierend auf Multikoptern. Hierfür wurde die Variabilität hydrometeorologischer Variablen über einer Grasfläche untersucht, die als homogen angenommen wurde. In einem zweiten Schritt konnten wichtige Variablen für die Energiebilanz identifiziert und letztendlich die Energiebilanzkomponenten einschließlich der *ET* bestimmt werden. Ergebnisse zeigten, dass die horizontale Variabilität von hydrometeorologischen Variablen am stärksten durch die einfallende Sonnenstrahlung und die Vegetationsbedeckung beeinflusst wurden. Diese beiden Variablen waren auch die wichtigsten bei der Bestimmung der Energiebilanz. Räumliche Heterogenität wurde beobachtet, weil die Messungen unterhalb der sogenannten Mischhöhe (engl. blending height) stattfanden. Außerdem konnte gezeigt werden, dass die *ET* Bestimmung mit Daten möglich ist, die vornehmlich Multikopter-basiert sind. Dies ermöglicht die Verwendung eines solchen Systems auch für andere Ökosysteme und Landnutzungsformen ohne rein bodengestützte Messinstrumente dort zu installieren.

Das zweite Schwerpunktthema befasste sich mit der Abschätzung von nächtlichen Methanemissionen aus der Landwirtschaft. Hierzu wurden die ganze Nacht lang regelmäßig Vertikalprofile von Methan und meteorologischen Variablen in der gesamten nächtlichen Grenzschicht (NBL) gemessen. Ein Ziel war es, die Vorteile von Multikoptermessungen im Gegensatz zu bodengestützten Messungen zu demonstrieren. Dies führte zu dem Ergebnis, dass Informationen über das gesamte Vertikalprofil notwendig sind, um Methanflüsse abzuschätzen, da die bodennahe Konzentration nicht repräsentativ für die NBL ist. Das andere Ziel war die Identifikation der Einflüsse meteorologischer Variablen und Transportprozesse auf die nächtliche Methankonzentration. Ergebnisse zeigten, dass atmosphärische Bedingungen die Bestimmung von Methanflüssen stark beeinflussen und die Kombination von meteorologischen und Methanmessungen wichtig für Informationen über Methanquellen ist. Die Emissionsabschätzungen waren in derselben Größenordnung wie im Emissionskataster.

Insgesamt konnte gezeigt werden, dass Multikopter eine hohe Flexibilität für die Anwendung in der Atmosphärenforschung aufweisen. Dies ist vor allem für kleinskalige Untersuchungen in der unteren PBL und für Wechselwirkungen zwischen der Erdoberfläche und Atmosphäre der Fall. Die wichtigsten Vorteile von Multikoptern waren die flexiblen Messungen mit hoher räumlicher und zeitlicher Auflösung als auch die Wiederholbarkeit bei stationärer Atmosphäre ohne das Ökosystem zu beeinflussen.

1 Introduction

Over the last years, unmanned aerial vehicles (UAVs) or colloquially known as drones became popular not only for leisure time activities but also for scientific research. Remotely controlled platforms equipped with all available kinds of sensors and cameras captured the air space, observing the Earth from above. On the one hand, this involves risks when leading to a crowded air space, but on the other hand, their usage enables new possibilities to investigate the Earth and the adjacent atmosphere above – the planetary boundary layer (PBL).

The PBL is this part of the atmosphere which is directly influenced by the Earth's surface. Its upper border varies within tens of meters to several kilometers depending on weather conditions and time of the day (Wallace and Hobbs, 2006; Schönwiese, 2008). Investigation of interactions between the atmosphere and the land surface is important to understand transport processes in the atmosphere and the exchange with the land surface on local to regional scales. UAVs are predestined for such observations due to their ability to measure atmospheric variables across different scales – from the surface through the PBL and even up to the free atmosphere.

With regard to global warming, impacts on a local to regional scale will become more important to initiate adaptation or mitigation strategies to protect society, economy and environment (Reid et al., 2009).
In order to investigate climatic changes, long-term observations are necessary to gain knowledge about climate variables such as air temperature, water vapor content, wind, and radiation as well as atmospheric composition and chemistry (Keeling, 1998; Nisbet, 2007; Zacharias et al., 2011). Simultaneously, intensive observations are needed to understand processes across scales and at the transition from the atmosphere to the Earth's surface.
Having this information, model simulations on different scales and their interrelations can help to get insights on future changes. Especially the overlap of scales, when parameterizations are necessary, is challenging in model simulations. But by using UAVs, these overlapping scales can be investigated while measurements of several atmospheric state variables are possible at the same time.

1.1 State of the Art

1.1.1 The Planetary Boundary Layer

The planetary boundary layer is the lowest part of the atmosphere. Its height is mainly dependent on solar radiation and thus on time of day. On average the PBL has an extent of about one kilometer in the mid-latitudes. While during daytime, the height can reach up to two or three kilometers, during nighttime several tens or hundreds of meters are predominating. Together with the free atmosphere, which is separated from the PBL through a capping temperature inversion, they form the troposphere (Wallace and Hobbs, 2006; Schönwiese, 2008).
Exchange between the PBL and free atmosphere is hindered through the inversion, thus moisture and pollutants are trapped in the PBL. Mixing within the PBL is predominantly turbulent. Dependent on weather conditions, three different conditions of the PBL are distinguishable – stable, neutral and unstable. Stable atmospheric conditions mostly occur during nighttime when the surface is colder than the air above or in case of warm air advection. Then, the PBL height is tens to hundreds of meters. In contrast, sunny days with weak winds lead to unstable conditions with convection and a larger vertical extent of the PBL. The same is true for cold air advection. During windy and overcast weather conditions, neutral stratification is predominating (Stull, 1988; Roedel and Wagner, 2011).
During the latter two atmospheric states, turbulence together with advection is responsible for mixing processes of pollutants and trace gases within the PBL. It is caused by a destabilization of the atmosphere due to external forcing. Thermally driven turbulence is called free convection which is caused by heating of the surface. From warmer surfaces, plumes of warm air rise up and cold air sinks over colder surfaces. Mechanically turbulence is a result of shear in the mean wind due to obstacles, e.g. mountains or trees, leading to a forced convection (Wallace and Hobbs, 2006).
Consequently, the PBL shows spatial and temporal variations mainly depending on surface characteristics, incoming energy from the sun and weather patterns.

For the vertical and horizontal investigation of the PBL, well-known techniques can be applied, which are either ground-based as towers, balloons, radiosondes and remote sensing instruments or airborne with aircraft and satellites (Konrad et al., 1970). Depending on the scale of interest and purpose of the measurements, these methods provide different advantages and disadvantages.

The operation of towers is fixed to a certain location and the vertical information is in most cases limited to the height of the tower as well as to discrete levels at the tower. However, towers provide continuous recording of the investigated variables and they are routinely used. Boundary layer mixing processes are investigated (Bakwin et al., 1998; Werth et al., 2017; Mateling et al., 2018) as well as greenhouse gas concentrations (Sasakawa et al., 2010; Pillai et al., 2011; Andrews et al., 2014) and particulate matter (Mikhailov et al., 2017). Tower-based measurements take place focusing different land use types (Berger et al., 2001; Davis et al., 2003; Miles et al., 2012) or remote areas like the Antarctic (Mateling et al., 2018).

With radiosondes, balloons or kites, information of meteorological conditions can be acquired for an extended vertical range throughout the whole PBL and partly even higher. But these systems are expensive and the location of the vertical profiles is dependent on atmospheric conditions. Nevertheless, mobile and temporary applications are possible, as the determination of the PBL height (e.g., Hennemuth and Lammert, 2006; Seidel et al., 2010; Korhonen et al., 2014). Especially radiosonde data is often used and easily accessible, for example through the "Integrated Global Radiosonde Archive" (IGRA) (Durre et al., 2006), which includes more than 1500 stations.

Research aircraft can cover large areas in the range of hundreds of kilometers within a short time span, but their operation close to the ground is still challenging (Velasco et al., 2008; Martin et al., 2011) and requires special permissions. Their high payload capacity allows to carry many sensors for different applications (Junkermann, 2001; Freney et al., 2014). Satellites operate from even higher altitudes for investigations spanning the whole Earth's surface. A high spatial resolution (tens of meters instead of kilometers) is achievable at the expense of a lower temporal resolution (weeks instead of days) and the other way round. Information from different vertical levels is not possible, but instead for the whole column. Satellite data is used, for example, for the aerosol optical depth (Beekmann et al., 2015; Tian et al., 2017) or for Earth surface characteristics as land surface temperature (LST) (Li et al., 2013).

Applying ground-based remote sensing methods as acoustic or optical instruments, information about the vertical atmospheric state is available throughout the whole PBL. Vertical profiles of meteorological variables as air temperature (Hammann et al., 2015) and wind (Banta et al., 2013; Brugger et al., 2018) are measured or the PBL height is determined (Wiegner et al., 2006; Emeis et al., 2009; Korhonen et al., 2014; Kotthaus et al., 2018). But the number of observable variables at the same time is limited (Muller et al., 2013). While

getting data from low altitudes up to about 50 m above ground level (a.g.l.) is hardly feasible using acoustic sensors, optical remote sensing methods are suitable applying certain scan patterns with low elevation angles at the position of such an instrument (e.g., Calhoun et al., 2006; Wolf et al., 2017). Especially for meteorological investigations in urban areas, remote sensing techniques gained more importance (Tan et al., 2015; Baklanov et al., 2018). Since scale interrelations are increasingly investigated, the application of several methods spanning different scales is beneficial and more often used than before (Barlow et al., 2017).
In recent times, unmanned aerial vehicles are applied for investigations in the PBL as well. Their advantage is that atmospheric measurements of several variables are possible at the same time. In addition, three-dimensional flights are easily feasible with a flight time between minutes to hours depending on payload and size.

1.1.2 UAVs in Environmental Sciences

The usage of unmanned aerial vehicles dates back to the 1970s, when the first small remote controlled model airplanes were taken for atmospheric measurements. But their payload capacity was not high and appropriate sensors were not available yet. Konrad et al. (1970) belonged to the first who measured convective processes with an UAV and reached a height of 3000 m a.g.l. The limiting factor was the line-of-sight and therefore binoculars were used. Later, UAVs were operated to fly below thunderclouds (Bluestein et al., 1990) and for weather forecast, e.g. for information about cold fronts and tropical cyclones (Holland et al., 1992; McGeer and Holland, 1993). A lot of those early measurements took place over water, because this reduced the risk of damage to property and people. Another limitation for the payload was the combustion engine and the necessary fuel. Therefore, there was the tendency to operate bigger UAVs with higher payloads. But this led to higher costs for the UAV and its operation (Stephens et al., 2000).

Over the last 20–30 years, miniaturization of electronics and sensors was pushed and the availability of GPS as well as the usage of electric motors with batteries led to a wider range of UAV-based applications for scientific purposes (McGeer and Holland, 1993). Especially the measurement of meteorological variables was a major application. The so-called “Aerosonde” was often used, for example for comparison of air temperature, humidity, and wind between UAV and radiosondes (Soddell et al., 2004) or for observations of the sea ice

development in the Arctic Ocean (Inoue et al., 2008). Corrigan et al. (2008) investigated the distribution of aerosols over the Indian Ocean and Astuti et al. (2008) equipped an UAV with remote sensing technologies to sense the plume of a volcano.

In recent years, unmanned aerial vehicles became increasingly used as flying platforms for measurements in atmospheric research for both vertical and horizontal monitoring (Villa et al., 2016). Martin et al. (2011) demonstrated the utilization of fixed-wing UAVs for measurements of meteorological variables, i.e. air temperature, humidity and wind, up to 1600 m a.g.l. In addition, de Boer et al. (2016) implemented radiation and aerosol size distributions sensors, Altstädter et al. (2015) focused on ultrafine particles and Båserud et al. (2016) showed the possibility of turbulence measurements. Nathan et al. (2015) measured methane with an in situ sensor flying around a compressor station to calculate its emissions. The importance of knowing both meteorological conditions and methane (or aerosols, particulate matter, etc.) was highlighted in previous studies (Mathieu et al., 2005; Bamberger et al., 2014).

Having interest in a smaller scale of several hundreds of meters, multicopters are the flying platform of choice. They offer flexible maneuverability at low flight speed and the possibility of hovering (i.e. no horizontal movement). Their applications include meteorological and air quality measurements, e.g. particulate matter (Alvarado et al., 2015) and aerosols (Brady et al., 2016). Air samples can be taken with a multicopter for analyses of chemical composition (Chang et al., 2016) and greenhouse gas concentrations (Andersen et al., 2018). Brownlow et al. (2016) and Greatwood et al. (2017) demonstrated that this is feasible up to 2500 m, even at high wind speeds (trade winds). Neumann and Bartholmai (2015) and Palomaki et al. (2017) showed that the onboard flight control sensors can be used to derive wind estimates from a multicopter's attitude control data.
Although small and lightweight methane sensors are available (Berman et al., 2012; Khan et al., 2012), current multicopters with a takeoff weight below 5 kg still require further miniaturization of the sensors. For carbon dioxide, for example, a lightweight onboard sensor was successfully operated with a multicopter (Kunz et al., 2018).
There is a variety of research questions for the application of UAVs. But until now, mobile investigations of vertically resolved profiles or spatially resolved patterns of various atmospheric variables are not routinely used yet. In the following chapters 1.1.3 and 1.1.4, two applications of UAVs for atmospheric investigations are further addressed.

1.1.3 Estimation of Evapotranspiration

The evapotranspiration (ET) rate is a crucial component in hydrology and climate, i.e. for the local and regional water cycle and thus for water management such as irrigation in agriculture. ET means the combination of the evaporation from the surface and transpiration of the vegetation. Both meteorological conditions and land surface temperature have impacts on evapotranspiration at the interface of the Earth's surface and the atmosphere. Incoming energy of the sun is the main driver of warming the land surface leading to transport of heat and water at the soil-atmosphere boundary or via stomatal conductance between the biosphere and the atmosphere (McPherson, 2007; Kalma et al., 2008). The magnitude of this transport is dependent on land surface temperature, which is mainly affected by albedo (the portion of reflected short-wave radiation to total short-wave radiation), vegetation cover and soil moisture. LST refers to the temperature which is calculated from infrared radiation measured at the interface between the land surface and the atmosphere and is thus the radiometric temperature (Norman and Becker, 1995; Gillespie, 2014). For example, for a grassland site the radiometric temperature is a combination of the vegetation and soil temperature.

Conventionally applied ET techniques are mainly based on field-site measurements. Among others, the Bowen ratio method and the eddy covariance (EC) method are often used (Li et al., 2009; Foken, 2016). With the former, the ratio between the latent and sensible heat flux is calculated by measuring air temperature and humidity at two heights as well as net radiation and ground heat flux. The closer this ratio equals zero, the higher the portion of the latent heat flux (Liu and Foken, 2001). The latter method provides a direct calculation of the latent heat flux and thus evapotranspiration from fluctuations of humidity and the vertical wind vector (Baldocchi et al., 1988; Baldocchi, 2003). It is widely used for exchange between an ecosystem and the atmosphere of, for example, carbon dioxide and water (Aubinet et al., 2012). The EC method is typically applied within the surface boundary layer, which is up to about 50 m above ground depending on atmospheric stability (Stull, 1988). Within this layer the fluxes are representative for the underlying surface and constant with height (Aubinet et al., 2012). Besides, pan measurements and weighing lysimeters can be used as well for ET estimations by recording the water loss (Li et al., 2009; Foken, 2016).
However, there are limitations in applying those methods for measuring evapotranspiration because they are only valid for homogeneous surfaces and they are not applicable for larger scales as regional or global.

To overcome these constraints remote sensing techniques as imagery from satellites or aircraft were used since the late 1970s (Price, 1980; McCabe and Wood, 2006; Morillas et al., 2013). Advantages using those methods are large and continuous spatial coverage within a short time and especially useful for areas where it is difficult to install ground-based instrumentation (Jackson, 1985; Rango, 1994). For example, installation of instruments in peatlands would change the environmental conditions, which is not the case using space-born remote sensing techniques.
In recent years, unmanned aerial vehicles were increasingly used for visible and thermal imagery (Rango et al., 2009; Watts et al., 2012; Turner et al., 2014) but applications for *ET* estimations are rare (Hoffmann et al., 2016; Ortega-Farías et al., 2016; Brenner et al., 2017, 2018). Data acquired with those platforms have the advantage of high spatial and temporal resolution and a more flexible application. For example, flights during cloudy conditions are no problem compared to satellites because the flying height is close to the ground (normally less than 100 m a.g.l.) and therefore beneath the cloud base (Guzinski et al., 2013).

Using *LST* data is one possibility to derive evapotranspiration by the application of different models distinguishing between (semi-)empirical and analytical methods. While the former mainly uses remote sensing data with minimal ground-based information, the latter includes physical processes with varying complexity using both remote sensing and ground-based data (Li et al., 2009).
One of the easier applicable methods is the simplified empirical regression method (Jackson et al., 1977), which directly relates the daily ET to the difference of land surface and air temperature measured around noon. Site-specific regression coefficients are dependent on surface roughness, wind, stability and other parameters. Applications are limited to the field site.
A more complex method is the so-called Surface Energy Balance Algorithm for Land (SEBAL) (Bastiaanssen et al., 1998), which needs only a minimum of ground-based measurements. The hydrometeorological variables are estimated empirically and the fluxes are independent on land cover. This method is applicable for different geographical regions up to the continental scale.
In addition, there is the residual method based on the surface energy balance (Li et al., 2009). One-source and two-source models are distinguishable, while the former treats the surface as homogeneous and the latter as the combination of vegetation and soil. Consequently, the latter is more complex to use but more accurate for sparse vegetated surfaces (Kustas and Daughtry, 1990; Anderson et al., 1997). The principle of the residual method is to calculate net

radiation, ground heat flux and sensible heat flux from existing remote sensing and ground-based data and as a residual the latent heat flux is derived. Therefore, spatial and temporal information about meteorological conditions and radiation as well as surface parameters like vegetation cover and surface roughness are necessary.

1.1.4 Nocturnal Methane Emissions

Greenhouse gases gained more importance over the last decades, especially in the context of climate change. Methane is, after water vapor and carbon dioxide, the most important greenhouse gas in the atmosphere and its global budget is relatively well known (Dlugokencky et al., 2011). Global atmospheric concentration increased exponentially since preindustrial times (Kirschke et al., 2013) with a global annual mean concentration of 1.834 ppm in 2015 (Saunois et al., 2016). Continuous measurements of methane concentrations are available since the early 1980s (Fig. 1.1). Although this increase was not continuous, a clear positive trend is detectable.

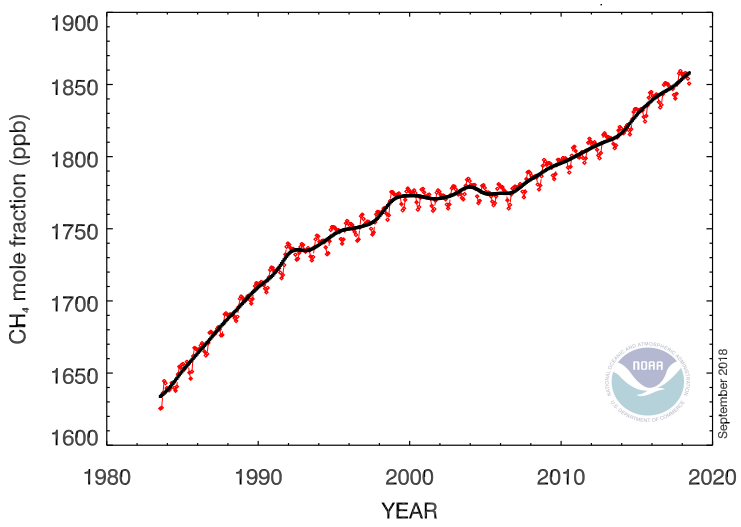

Fig. 1.1: Global monthly mean of methane concentration (y-axis) from 1984 to 2018 (x-axis). Red squares represent the monthly values and the black line shows the 12-month running mean (NOAA/ESRL, 2018).

About two thirds of global methane emissions can be traced back to anthropogenic sources (Nisbet et al., 2014). While tropical wetlands are the greatest natural methane source, fossil- and agricultural-related emissions have the highest impact from anthropogenic sources (Bergamaschi et al., 2013; Ciais et al., 2013; Hausmann et al., 2016; Dean et al., 2018).
Although the global methane budget is well known, budget controlling processes on local and regional scales are still not well investigated (Dlugokencky

et al., 2011). But this is important because different scales interrelate when investigating biosphere-atmosphere exchange processes of trace gases. Methane is emitted on a plot scale considering soil or farms as sources. However, its mixing in ambient air takes place on a local and transport on a local to regional scale, e.g. due to thermally or mechanically driven dynamics.

Bottom-up and top-down approaches are widely used to determine CH_4 emission budgets (Nisbet and Weiss, 2010), but with differences between the two approaches up to 20 % for the 2000s (Kirschke et al., 2013). During daytime, the atmosphere is on average well mixed and with bottom-up approaches fluxes can be determined by applying for example the frequently used eddy covariance method (Baldocchi et al., 1988; Baldocchi, 2003). This is a turbulent transport technique for the exchange of trace gases (among others) between land surface and atmosphere. The addressed scale ranges between hundreds of meters to several kilometers (Schmid, 1994).
But in nighttime, stable atmospheric conditions can be often found which impede vertical mixing. Especially in calm and clear nights, the nocturnal boundary layer (NBL) develops from the surface and its height varies between couples of tens to a few hundreds of meters (Stull, 1988). The height of the NBL influences the near-surface concentration of atmospheric compounds (Schäfer et al., 2006). Choularton et al. (1995), Beswick et al. (1998) and Stieger et al. (2015) have been shown that vertical gradients of methane develop with accumulation close to the ground when sources at or close to the ground are present. Bamberger et al. (2014) used a car equipped with a methane sensor for investigations in a valley finding higher concentrations near the bottom of the valley than on both hillsides. Therefore, it is not sufficient to only have point measurements, but investigations of vertical profiles are necessary to take these gradients into account for the methane budget. Applying the NBL method (Denmead et al., 1996, 2000; Emeis, 2008), local methane fluxes are calculable for nighttime conditions by concentration changes within the NBL over time. Both Pattey et al. (2002) and Mathieu et al. (2005) pointed out that this is the preferable method under stable atmospheric conditions, but difficult under non-ideal conditions (Wittebol, 2009).

For interpretation of concentrations and fluxes, footprint estimates are derived from models, which estimate the area of the surface, from where sources/ sinks contribute to the concentration or flux. This is especially important for up-scaling processes. Pasquill (1972) was the first who described such a model. In the 1990s, this topic became more important with the development of different models (Schmid, 2002). The most important models which were

developed over the years were summarized by Vesala et al. (2008). Problematic with those footprint models is that they are not optimized for stable conditions as found during nighttime. Eddy covariance measurements and surface calculations have the assumption of surface homogeneity (Mauder et al., 2013). Since the footprint for nocturnal fluxes is in the order of kilometers, the surface cannot always be assumed to be homogeneous. Nevertheless, applying such footprint models gives an idea about the size and shape of the footprint. But it is important to investigate vertical and horizontal variations of methane emissions to improve those models.

1.2 Motivation

Atmospheric processes and transport, especially in the lower PBL, are influenced by the Earth's surface and vice versa. Understanding of such interactions is of fundamental importance to estimate effects of, for example, climate change. These interactions have an impact on atmospheric transport and thus on local and regional distribution of gases and air pollutants.
From the literature review above follows that UAVs provide a suitable tool for investigations in the lower atmosphere as well as at the transition of the atmosphere and the land surface. For several years, UAVs have been operated for such purposes. But there is still the challenge of measuring all necessary variables spatially resolved (three-dimensional) and at the same time based on the flying platform. The overlap of scales is another important aspect to address, which is not always easily feasible.

Considering the water cycle and the surface energy balance, the evapotranspiration plays an important role and is quite variable comparing different land use types (e.g., Liu et al., 2010). In agriculture, irrigation strongly depends on ET, which is influencing soil moisture. The water cycle of a peat bog is dependent on ET and precipitation. Forested areas show high ET rates and do not only influence the micro-scale but also the meso-scale depending on its size. Since evapotranspiration is quite heterogeneous across different spatial scales and its magnitude is dependent on meteorological conditions as well as surface and soil characteristics, its determination needs a lot of different variables and process understanding. In order to gain information about ET across scales and land use types, flexible and easy-to-apply methods are necessary.

There are not only exchange processes of water vapor and heat between the atmosphere and land surface, but also other air constituents as greenhouse ga-

ses or pollutants. With regard to methane, the global budget with sources and sinks is relatively well investigated (Dlugokencky et al., 2011), but there are more investigations necessary on a local and regional scale. Especially, nighttime conditions were rarely studied, but this is the time a stable layer – the nocturnal boundary layer – can develop leading to a vertical methane gradient in case of sources close to the ground (Choularton et al., 1995; Beswick et al., 1998; Stieger et al., 2015). Simultaneous measurements of meteorology and methane are necessary throughout the whole NBL for emission estimations and thus the methane budget. Since the NBL height is variables even within the night, adaptation of methods to this purpose is needed.

In order to address these research questions spanning different spatial scales and topics, UAVs attracted attention over the last decades. Their advantage is that atmospheric measurements of several variables are possible at the same time. Three-dimensional flights are easily feasible with a flight time between minutes to hours depending on payload and size. In addition, the application of UAVs is beneficial for measurements in sensible ecosystems or difficult to reach areas. Applying a multicopter for ET estimations, there is no need for a ground-based installation and the operation provides flexible measurements in space and time without influencing the ecosystems. The same is true for the estimation of methane emissions with the advantage that multicopters can carry both methane and meteorological sensors at the same time.
Consequently, further development and usage of UAVs is justified and has a high potential to investigate local and regional processes with regard to exchange between the Earth's surface and atmosphere.

1.3 Objectives

This thesis is aiming the development and application of a UAV-type platform for measurements of spatially distributed variables important for land surface-atmosphere interactions, which includes energy balance components and methane fluxes.
Therefore, the objectives of this thesis are:

- Demonstrating the technical feasibility of a hexacopter as a meteorological instrument for three-dimensional atmospheric investigations in order to address the following two objectives about exchange processes between the atmosphere and the land surface.

- Investigating the applicability of hexacopter-based measurements for the

spatial and temporal estimation of evapotranspiration above an agricultural area and the identification of driving variables. In this context, interactions between soil, vegetation and atmosphere have to be considered.

- Determining the benefits of using instrumented hexacopters as platforms for methane emission rates during nighttime instead of ground-based instrumentation. To this end, influences of local and regional meteorological conditions and transport processes on the methane concentration are considered within the whole NBL.

1.4 Innovation and Publications

This thesis is a feasibility study of hexacopter-based hydrometeorological and methane measurements and the application for small-scale atmospheric transport processes close to the land surface consisting of the following innovations:

- Development of a compact "meteorological instrument" based on a hexacopter for three-dimensional investigations in the lower PBL,
- Flexible and low-cost solution of extension of existing tower-based infrastructure and filling gap to remote sensing techniques and aircraft measurements,
- Estimation of energy balance components with the residual method based on mainly hexacopter-derived data,
- Vertical in situ methane measurements in combination with meteorological conditions on hexacopter platforms to estimate agricultural methane emissions.

Parts of this thesis were already published in peer-reviewed journals. Brosy et al. (2017) demonstrated the feasibility of multicopter-based measurements of meteorological variables and methane concentration at the same time, in which tower-based measurements were extended by a factor of five by raising a tube up in the air with a hexacopter. Chapter 3 and 5 in this thesis are based predominantly on this publication. A continuation of those tube-based methane investigations was the development and integration of a methane sensor onboard a hexacopter and the demonstration of its applicability (Golston et al., 2017). Further analysis and interpretation of measured methane concentrations can be found in chapter 7 of this thesis. In Wolf et al. (2017) first

meteorological results were shown (chapter 5) and how those measurements were placed in the context of the ScaleX campaign in 2015.

The above mentioned publications are the following ones:

- **Brosy, C.**, Krampf, K., Zeeman, M., Wolf, B., Junkermann, W., Schäfer, K., Emeis, S., and Kunstmann, H.: Simultaneous multicopter-based air sampling and sensing of meteorological variables, Atmos. Meas. Tech., 10, 2773-2784, doi:10.5194/amt-10-2773-2017, 2017.
- Golston, L. M., Tao, L., **Brosy, C.**, Schäfer, K., Wolf, B., McSpiritt, J., Buchholz, B., Caulton, D. R., Pan., D., Zondlo, M. A., Yoel, D., Kunstmann, H., and McGregor, M.: Lightweight mid-infrared methane sensor for unmanned aerial systems, Appl. Phys. B., 123, 170, doi:10.1007/s00340-017-6735-6, 2017.
- Wolf, B., Chwala, C., Fersch, B., Garvelmann, J., Junkermann, W., Zeeman, M., Angerer, A., Adler, B., Beck, C., **Brosy, C.**, Brugger, P., Emeis, S., Dannenmann, M., De Roo, F., Diaz-Pines, E., Haas, E., Hagen, M., Hajnsek, I., Jacobeit, J., Jagdhuber, T., Kalthoff, N., Kiese, R., Kunstmann, H., Kosak, O., Krieg, R., Malchow, C., Mauder, M., Merz, R., Notarnicola, C., Philipp, A., Reif, W., Reineke, S., Rödiger, T., Ruehr, N., Schäfer, K., Schrön, M., Senatore, A., Shupe, H., Völksch., I., Wanninger, C., Zacharias, S. and Schmid, H. P.: The ScaleX campaign: scale-crossing land-surface and boundary layer processes in the TERENO-preAlpine observatory, Bull. Amer. Meteor. Soc., 98(6), 1217-1234, doi:10.1175/BAMS-D-15-00277.1, 2017.

1.5 Project Integration

This thesis is part of the cluster on unmanned aerial system (UAS)-based remote sensing in climate and environmental research with the topic "Transdisziplinäre Ansätze zur klima- und umweltrelevanten Fernerkundung basierend auf Kleinplattformen" initiated by the Graduate School for Climate and Environment (GRACE) of the KIT (http://www.grace.kit.edu/english/166.php). This includes the funding of doctoral theses as well as meetings for idea exchange and sharing of instrumentation.
Current research topics include processes in vegetation, erosion and sediment distribution as well as atmospheric processes together with greenhouse gas emissions, which is the topic of this thesis. The common aspect is the usage of UASs to investigate those mentioned topics.

1.6 Structure of the Thesis

In the following chapter 2, the investigation site DE-Fen of the TERENO pre-Alpine observatory with instrumentation is explained as well as the two ScaleX campaigns in the summers 2015 and 2016. Afterwards, chapter 3 deals with the hexacopter systems including setup, instrumentation and data processing, while in chapter 4 statistical methods as well as calculations and models are presented.
Chapters 5 to 7 contain the core of this thesis. The first of those shows the feasibility of the hexacopter-based measurements of investigated variables, while chapter 6 and 7 deal with scientific analyses about ET estimates and methane emissions. The last chapter gives an overall conclusion as well as an outlook.

2 Investigation Area DE-Fen

2.1 Geographic Location and Climate

The investigation site of this study was Peißenberg-Fendt (DE-Fen), which is located in the foothills of the Bavarian Alps, Germany, at 600 m above sea level (47.832° N, 11.062° E) (Fig. 2.1). It is a comprehensively instrumented research site within the TERENO pre-Alpine Observatory (Zacharias et al., 2011). DE-Fen is situated in a north–south aligned valley towards the Alps with prevailing agricultural land use, i.e. grassland and crops. To the west, the forested terrain rises up 100–130 m above the valley bottom, which extends eastwards.

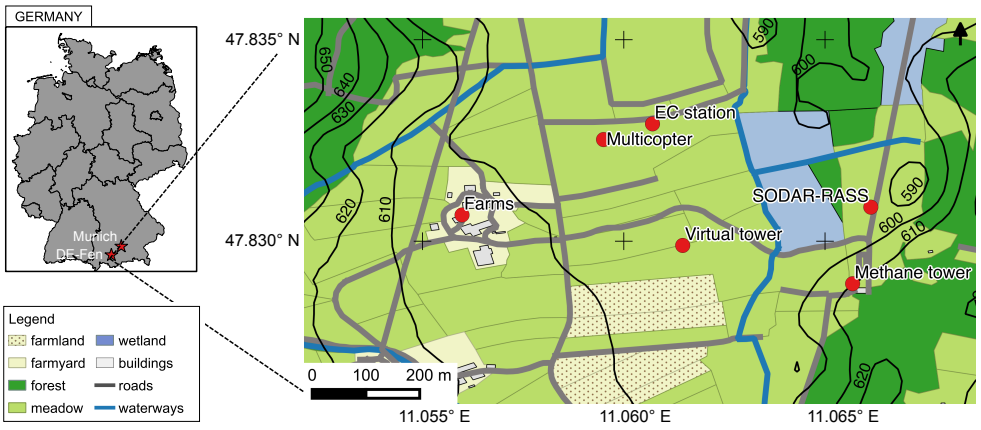

Fig. 2.1: Measurement site DE-Fen, Germany, with land use and ground-based instrumentation important for this study during the ScaleX campaign 2015. Contour lines stand for altitude (m) above sea level (QGIS, OpenStreetMap).

According to the climate classification of Köppen and Geiger (Kottek et al., 2006), the investigation area belongs to the classification category C_f, which means "warm temperate climate, fully humid". Looking at the long-term measurements at Wielenbach (47.8827° N, 11.1576° E; 550 m a.g.l.) operated by the German Weather Service (DWD), which is about 10 km to the northeast, these conditions can be confirmed (Fig. 2.2). While January is the coldest month with mean air temperature of -0.5 °C, July is the warmest month with

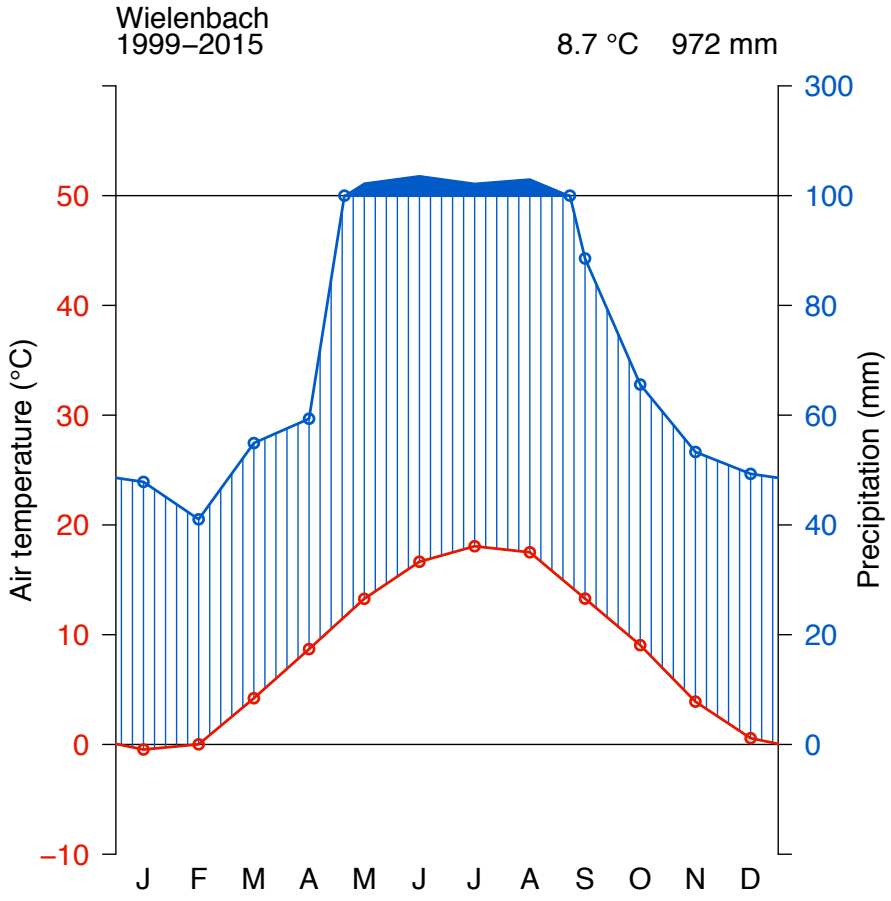

Fig. 2.2: Climate diagram after Walter and Lieth for Wielenbach, Germany, operated by the German Weather Service. On the left y-axis, air temperature is shown in red and on the right y-axis precipitation in blue (Data by DWD 2017).

18.1 °C. Summer has the highest amount of precipitation with over 100 mm from May to September, while February is the driest month.
Further details on climate characteristics of the region can be also found in Kunstmann et al. (2004, 2006).

Since DE-Fen is only about 30 km north of the northern Alpine mountains, it is influenced by the meso-scale mountain and valley breezes (Lugauer and Winkler, 2005; Graf et al., 2016) occurring one after the other on a daily cycle; the so-called Alpine pumping. During daytime, the mountain slopes are heated faster than the valley, warm air rises and at the ground the air flows towards the mountains. At night, the mountains cool down faster and thus the air above the ground, which leads to a cold air outflow towards the valley. This means for DE-Fen prevailing northerly wind directions during daytime and southerly directions during night in case the requirements are fulfilled, namely high sun radiation and clear nights. Additionally due to the terrain, orographical winds and diurnal wind systems favor northerly and southerly directions with

occasional easterly or northeasterly components. Westerly winds are normally associated with orographic turbulence because of the forested hill slope in the west of the investigation area (see Fig. 2.1).

2.2 The Research Program TERENO

The TERestrial ENvironmental Observatories (TERENO) are an interdisciplinary and long-term research program covering whole Germany to investigate impacts of global change to the regional scale (http://teodoor.icg.kfa-juelich.de/overview-de). With regard to global change, not only climatic changes are included, but also changes to land use, environment, economy and society. In this century, those are major challenges humans have to face. Finding solutions to these challenges is the main focus to increase the understanding and knowledge to react to global changes (Zacharias et al., 2011).

For process understanding those long-term observations are not sufficient because their spatial resolution is to coarse. TERENO, for example, consists of four observatories spread over Germany, but a complete coverage is not possible. Therefore, intensive measurement campaigns are additionally necessary to increase the understanding of processes across different scales. Then, spatial distributions as well as gradients can be investigated by extending an existing infrastructure for a limited amount of time. In addition, new methods or instruments can be tested and their applicability demonstrated (Wolf et al., 2017). Such an example are the ScaleX campaigns organized by the Institute of Meteorology and Climate Research (IMK-IFU) of the Karlsruhe Institute of Technology (KIT). The campaigns focused on processes in the planetary boundary layer and between the atmosphere and the land surface with both measurements and modeling.

2.3 ScaleX Campaigns and Instrumentation

ScaleX In order to extent the long-term investigations by using scale-crossing investigations of atmospheric properties at the site, the intensive measurement campaigns ScaleX took place in June to July 2015 (Wolf et al., 2017) and June to July 2016. These intensive campaigns aimed to address atmosphere-land surface interactions across different scales with both measurements and modeling. The investigations ranged from ground-based point measurements to three-dimensional investigations with remote sensing techniques and airborne platforms. Simulations with different micro- to meso-scale models were inclu-

ded, too. Investigations of spatial patterns and vertical gradients to obtain three-dimensional and more detailed information were focused. The different research questions were summarized in "work packages" addressing various topics such as nocturnal greenhouse gas budgets, precipitation and soil moisture interactions or vertical profiles of meteorological variables. These packages were not the same for the two campaigns but similar. More information is provided under http://scalex.imk-ifu.kit.edu.

Instrumentation An overview about the location of instruments is given in Fig. 2.1. The site is equipped, among other instruments, with a permanent eddy covariance station for carbon dioxide, water vapor and energy flux measurements (Mauder et al., 2013; Zeeman et al., 2017). In addition, this station provided measurements of air temperature, relative humidity, wind conditions, pressure at 2 m a.g.l. and radiation information. In the area around the station, soil moisture and temperature were also available.

Besides, a ceilometer (CL51, Vaisala, Helsinki, Finland) for determination of the mixing layer height belongs to the permanent instrumentation at the DE-Fen site (Münkel, 2007; Schäfer et al., 2016). A ceilometer is a small lidar, which emits light beams and records the vertical profile of the optical backscatter from aerosols. Originally, ceilometers were used to detect the lower level of clouds. Its vertical resolution is 15 m with a range up to 3–4 km. Hourly means were used for analysis.

During the campaigns, a radio acoustic sounding system (Sodar-RASS, Metek GmbH, Elmshorn, Germany) was installed on the east side of the area. The Sodar-RASS consists of a sodar for the wind measurement with an acoustic signal and two radar antennas for measurements of vertical profiles of air temperature (Emeis et al., 2009). The temporal resolution is 10 min with a range between 40 m to 650 m a.g.l. and a vertical resolution of 20 m.

In addition, vertical profiles of the three-dimensional wind speed and direction were determined at the intercept of three simultaneously scanning Doppler wind-lidar systems (model Stream Line, Halo Photonics Ltd, Worcester, UK) as a so-called "virtual tower". Horizontal information is available in 60 s and 18 m intervals from 3 m up to approximately 800 m a.g.l., the lowest vertical wind speed information at about 40 m a.g.l.

Methane mixing ratios were determined using a cavity ring down (CRD) spectrometer (G2508, Picarro Inc., Santa Clara, CA, USA) with an accuracy of < 0.007 ppm. In 2015, the instrument was installed close to a 10 m tower equipped with wind speed and direction measurements (CSAT3, Campbell Scientific Ltd., Bremen, Germany; WindMaster 3D, Gill Instruments, Lyming-

ton, Hampshire, UK) and sample air inlets at 1, 5 and 10 m height. This tower was located in the south-east of the research site. The three sampling lines (stainless steel, 3.2 mm outer diameter, 1.2 mm inner diameter) were flushed continuously with ambient air and a custom built system of solenoid valves connected one sampling line to the CRD spectrometer every 75 s. In 2016, a 9 m tower was installed about 100 m to the east of the EC station with sample air inlets at 1, 6 and 9 m as well as sonic anemometers (uSonic3, Metek GmbH, Elmshorn, Germany, WindMaster 3D, Gill Instruments, Lymington, Hampshire, UK) for EC measurements at 6 and 9 m.
The so-called "SoilNet" represents a wireless hydrometeorological sensor network with soil water content and soil temperature (SMT-100, TRUEBNER Instruments, Neustadt, Germany) measurements at 5, 20 and 50 cm depth every 15 min. This network covers the grassland site south of the EC station and therefore was installed in its footprint area covering 400 m x 330 m. Altogether, there were pairs of sensors buried at 55 locations (Wolf et al., 2017).

Additionally, the continuous measurements were complemented by airborne-based measurements during so-called intensive observation periods (IOPs). While in 2015, this was three times for two days, in 2016, there was one longer IOP lasting a week. During this time, a microlight aircraft (only 2015, Junkermann, 2001; Metzger et al., 2012, 2013) and several unmanned aerial vehicles, both multicopter and fixed-wing UAVs, were measuring mostly meteorological variables, but also LST, CO_2 and CH_4. While the multicopters covered an area of a couple of hundreds of meters around the EC station, the fixed-wings had permission to fly up to 1000 m a.g.l. and covered an area of 1000 m x 1000 m. The microlight aircraft flew 10 km x 10 km around the investigation area and up to the free troposphere. Measurements during nighttime were only possible with the UAVs, because they had permission to fly with lights. The microlight only had permission from half an hour before sunrise until half an hour after sunset.

3 Unmanned Aerial Systems

3.1 Overview

An unmanned aerial vehicle defines a flying platform without a pilot on board. A distinction is made between fixed-wing UAVs which are similar to an airplane and multicopters/multirotors. Multicopters usually have four (quadrocopter), six (hexacopter) or eight (octocopter) rotors, which are horizontally aligned to each other. This allows a sensor positioning in the center of the copter near the center of gravity for a better balance and flight stability.
Depending on the objective, both UAV types provide different advantages. Fixed-wing systems can cover a vertical and horizontal range of several kilometers and therefore, they are suitable for investigations throughout the boundary layer. Multicopters offer flexible maneuverability at low flight speed and the possibility of hovering (i.e. no horizontal and vertical movement).

In the following, only multicopters are addressed further because they were the applied platform in this thesis.

3.2 Multicopters

Multicopter is an umbrella term for copters with four, six or eight rotors. The name is derived from the number of rotors so quadrocopter, hexacopter and octocopter. Each of the rotors consists of a propeller, motor and controller, which are connected to the flight controller and to the battery. The speed of each rotor is controlled individually by the autopilot and the even number is necessary to compensate the torque and therefore half of the rotors turn clockwise and the other half anti-clockwise. Otherwise, the multicopter would permanently turn around its vertical axis (yaw axis). Movement is possible in all directions changing the spinning speed of the propellers, while fore- and backwards is called “pitch” and left and right “roll”. The “yaw” angle defines its horizontal orientation. “Hovering” is the term for neither horizontal nor vertical movement.
Two sensors are essential for flying: an accelerometer and a gyroscope. While

the first measures the interia forces on the multicopter and therefore its acceleration, the latter measures the rotation rate around all three axes. The flight controller analyzes these data and controls the motors accordingly. Flight stability increases the more rotors a multicopter has. In case of a broken motor or propeller it is possible to land hexa- and octocopters, but not a quadrocopter. This is due to the fact that three remaining rotors are not enough to stabilize the platform. For autonomous flying, GPS, compass and barometer are necessary, too. With the GPS, longitude, latitude and altitude are known, the barometer is important for a better relative height precision by using air pressure difference and with the compass the horizontal orientation towards magnetic north can be determined. Autonomous flying means the autopilot gets a "mission" with way points and is flying all on its own including start and landing.
The multicopters used in this thesis were the hexacopter F550 and the hexacopter Pro X-3 Lite, which are described in the following.

Hexacopter F550 The mainly used multicopter was a commercially available hexacopter DJI F550 Flame Wheel (DJI Innovations, Shenzhen, China) with dimensions of 55 cm x 55 cm x 30 cm and a frame weight of 1.3 kg including motors, propellers, autopilot and electronics (Fig. 3.1a). The takeoff weight of 2 kg led to a flying time of approximately 10 min with a ground speed of 5 m s^{-1}. Nine inch carbon fiber propellers were used (Graupner E-PROP 9x5, Graupner/ SJ GmbH, Kirchheim unter Teck, Germany). The battery was a 4 cell LiPo (lithium polymer) with 5000 mAh and 14.7 V.
At the beginning, this hexacopter was controlled using the autopilot Naza-M V2 (DJI Innovations, Shenzhen, China), which was part of the bought set. The problem was that it was not easy to get all the important flight data like pitch, roll and yaw angles but only GPS data. Therefore, this flight controller was replaced by the open access autopilot Pixhawk (3DR, Berkeley, USA).

Hexacopter Pro X-3 Lite In addition, a second hexacopter platform the Pro X-3 Lite (Stein Elektronik, Jülich, Germany) was used in order to get a higher payload capacity (Fig. 3.1b). The frame and motors of the hexacopter itself had a weight of 3.1 kg including a battery of 1 kg. With a take-off weight of 4.9 kg, a flight time for vertical flights of 5–6 min was possible. Thirteen inch propellers were installed and the used battery was a 4 cell LiPo with 10000 mAh.
This hexacopter is normally equipped with a Naza-M V2 flight controller, but since this did not provide all necessary information for further analysis, a Pixhawk controller was also installed on this hexacopter.

So, both hexacopters were equipped with a Pixhawk (3DR, Berkeley, USA) autopilot for stabilized and autonomous flights. The autopilot contains a 3D accelerometer, gyroscope, magnetometer and barometer for position control as well as an external GPS (LEA-6 u-blox 6, u-blox, Thalwil, Switzerland) for autonomous flying. All data were logged onboard, attitude angles as well as motor output with 10 Hz, the accelerometer and gyroscope data at 50 Hz and GPS at 5 Hz. Additionally, a remote receiver was installed onboard for manual flying with the remote control (MX-16 HoTT, Graupner/ SJ GmbH, Kirchheim unter Teck, Germany). In case of a communication loss of the remote control, GPS signal or low battery status a pre-programmed fail-safe mode took over the control and initiated the landing. The open-source software Mission Planner was used for ground control to transmit and display important flight data (e.g. height, horizontal and vertical speed, battery capacity, position) during the flights. In addition, flight plans can be programmed for autonomous missions and communication with the autopilot is possible. Documentation is available about first steps using a multicopter with this software as well as installing sensors, changing flight parameters and more (http://ardupilot.org/copter/index.html). A schematic connection diagram and a table with electronic parts of the hexacopters are attached in the appendix (Fig. A1, Tab. A1).
For night flights, bright LEDs were mounted on the landing gear of the hexacopters for visibility and the identification of their orientation.

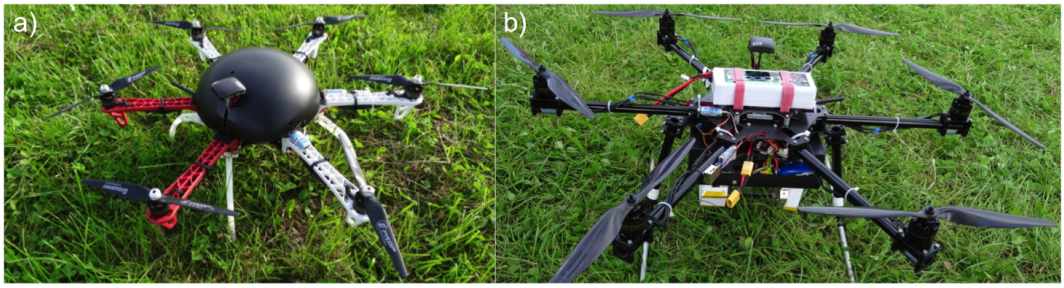

Fig. 3.1: a) Hexacopter F550 with meteorological as well as IR-sensor and b) hexacopter Pro X-3 Lite with onboard methane sensor below the bottom center plate.

3.3 Instrumentation

3.3.1 Onboard Sensors

Hexacopter F550 Initially, a combined sensor, the SHT75, was installed at the hexacopter measuring air temperature and relative humidity at the same

time. The response time was 8 s with an accuracy of ±0.3 °C for air temperature and ±1.8 % for relative humidity. Data were logged with a Raspberry Pi B at 1 Hz. This sensor is a pre-calibrated, cheap and lightweight sensor and was applied in several UAV-based studies (Reuder et al., 2009; Bonin et al., 2013; Wildmann et al., 2014; Seidel et al., 2016). But after several test flights during the ScaleX campaign in summer 2015, this sensor was not used anymore because of the hysteresis. Therefore, data were not further analyzed.
In addition, a fast thermocouple was installed for high time resolution air temperature measurements. The used thermocouple was a butt welded type K (CHROMEGA/ALOMEGA CHAL-003, OMEGA, Stamford, CT, USA), one wire chromium nickel alloy and the other constantan, both with a diameter of 0.08 mm. Its measurement range is 0 °C to 60 °C with an output voltage of 50 mV per °C. A curcuit diagram is attached in the appendix (Fig. A2). The response time is better than 1 Hz in calm air with an accuracy of ±0.1 °C. Calibration against a reference thermometer (Thermapen, Eletronic Temperature Instruments Ltd, Worthing, UK) was done in the lab (Fig. 3.2). To this end, a styrofoam box with a light bulb and two fans for mixing the air were used. With changing the supply voltage of the light bulb its produced warmth differed to heat the box. Liquid nitrogen was used to cool the air in the box down. Calibration was done by increasing and decreasing the temperature in the box several times. The resulting calibration line for the thermocouple is for a range between around 5 and 30 °C (Eq. 3.1):

$$y = 1.0432\,x + 0.4899 \tag{3.1}$$

with x as the uncalibrated thermocouple output in °C and y as the calibrated value with the same unit. These calibrated air temperature data were also used together with pressure data from the autopilot for potential temperature (T_{pot}) calculations to get information about the stability of the atmosphere. Potential temperature is this temperature an air parcel would have bringing it dry adiabatically to a reference pressure (see Eq. 4.10 later). So its temperature is independent of pressure. Often, a reference of 1000 hPa is assumed (Kraus, 2004). The used pressure sensor was a MS5611-01BA03 (AMSYS, Mainz, Germany) and is able to resolve an altitude of 10 cm corresponding to a precision of about ±0.02 hPa.
Relative humidity was measured with a LinPicco A05 (IST AG, Ebnat-Kappel, Switzerland), which is a capacitive sensor having a response time better than 5 s and an accuracy better than ±3 %. The output signal ranges between 0–5 V for a humidity between 0 and 100 %. Calibration was already done by the com-

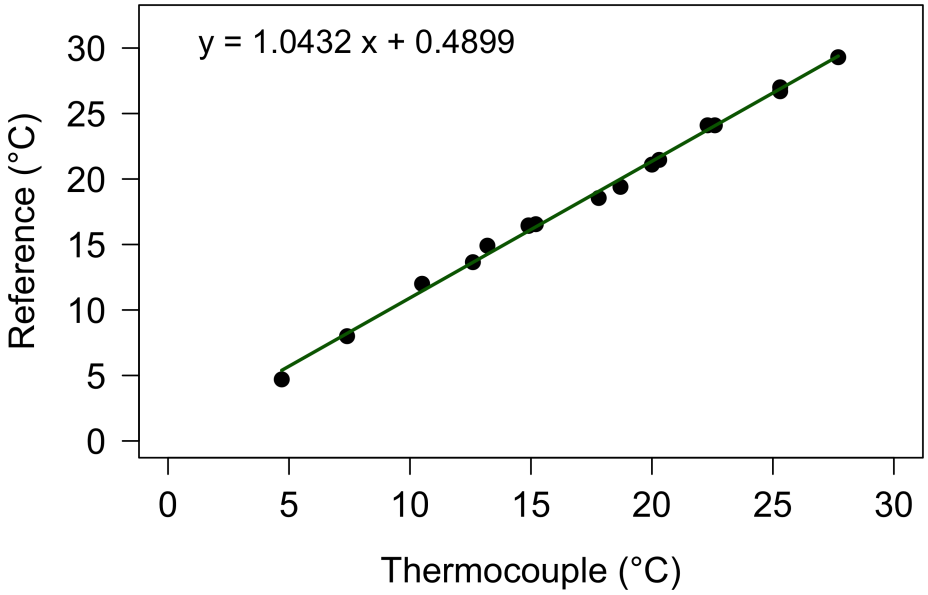

Fig. 3.2: Calibration of the thermocouple (x-axis) against a reference thermometer (y-axis) was done in the lab by increasing and decreasing the temperature in the calibration box several times. Black points represent the measurements and the green line shows the calibration line.

pany. Although the absolute accuracy was worse compared to the SHT75, the better response time was the decisive factor.

Land surface temperature was derived using the infrared thermometer CSmicro LT02 (Optris GmbH, Berlin, Germany). With this, the infrared radiation between 8 and 14 μm emitted from the Earth's surface is measured and dependent on the emissivity of the surface, its temperature is calculated. The temperature range is 0–350 °C which corresponds to an output signal between 0 and 3.5 V. This sensor has an accuracy of ±1.5 °C and a precision of ±0.75 °C. The diameter of the emitting area is half the distance of the sensor to the object. This means, that measuring from 5 m a.g.l. leads to a diameter of the emitting area of 2.5 m.

Those three sensors were installed at the hexacopter F550 and data were logged at 10 Hz. To merge the sensor data with the flight data of the autopilot afterwards, a GPS (GPS-Logger 2, SM-Modellbau, Wielenbach, Germany) was connected to the data acquisition board UniLog 2 (SM-Modellbau, Wielenbach, Germany) for time stamp information. Since this board was only able to record 0-3.3 V, relative humidity could only be measured up to 65 %.

The conversion equations (Eqs. 3.2, 3.3, 3.4) from Volt to degree celsius and percent, respectively, are:

$$T_a\ (^\circ C) = \frac{(out_{mV}/1000) - 0.978}{0.05} \tag{3.2}$$

$$LST\ (^\circ C) = \frac{out_{mV}}{10} \tag{3.3}$$

$$RH\ (\%) = \frac{1}{50 \cdot out_{mV}} \tag{3.4}$$

while for out_{mV} the output of the sensors has to be inserted.

Pro X-3 Lite For vertical in situ methane investigations, an open path sensor based on wavelength modulation spectroscopy with a weight of 1.6 kg (Golston et al., 2017) was installed at the Pro X-3 Lite hexacopter (Stein Elektronik, Jülich, Germany) in cooperation with the Princeton University, USA. The lightweight methane sensor consists of a sensor head with a 3.27 μm GaSb distributed feedback laser (Norcada, Edmonton, Canada) as well as an optically immersed HgCdTe photodetector (Vigo Systems S.A., Ozarow Mazowiecki, Poland) and an electronic box for processing the signals. Its in-flight precision was 0.01 ppm at a 1 Hz averaging time. Directly outside the radiation absorption path length, the temperature and relative humidity sensor HYT271 (Innovative Sensor Technology IST AG, Ebnat-Kappel, Switzerland) was installed. Further information about the methane sensor is provided in Golston et al. (2017).

3.3.2 Wind Estimation

Multicopters move through the air by setting a tilt angle (γ) towards the flying direction with the magnitude of tilt angle roughly proportional to speed. This angle is also changing for compensation of wind variations during the flight. Therefore, without using an additional sensor for wind measurements, estimation of both horizontal wind speed and direction was possible with onboard sensors for the vehicle's attitude control by measuring the pitch (for- and backwards), roll (left and right) and yaw (orientation to north) angles. In contrast to an aircraft, which is controlled by setting a true air speed, a multicopter is flying with a given ground speed resulting in a varying true air speed. This relationship is shown in the wind triangle (Fig. 3.3).

The ground (Gr) vector represents the speed and direction of the multicopter's movement determined by the GPS, while the true air speed (TAS) vector represents the actual speed and direction the multicopter is heading to. The deviation of Gr and TAS is caused by the wind. Assuming hovering, the tilt angle is only a result of the wind and so the TAS vector is contrary to the wind

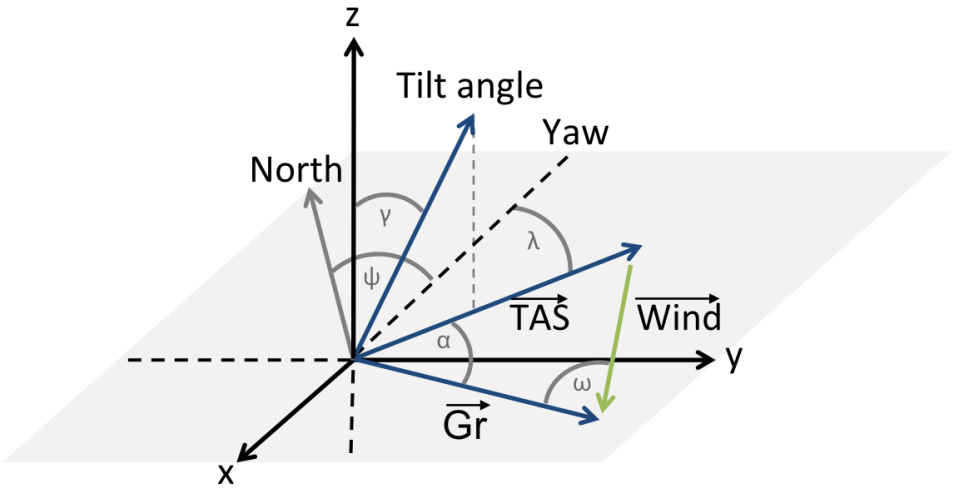

Fig. 3.3: Relationship between the tilt angle γ of the multicopter and the wind triangle with true air speed (TAS) vector, ground (Gr) vector and wind vector with corresponding angles α and ω. Pitch angle is in x-axis and roll angle in y-axis direction. Yaw (Ψ) is the viewing direction of the multicopter relative to north and the angle between TAS and yaw is λ.

vector; the ground vector is zero. Consequently, in the easiest case the direction of TAS represents the horizontal wind direction and the length of the TAS vector the horizontal wind speed. Equations applied for the wind calculation are based on Neumann and Bartholmai (2015) and shortly explained in the following.

First, the multicopter's tilt angle γ was calculated from roll and pitch angles and then projected to the xy-plane, which results in the true air speed vector after insertion into the regression function (Eq. 3.7). Then, its direction was calculated relative to the viewing direction of the multicopter (yaw angle (Ψ)) and is given by the angle λ. TAS direction was determined by the sum of Ψ and λ in case the TAS vector is on the right side of the viewing direction ([Ψ,Ψ + 180°]). In the other case, this sum was subtracted from 360° and in both cases the result has to be within 0° and 360°. The angle α represents the difference between the ground and TAS vectors. Using the law of cosine, wind speed was calculated with Eq. 3.5:

$$WS = \sqrt{|\overrightarrow{TAS}|^2 + |\overrightarrow{Gr}|^2 - 2 \cdot |\overrightarrow{TAS}| \cdot |\overrightarrow{Gr}| \cdot cos(\alpha)} \tag{3.5}$$

Finally, the angle ω has to be determined by using the law of cosine for wind direction. In case the flight direction (GC) $< 180°$, ω is subtracted from the

flight direction and added in case of GC $> 180°$ (Eq. 3.6):

$$WD = GC \pm \omega + 180° \tag{3.6}$$

Adding 180° to the result is needed because wind direction is the direction from where the wind is coming and therefore the opposite direction the wind wind vector is pointing to. Neumann and Bartholmai (2015) used wind tunnel experiments to determine the regression function. In contrast, in our approach the length of the TAS vector was determined by relating tilt angles to specific true air speeds during different flight experiments. The assumption was that without wind the true air speed corresponds to the flight speed measured with the GPS (GPS speed or ground speed), which has an accuracy of 0.1 m s^{-1}. The multicopter's tilt angle was calculated by using pitch and roll angles. Their accuracy was better than 0.1°. Using racetrack flights, the regression function was experimentally determined during calm wind conditions with wind speeds below 1 m s^{-1}. The track had a length of 120 m and had been flown six times on average for several ground speeds between 2 m s^{-1} and 8 m s^{-1}. While the ground speed was kept constant ($< \pm 0.2$ m s^{-1}) by the GPS, the variability of the assigned tilt angle was dependent on atmospheric conditions. To avoid an offset in the regression function the multicopter was balanced out. The resulting regression function is shown in Fig. 3.4 with the following equation (Eq. 3.7):

$$TAS = 0.8102 \cdot \gamma^{0.94} \tag{3.7}$$

The root-mean-square error (RMSE) of TAS determination was ± 0.3 m s^{-1}. Based on this error for TAS, the RMSE of the tilt angle was $\pm 0.4°$, which is similar to the one of Neumann and Bartholmai (2015). This mean error of TAS leads to a higher relative error for low wind speeds than for higher wind speeds.

With this equation, horizontal wind speed and wind direction were estimated from 1 Hz data and were averaged with a moving window over 10 s for further smoothing. To determine the inaccuracy caused by a wind speed up to 1 m s^{-1} during the experimental flights, the variability of the tilt angle was analyzed during hovering under calm wind conditions (< 1 m s^{-1}). This led to an uncertainty of 0.7° $\pm 0.3°$ corresponding to a true air speed of 0.7 m s^{-1} ± 0.3 m s^{-1}, which resulted in an overall accuracy of TAS estimation of 0.7 m s^{-1} ± 0.6 m s^{-1}.

Parts of the wind estimation were done in the master thesis of Karina Krampf (Krampf, 2017), especially flight strategies for the regression function and the

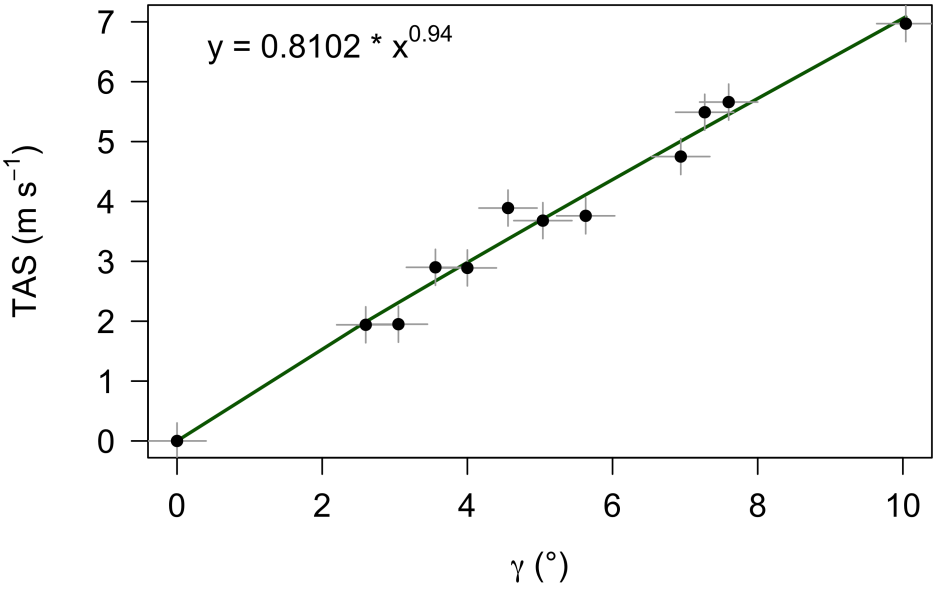

Fig. 3.4: Regression function of relationship between true air speed (TAS) and tilt angle (γ) experimentally determined with racetrack flights during calm wind conditions. The green line represents the fitted regression function and the error bars indicate the standard deviation of $\pm 0.4°$ for the tilt angle and ± 0.3 m s^{-1}, respectively.

characterization of the hexacopter's flight behavior.

3.3.3 Tube and Methane Analyzer

For the campaign in 2015, methane investigations close to the tower were done by raising a tube up in the air (Fig. 3.5). A 40 cm long aluminum tube (3.2 mm outer diameter, 1.2 mm inner diameter) was installed at the multicopter with the inlet about 30 cm above the propellers. This was attached airtight to an additional sampling line (PTFE, 3.2 mm outer diameter, 2 mm inner diameter, 70 m long) with the same characteristics as at the tower and was connecting the CRD spectrometer and the multicopter. The 70 m sample line was flushed at a flow rate of 350 sccm min^{-1} (calibrated for 0 °C and 1013.25 hPa) of which 200 sccm min^{-1} were drawn by the CRD analyzer. This resulted in a residence time of approximately 38 s in the tube. At 50 m a.g.l., the tube was an additional payload of about 650 g, which led to a takeoff weight at the upper recommended limit. Thus, the maximum ascent height was limited by the payload capacity of the multicopter and simultaneously reduced to the multicopter's flight time.

Alvarado et al. (2017) experimentally determined a distance of 40–45 cm above the multicopter, where the influence of the rotors to air speed decreases signi-

Fig. 3.5: Hexacopter F550 with 70 m tube at about 20 m above ground (Picture taken by Klaus Schäfer).

ficantly. So, the recorded methane mixing ratio is actually not a point measurement but valid for a volume < 1 m^3.

3.4 Flight and Sensor Data Processing

On the one hand, data from the multicopter flights were saved onboard on a SD-card as well as saved directly by the Mission Planner while data were transmitted via telemetry. The problem of the latter one was that the telemetry link is dependent on atmospheric conditions, distance and used frequency. Therefore, onboard stored data were used, downloaded from the autopilot and converted into a *.log and *.kmz file with the Mission Planner. The former is a text file containing the flight data and the latter can be directly opened and visualized with Google Earth.
In the text file, each sensor has an identifier followed by the sensor data and a time stamp counting the seconds (milliseconds) from the moment the data logging was started. The GPS has an additional time stamp corresponding almost to UTC. While for all flights which were done before 1 July 2015, the difference between UTC and GPS time was 16 s (UTC = GPS − 16 s), the difference increased by 1 s (UTC = GPS − 17 s) afterwards. Depending on the used GPS device, the output time of the GPS is already in UTC and then,

no manual correction has to be done.

Using the open-source software R, the text files were rearranged to have the time in the rows and the sensor data in the columns. In a next step, the data from the second acquisition board were merged with the flight data according to the GPS time (UTC, respectively). Since the sensors provided data at different frequencies (50 Hz, 10 Hz, 5 Hz) these were averaged to 1 Hz and saved to a new text file. The corresponding R-script is attached in the appendix (A2). For the experimental flights in 2015, data merging was done manually using pressure data as an indicator for the start of the multicopter. Having this point in the flight data and the sensor data, columns could be attached to each other. The last step was to extract only relevant data during the flights by using the throttle information (motor thrust) and in case two flights were in one file they were separated into to files.
Everything else as plotting or calculation of further parameters was done with those files. The naming of the files was "YYYY−MM−DD_HH−MM−SS", which corresponds to the first time stamp of the file.

3.5 Flight Regulations

Since some years, there are flight regulations for the operation of UAVs without a combustion engine. In case the operation is not for sport or leisure time activities an "Allgemeine Aufstiegsgenehmigung" is necessary for which the aviation authority (in this case Luftamt Südbayern) is responsible. Having a take-off weight above 5 kg, an additional permission is necessary. By default, flights are only allowed in the uncontrolled air space up to 100 m a.g.l. during daytime. For scientific purposes, it was possible to extend it to uncontrolled air space during day- and nighttime. But the rule of flying in line-of-sight has to be obeyed anyhow. At all times, manned aircraft have the right of way. It is not allowed to fly close to an airport (1500 m), above a gathering of people, accident sites, residential estates, industry and state buildings, and nature reserve areas. In addition, the land owner's permission for start and landing has to be obtained.
Since both hexacopters weighted below 5 kg, an additional flight permission was not necessary, which was the intention when choosing the UAVs and sensors.

4 Methods and Calculations

4.1 Statistical Analyses

Interpolation For the analysis, flight data were used within the area of 47.83191° N, 11.05845° E (lower left coordinate) and 47.83298° N, 11.06294° E (upper right coordinate) with a grid resolution of 10 m west–east direction and 50 m north–south direction. Due to the fact that within this grid the data points of the flights differed in position and number (±5) an interpolation was necessary for easier comparison of the flights.
Therefore, the three long legs (350 m) were interpolated using the method IDW (Inverse Distance Weighting) interpolation based on the R package *gstat*. To find the best parameters a sensitivity analysis was done. Different values for two parameters were used, the first defines the maximum number of neighbors used for the calculation and the second defines the power for weighted calculation. Applying the RMSE to the results, the best set of parameters was found. The minimum of RMSE was for $neighbors = 2$ and $power = 1$. This means the variables (e.g. air temperature or humidity) in each grid cell were calculated by an average of three data points all having the same weight.

Pattern correlation As a first indicator of the similarity of measured patterns within one variable over different heights and time of day, Pearson's correlation coefficient was used. This is a measure of similarity to compare two different data sets. Possible values range between -1 and $+1$, while the former indicates a negative correlation and the latter a positive correlation. No correlation is indicated with the value 0. The pattern correlation is often applied in climate change studies, for example, to distinguish between different causes of climate change (Mitchell et al., 2001). There are two types – the uncentered and the centered pattern correlation. The difference is that in the latter the data sets are centered around their mean value prior to correlation (Santer et al., 1993; Mitchell et al., 1995). In this thesis, the centered method was used because removing the mean facilitates the identification of pattern similarities over time.

Principle Component Analysis The principle component analysis (PCA)

is a multivariate statistical technique to reduce the dimensionality of a data set. The data set contains observations, which are described by dependent variables. To this end, the initial variables are summarized to linear combinations of the variables while extracting the most important information. At the same time, the number of variables is reduced, the so-called *principle components* (PCs), then the structure of the data set is analyzed (Abdi and Williams, 2010). The PCs are ranked according to their explaining variance of the total variance, i.e. PC1 explains the largest fraction, PC2 the second largest fraction and so on. Taking the first two PCs together, they usually explain more than 60 % of the variance. The number of PCs taken for further analysis is chosen depending on how much variance should be explained with the PCs.
In this thesis, the *prcomp* function from the R-package *stats* were used to calculate the PCs and with the *factoextra* package the data were visualized. To this end, the first component was represented on the x-axis and the second component on the y-axis. Each variable was plotted with a vector; its direction indicates the importance for the first two components and its length the importance for the whole observation. The longer the vector, the more important the variable (Abdi and Williams, 2010).

Gaussian Error Propagation This method estimates the overall uncertainty based on the uncertainty of input variables. Both variables are needed for the calculation and thus both accuracies contribute to the error. To this end, the equation is differentiated for each variable and multiplied by the corresponding standard deviation according to the equation (Papoulis, 1984; Marx et al., 2008):

$$\sigma_f = \sqrt{\left(\frac{\partial f}{\partial x_1}\right)^2 \cdot \sigma_{x_1}^2 + \left(\frac{\partial f}{\partial x_2}\right)^2 \cdot \sigma_{x_2}^2} \tag{4.1}$$

with f as function and x_1, x_2 as variables. The equation is only valid for uncorrelated variables. In case of more than two variables, derivation and standard deviation have to be added under the root. As an example, when calculating potential temperature its uncertainty can be estimated by the accuracies of air temperature and pressure measurements.

4.2 Surface Energy Balance and ET Estimation

The surface of the Earth is the major surface area to transform energy (Fig. 4.1). Short-wave radiation from the sun impacts on the Earth's surface where it is partly reflected (albedo) and partly absorbed. The absorbed energy is con-

verted into heat, which increases the temperature of the Earth's surface. Together with the long-wave radiation from particles, clouds and gases in the atmosphere, the absorbed short-wave radiation sums up to the total incoming energy. Depending on the temperature of the Earth's surface, long-wave radiation is emitted into the atmosphere. Since the surface gets more energy than it emits, there is a surplus, which is on the one hand transported into the soil leading to the ground heat flux (G) and on the other hand into the atmosphere as turbulent fluxes of sensible (H) and latent heat (LE). While the sensible heat flux warms the atmosphere from the "bottom", the latent heat flux transports energy into the atmosphere through evaporation (Oke, 1987; Foken, 2016).
Therefore, the energy balance is described with the following equation (Eq. 4.2):

$$-R_{net} = H + LE + G \tag{4.2}$$

with R_{net} as net radiation including short- and long-wave radiation terms: $R_{net} = S_{in} - S_{out} + L_{in} - L_{out}$ (see Fig. 4.1). The energy balance components describe flux densities and have the unit Wm^{-2}, while the sign indicates the direction of the flux. Positive fluxes are directed away from the surface and negative fluxes towards the surface. The ratio between the sensible and latent heat flux (H/LE) is called the Bowen ratio (β).
Generally, the net radiation is directed towards the surface during daytime and away from it during nighttime. For the other fluxes this is the other way round (Oke, 1987).

The already mentioned eddy covariance method is a micrometeorological technique to directly measure the turbulent fluxes of sensible and latent heat by measuring the vertical wind component and the quantity of interest. Calculating the covariance between the perturbations of those variables results in the turbulent fluxes (Aubinet et al., 2012). In order to know the available energy and thus close the energy balance, radiation and ground heat flux are measured as well. All the fluxes are often available as half-hourly averages. Shorter averaging times have the problem that not all turbulent eddies are captured and so the turbulent fluxes are underestimated compared to the available energy ($R_{net} - G$). In contrast, longer averaging times include the large eddies too, but then the required atmospheric stationarity may not be fulfilled anymore. Comparing the available energy to the sum of the turbulent fluxes, the energy balance closure can be determined, while a result of 1 would be a closed energy balance (Finnigan et al., 2003). Since in reality this is not often the case, closure methods are needed. In this thesis, the Bowen ratio method was used because it does not change the ratio between sensible and latent heat flux.

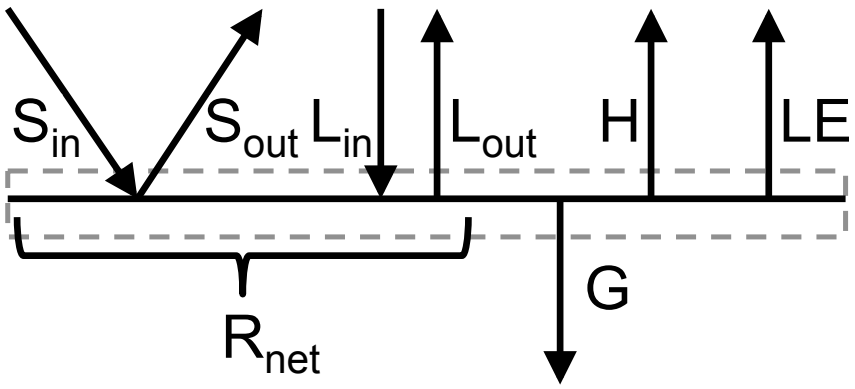

Fig. 4.1: Schematic representation of the terms of the energy balance components. The Earth's surface is plotted as a horizontal black line. Short-wave (S_{in}, S_{out}) and long-wave (L_{in}, L_{out}) radiation add up to the net radiation R_{net}, which is the available energy. This is transported into the ground (G) and into the atmosphere (H, LE). The grey dashed rectangle stands for the energy storage in the soil, vegetation, water and air close to the surface. Own graphic, adapted from Foken (2016).

The available energy surplus is partitioned in order to keep the existing Bowen ratio (Twine et al., 2000).

Since there were no turbulence measurements available based on multicopter data, another method, a so-called residual method, was applied to estimate the energy balance. To this end, net radiation, ground and sensible heat flux were calculated according to equations 4.3–4.5. The surface is assumed to be a uniform layer without differentiating between soil and canopy when estimating H. Therefore, this method is known as a one-source energy balance model (OSEB). In contrast, a two-source energy balance model (TSEB) distinguishes between the surface temperature of soil and canopy. The latent heat flux represents the residual energy in both the OSEB and TSEB in order to close the energy balance (Eq. 4.6). Actually, the errors done by estimating R_{net}, G and H are also included in LE. The equations of the OSEB are as follows (Brutsaert, 1975; Jackson, 1985; Kustas et al., 1989; Norman and Becker, 1995):

$$R_{net} = (1 - a) \cdot S_{in} + \epsilon_a \cdot \sigma \cdot T_a^4 - \epsilon_s \cdot \sigma \cdot LST^4 \tag{4.3}$$

$$G = i \cdot R_{net} \tag{4.4}$$

$$H = \frac{c_p \cdot \rho \cdot (T_{aero} - T_a)}{r_{ah}} \tag{4.5}$$

$$LE = R_{net} - G - H \tag{4.6}$$

with albedo (a), downward short-wave radiation (R_s in $\mathrm{Wm^{-2}}$), atmospheric emissivity (ϵ_a), Stefan-Boltzmann constant ($\sigma = 5.67 * 10^{-8}$ $\mathrm{Wm^{-2}}$ K^{-4}), surface emissivity (ϵ_s), $i = 0.0812$ which is a constant and was derived from the relationship between R_{net} and G from daytime EC data during the measurement period, volumetric heat capacity ($c_p\rho$ in J $\mathrm{m^{-3}}$ $\mathrm{K^{-4}}$), aerodynamic temperature (T_{aero} in K) and resistance to heat transfer (r_{ah} in s $\mathrm{m^{-1}}$).

The key variable, which has to be determined in sensible heat flux calculations, is the resistance to heat transfer (r_{ah}) in order to relate the measured radiometric temperature, i.e. LST, to the aerodynamic temperature. In case of a highly vegetated surface the resistance to heat transfer can be assumed to be constant, which is not the case for partially covered surfaces. The r_{ah} is derived from roughness length, wind speed and stability according to the following equation (Kustas et al., 1989; Li et al., 2009):

$$r_{ah} = \frac{(ln((z-d)/z_{om}) + kB^{-1} - \psi_s) \cdot (ln((z-d)/z_{om}) - \psi_m)}{k^2 \cdot WS} \tag{4.7}$$

with measurement height (z in m), displacement height (d in m), resistance to momentum transport (z_{om} in m), added resistance to heat transfer (kB^{-1}), stability correction for heat (ψ_s) and momentum (ψ_m), von Karman constant ($k = 0.4$) and wind speed (WS in m $\mathrm{s^{-1}}$). Stability correction is zero for neutral atmospheric conditions, positive for stable and negative for unstable conditions. According to Thom (1972), the exchange of mass and heat is less effective than the one of momentum leading to a greater aerodynamic resistance for the former one (z_{oh} in m) than the latter one (z_{om} in m). The parameter kB^{-1} expresses this difference in aerodynamic resistance ($kB^{-1} = ln(z_{om}/z_{oh})$).

Most of the variables were derived from multicopter measurements, but short-wave radiation and Obukhov length for stability correction were used from the EC station. The relationship between R_{net} and G was derived from EC station values during the whole measurement period as well. For kB^{-1} two approaches were used. The one after Bastiaanssen et al. (1998) uses a constant value of $kB^{-1} = 2.3$ and after Kustas et al. (1989) this value is dependent on wind speed, the difference between LST and T_a and an empirically determined value of 0.17.

In order to get the evapotranspiration rate, the latent heat flux together with the latent heat of vaporization ($\lambda_v = 2.5 * 10^6$ J $\mathrm{kg^{-1}}$) and density of wa-

ter (ρ_w = 1000 kg m^{-3}) is used (Oke, 1987). Since the latent heat flux was estimated as an instantaneous value, the evaporative fraction (EF) has to be determined first by using the average of available energy within 24 hours (Chávez et al., 2008):

$$EF = \frac{LE}{R_{net} - G} \tag{4.8}$$

$$ET = \frac{EF}{\lambda_v \cdot \rho_w} \tag{4.9}$$

In hydrology, ET is normally given in mm per hour or day.

4.3 Atmospheric Stability and Flux Estimation

Atmospheric stability The stability of the atmosphere was determined by using the potential temperature with the following equation (Foken, 2016):

$$T_{pot} = (T_a + 273.15)\left(\frac{p_0}{p}\right)^{(R_L/c_p)} \tag{4.10}$$

with T_{pot} as potential temperature (in K), T_a as air temperature (in °C), p is air pressure (in hPa), p_0 is reference air pressure (hPa), the gas constant of air R_L = 287 J kg^{-1} K^{-1} and specific heat capacity at constant pressure c_p = 1003 J kg^{-1} K^{-1}. The reference air pressure in this thesis equals the ground pressure and thus is not constant, but dependent on weather conditions.
Furthermore, the gradient Richardson number (Ri) can also be used for atmospheric stability, which indicates the transition from laminar to turbulent flow (Stull, 1988):

$$Ri = -\frac{g}{T_{pot}} \frac{\Delta T_{pot}/\Delta z}{(\Delta WS/\Delta z)^2} \tag{4.11}$$

with gravity g = 9.81 m s^{-2}, z is height a.g.l. (m) and WS is horizontal wind speed (m s^{-1}). The Richardson number is dimensionless, while numbers $<$ 0.2–0.25 indicate unstable atmospheric conditions with turbulence and values above this critical number point to stable conditions without turbulence.

Determination of the nocturnal boundary layer height is difficult, because sometimes there is no clear marker to the residual layer (Stull, 1988). This information, however, is essential to estimate nocturnal fluxes. Different approaches are available summarized by Seibert et al. (2000). Therefore, several variables were used in this thesis for determination of the NBL height following Choi et al. (2011).

The most reliable criterion to determine the NBL height in this thesis was thought to be the vertical potential temperature gradient. Under stable conditions, and so within the NBL, T_{pot} increases with height. In case of constant or decreasing values with height, the top of the inversion and so the top of the NBL height is reached. Similar to this is the change in T_{pot} with change in height $(T_2 - T_1)/(z_2 - z_1)$. Positive values point to stable stratification, while values close to zero ($\pm$0.1 K) define the NBL height.
In addition, the Richardson number can be used too, but considering the uncertainties in estimating the wind speed, this value is not as reliable as T_{pot}. For decision-making, both wind speed and direction and humidity changes were also taken into account if necessary.

Flux estimation Sensible heat (Bonin et al., 2013) and methane (Denmead et al., 1996, 2000; Emeis, 2008) fluxes were calculated from the multicopter data. For both vertical profiles within the NBL from two successive flights (time difference one hour) were necessary to determine nocturnal fluxes.
The sensible heat flux was vertically integrated to the NBL height and represents a horizontally as well as temporally average (Bonin et al., 2013):

$$H(z) = \sum_{z/\Delta z}^{NBL_z/\Delta z} c_p \rho \frac{\Delta T_{pot}}{\Delta t} \Delta z \tag{4.12}$$

where NBL_z is the NBL height, $\Delta z = 1$ m and ρ is air density, which was calculated from air temperature and pressure data. Since an ascent speed of 1.5 m s^{-1} was used, there was no value for every 1 m step. Therefore, missing values were interpolated with adjacent values by calculating the average. In this approach it is assumed that the vertical wind component is zero and so the flux only depends on potential temperature change over space and time. This means that energy loss leads to lower T_{pot} over time, which corresponds to a negative flux directed towards the surface. This can be different throughout the whole vertical profile.

For the NBL method, concentration changes of successive flights were integrated over the NBL height assuming that horizontal advection was negligible under calm atmospheric conditions (Denmead et al., 1996):

$$F_C = \int_0^{NBL_z} \frac{\Delta C}{\Delta t} dz \tag{4.13}$$

with F_C as the surface flux, in this case the CH_4 flux, and $\Delta C/\Delta t$ is the gas concentration change with time.

4.4 Backward Trajectories and Footprint Estimation

HYSPLIT Measuring gas concentration of for example methane as in this thesis, meso-scale wind fields are important to interpret the results in order to know where the origin is of air masses with high concentrations. The HYSPLIT (HYbrid Single-Particle Lagrangian Integrated Trajectory) model developed by the National Oceanic and Atmospheric Administration (NOAA) Air Resources Laboratory (ARL) was designed to calculate back- and forward trajectories as well as gas concentrations (Draxler and Hess, 1998; Stein et al., 2015). Such a trajectory is defined as the time-integrated advection of an air particle. In other words, the model reconstructs the way back of an air parcel from where it was coming by using gridded meteorological data. Different data sets can be chosen as input with varying spatial resolution. For Europe, only global data sets can be used with a resolution of 0.5° or 1° (GDAS).

Flux Footprint Prediction The Flux Footprint Prediction (FFP) is a two-dimensional parameterization, which provides the extent, width and shape of a footprint even for long time series with the possibility of calculating the derivation of footprints (Kljun et al., 2015). This version of the model is an updated version of the Lagrangian stochastic particle dispersion footprint model (Kljun et al., 2002). It is applicable for different measurement heights as well as for fluxes derived from airborne measurements and valid for various boundary layer conditions. Therefore, it provides footprint estimates for a lot of real-case applications. Necessary input variables can be derived from standard flux tower setups or airborne measurements. The code is freely available and can be run with R, Python and MATLAB. In this case, the R code was chosen because this program was also used for other analyses. To run the model, several input variables have to be inserted such as mean horizontal wind (WS_{mean}), standard deviation of lateral wind speed (σ_v), friction velocity (u_*), Monin-Obukhov length (L), boundary layer (NBL_z) and measurement height (z). The specification of further variables as wind direction or geographical coordinates is possible as well as the domain and grid size, and the percentage of footprint fractions.
Although this model is not optimized for stable conditions, it gives an idea about the footprint's extent setting the input variables as close to stable conditions as possible. To get a range of footprints, NBL heights and wind speed was varied for the calculations, while the other variables were kept constant. The measurement height was set relative to the NBL height ($0.2 \cdot NBL_z$,

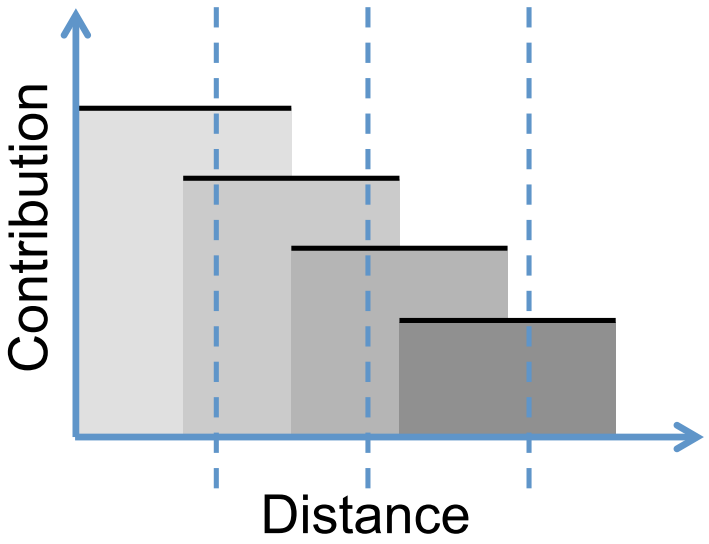

Fig. 4.2: Schematic representation of the calculation of a cumulative footprint for footprints at several vertical levels. The dashed blue lines show the discrete bins of the upwind distance and the black lines the extent of the footprints in upwind direction.

$0.4 \cdot NBL_z$, $0.6 \cdot NBL_z$, $0.8 \cdot NBL_z$). Applied values for the NBL height were 80, 100 and 120 m and for mean wind speed 1, 2 and 3 m s^{-1}. The other values were chosen according to the available data from the EC measurements at the tower ($L = 5$, $u_* = 0.2$, $\sigma_v = 0.07$). Since fluxes were estimated from vertical profiles, a combination of several footprints represent the actual footprint of the profile. This cumulative footprint was derived from four footprints at heights mentioned above. To this end, the contribution at each upwind distance was summed for the footprints, while discrete steps of 100 m were used. This is shown schematically in Fig. 4.2 with the place of measurement at the origin, where the x- and y-axes meet. The black horizontal lines represent the extent of the footprints in upwind direction, so the distance to the measurement point. On the y-axis, the magnitude of contribution of the footprints is shown. High contribution and a close distance to the measurement point indicates a measurement height near the ground, lower contribution and larger distance points to a higher measurement height. The blue dashed lines are the 100 m bins. So, for example, in the closest bin to the measurement two footprints partly contribute and therefore their contribution is summed. The same is true for the other bins and then the result is a cumulative footprint.

5 Feasibility of Hexacopter Measurements

In order to address the scientific research objectives of this thesis, the feasibility of a multicopter-based approach is assessed to achieve mobile and flexible investigations of hydrometeorological variables and methane concentrations at the same time. Air temperature and relative humidity were measured with installed onboard sensors, wind was estimated by using the vehicle's attitude control. For methane investigations, two different approaches were tested: first by pulling up a tube with the hexacopter, while the tube is connected to a methane analyzer on the ground and second by using an onboard open-path methane analyzer. To integrate the necessary sensors, two hexacopters were used differing in their size and payload capacity (see chapter 3.2).

5.1 Flight Strategies

Three-dimensional investigations of meteorological variables, methane concentrations and land surface temperature require specific flight strategies. Therefore, the flight pattern has to be adapted to the purpose of the flight as well as to the used sensors. In this regard, a balance between fast sensors and long flight times has to be determined. The faster a sensor, the faster the flight speed can be chosen and consequently a larger area can be covered. This is true for both horizontal and vertical flights. During the campaign in 2015, appropriate flight patterns were investigated and in 2016, all flights were repeated by using the same flight patterns, i.e. one for horizontal and one for vertical flights.

With a vertical ascent and descent speed of 2.5 m s^{-1} for example, the SHT75 sensor showed a hysteresis because of the response time of 8 s. Even with a lower speed of 1.5 m s^{-1}, ascent and descent data were different, especially when flying through an inversion. However, the thermocouple with a response time of less than 1 s was appropriate for those speeds. To counteract the hysteresis of the SHT75, a hover time every 10 m for 10 s was included. But considering a vertical height of 100 m, the continuous profile can be flown

three times in the same time as the profile with hover time once.
For wind estimation, both type of profiles worked, but only for ascents because downwards the multicopter had to fly through its own downwash, which caused artificial turbulence. In addition, hovering close to the ground (below 5–6 m) led to higher variability because of the reflection of the downwash at the surface. Only for the tube-based methane measurements the hovering was necessary to ensure that the air in the tube was replaced at least once at a new height as well as to know the variability of the concentration. In contrast, the onboard methane sensor needed no hover time.
In the end, a vertical speed of 1.5 m s^{-1} was chosen for 2016 due to the lower response time of the new humidity sensor compared to the thermocouple and the generally better flight stability, especially the one of the Pro X-3 Lite because the payload was pushed to the limit. Additionally, the maximum height was extended to 150 m in order to reach an overlap with other instrumentation of about 100 m. To save time, only one ascent and descent were done.

With the horizontal flights, the extend of the soil moisture network (almost 350 m x 350 m) should be covered and at the same time with a high spatial resolution. According to the regression flights for the wind estimation (racetrack flights at different flight speeds), a horizontal flight speed of 5 m s^{-1} was appropriate to cover the whole area with four straight lines in north–south direction. Hover time was considered too, but for wind estimation this led to a high variability because of the acceleration and deceleration. But with a flight time of 9–10 min for each flight, more than half an hour was necessary to make those flights in three heights. Therefore, only half of the area was covered in the end. Since the west–east gradient between the road and the small stream was interesting to investigate, the flight pattern was chosen to consist of three straight west–east legs (350 m) with a distance of 50 m. So the three horizontal flights at 5, 10 and 15 m a.g.l. were done in less than 20 min. The relatively long legs in comparison to their distance was important for wind estimation because the wind estimation is not robust enough to rapid changes of the multicopter's tilt angle due to flight direction change.

5.2 Air temperature and relative humidity

During the ScaleX campaign 2015, the identification of appropriate flight patterns was focused in order to account for their time resolution and to prevent a hysteresis effect. In addition to that, vertical profile comparisons were done between different airborne platforms using in situ sensors. An example of the

vertical T_a profile comparison is shown in Fig. 5.1, which was published in Wolf et al. (2017). At two time periods, the hexacopter F550, a fixed-wing UAV and the microlight aircraft measured vertical air temperature profiles at the investigation site. Though the measurements were not taken at exactly the same time and location, the temperature measurements of all three systems mostly agreed within 0.5 °C for the overlapping heights. Therefore, the aerial vehicles complemented each other to obtain a seamless representation of the vertical structure from the ground up to the free troposphere (only the first 300 m are shown).

Looking at the two hexacopter-based vertical profiles more detailed, two different flight strategies can be distinguished. In the early one, a hovering time of 10 s every 10 m for ascent and descent was included, while the later one was without hovering time and up to 150 m a.g.l. instead of 100 m. As mentioned in chapter 5.1, the second strategy was applied for the campaign in 2016, because of a better flight stability and more overlapping heights for comparison with other instrumentation.

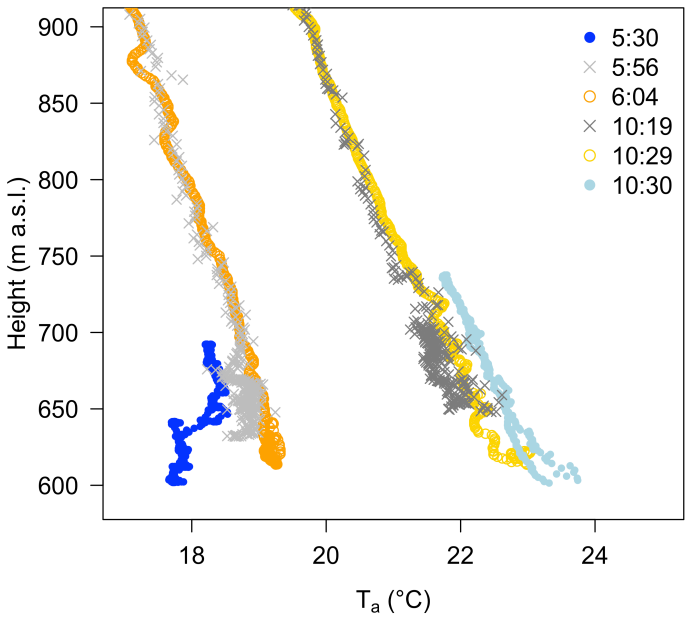

Fig. 5.1: First 300 m of vertical air temperature (T_a) profiles determined by the hexacopter (shades of blue), fixed-wing UAV (yellow and orange), and microlight aircraft (grey) on 15 July 2015 (start times given in UTC).

During the ScaleX campaign 2016, a comparison was done while hovering close to the 9 m tower where the feasibility of the wind estimation was tested. Air temperature measured over 5 min with the thermocouple had an average of 28.5 °C, the sonic temperature at the tower had 27.6 °C and the EC station

28.7 °C. This indicated a warm bias of the thermocouple compared to the sonic temperature, which is derived from sonic speed in the air. After normalization, the RMSE was ±0.3 °C between hexacopter and tower. Averaged relative humidity at the hexacopter was 41.5 %, while at the EC station it was 43.1 %. This difference was within the accuracy of the hexacopter's humidity sensor.

5.3 Wind

To demonstrate the functionality of the wind estimation based on the attitude control sensors of the multicopter, a comparison was done to an 3D ultrasonic anemometer (uSonic3, Metek GmbH, Elmshorn, Germany) installed at a 9 m tower having an accuracy of 0.1 m s^{-1} and 2° at 5 m s^{-1}, respectively. During windy conditions (3–5 m s^{-1}) the multicopter was hovering for 5 min close to the tower at a distance of approximately 5 m (Fig. 5.2). This horizontal distance as well as the 9 m height of the measurements ensured that the multicopter's downwash neither had an influence on the multicopter itself nor on the anemometer. For calm wind conditions, influences of the downwash were detected up to 5–6 m a.g.l.

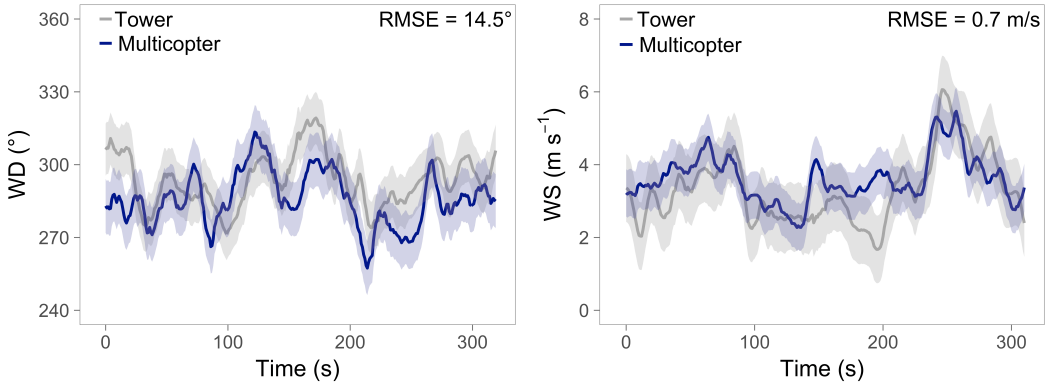

Fig. 5.2: Wind direction (WD) and speed (WS) comparison between tower (grey) and multicopter (blue) at 9 m a.g.l. over 5 min. The colored bands around the lines represent the standard deviation of each time series.

The multicopter derived wind direction showed a standard deviation of ±11.1° and ±0.7 m s^{-1} for wind speed within a hovering time of 5 min. During the same time, the anemometer's wind direction varied by ±10.6° and wind speed by ±1 m s^{-1}. The difference between the multicopter and tower measurements both averaged over 5 min was 7.7° and 0.3 m s^{-1}. For both time series the 10 s moving average was applied resulting in a RMSE between multicopter and tower of 14.5° and 0.7 m s^{-1}, respectively. Both changes in wind speed

and direction could be captured by the multicopter. The highest deviation was between 150 s and 200 s with differences of about 30° and 2 m s^{-1}, respectively. The multicopter only reacts to turbulent elements, the so-called eddies, with a size equal to the multicopter or larger. Since the volume of the multicopter is larger compared to the measurement path of the sonic anemometer, the multicopter does react to less eddies and therefore cannot capture the full range of wind speed. In addition, the multicopter has inertia due to its weight. Consequently, the wind speed deviations measured by the multicopter should not be used as information about atmospheric turbulence.

In addition to the side-by-side measurements, wind estimation from vertical profiles was compared to lidar and sodar measurements as well as EC station data for near ground information (Fig. 5.3).

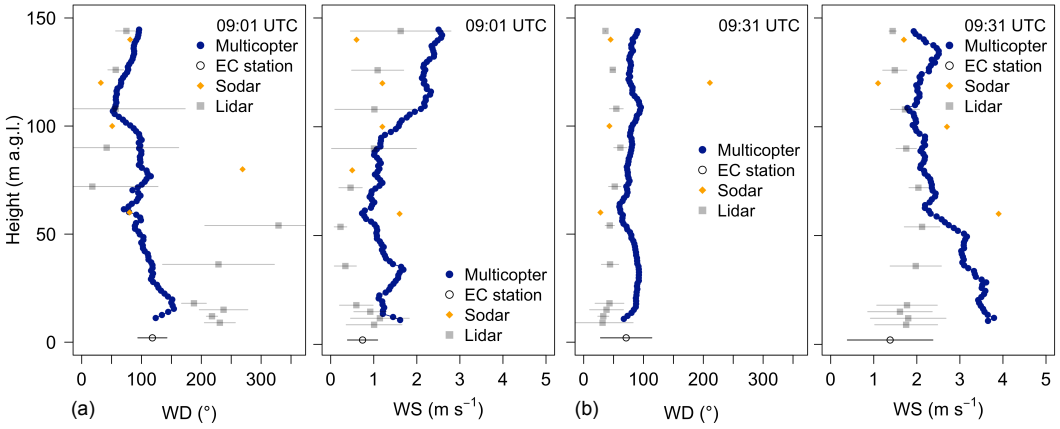

Fig. 5.3: Wind direction and speed profiles during two different flights: 09:01 UTC (a) and 09:31 UTC (b) on 15 July 2015. The blue profiles show multicopter data, dark grey circles represent EC station data, light grey squares lidar data and orange squares sodar data. Lidar and EC station data were averaged over the time the multicopter needed for the profile. Error bars show their standard deviation.

Both lidar and EC station data (both 1 min time resolution) are shown for the time around the vertical profiles of the multicopter (about 4 min). The sodar had a temporal resolution of 10 min, so only one value was available at each height. Wind direction and speed of the UAV data were in good agreement with the recordings of the different instruments. During the flights at 09:01 UTC and 09:31 UTC, wind direction was mainly from north to east with an increasing wind speed over time. For the first flight, spatial and temporal averages of multicopter, sodar and EC station were in agreement within 20–30° and a standard deviation of about ±20° for wind direction. Lidar data showed higher variability than other measurements but above 100 m data were in

the same range. Wind speed for all instruments was low with an average of about 1–1.5 m s^{-1} and a standard deviation of about ±0.6 m s^{-1}. For the second flight, the same was true for wind direction, but greater differences occurred for wind speed. While the multicopter and sodar recorded a mean speed of 2.6 m s^{-1} and 2.5 m s^{-1}, respectively, lidar and EC station had 1.7 m s^{-1} and 1.4 m s^{-1}, respectively. It should be noted that the instruments were not located at the same place (distance 100–570 m from multicopter, see Fig. 2.1) and that time resolution varied. Besides, during northeasterly winds, generation of turbulence is likely at the edge of the forest, which is to the east of the investigation area. Accordingly, differences can be explained by orographical influences, especially at heights up to 50 m.

5.4 Methane

During the first ScaleX campaign in 2015, methane measurements were done using the hexacopter F550. As mentioned before, an aluminum tube was installed at the hexacopter and an additional sampling line was attached to the hexacopter and the CRD spectrometer. By raising up the sampling line with the hexacopter, methane measurements were done at heights of 10, 25 and 50 m a.g.l. A hover time of 60 s at each level was included to get an averaged value. The pattern was repeated every 15 min and lasted for about 5 min.
For comparison of tower and multicopter results (Fig. 5.4), the subsequent measurements are displayed with orange points for tower data in 10 m and multicopter data with green ones also for 10 m. Short-term variations in methane concentration were detected by both techniques, even with the same extent (around 22:00 UTC). There was only one major deviation shortly past midnight when the multicopter measured a value of 2.45 ppm compared to 2.2 ppm at the tower. This may be due to the distance of approximately 5 m between tower and UAV and a time difference of around 30 s between those measurements. Overall, the two data sets were significantly correlated with a correlation coefficient of 0.96. Calculation of the RMSE led to ±0.063 ppm. Consequently, the measurements on the moving platform were as representative as those of the stationary tower installation.

For the campaign in 2016, an onboard methane analyzer was used, which was applied in cooperation with the Department of Civil and Environmental Engineering of the Princenton University, USA. The sensor was mounted below the lower center plate of the Pro X-3 Lite. Calibration was done several times during the campaign using the same reference gases as for the CRD

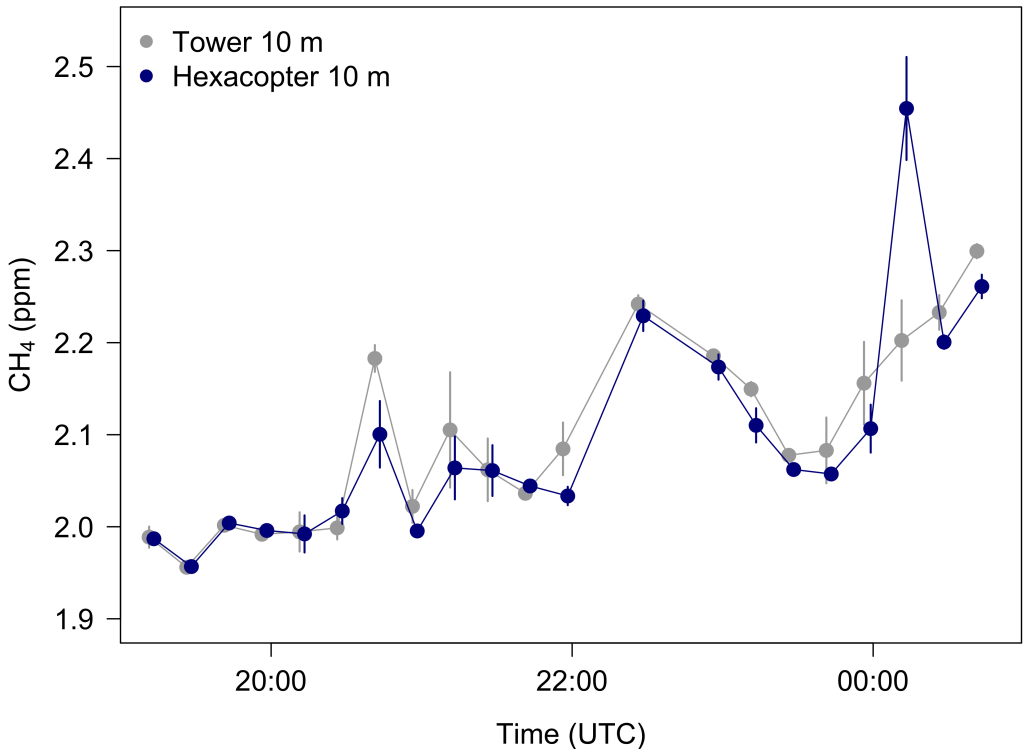

Fig. 5.4: Methane mixing ratio measured at the tower and with the multicopter in the night between 21 and 22 July 2015. Tower data were measured just before the 10 m data from the multicopter. Error bars show the standard deviation for each measurement averaged over 60 s. A standard deviation of 0.01 ppm or less cannot be shown because the size of the data point exceeds the error bar.

spectrometer analyzer, which was the same already used in 2015. Since the hexacopter-based methane measurements were done about 100 m away from methane measurements at the tower, comparison was possible and is shown in Fig. 5.5. The continuous time series of the Picarro analyzer shows an accumulation of methane close to the ground before 01:00 UTC, a decrease in concentration afterwards for about an hour and then again an increase until sunrise (03:26 UTC). The first four measurements of the UAV matched well with the concentration at the tower at both 1 m and 9 m. At 01:00 UTC, the gradient of 0.08 ppm between 1 and 9 m was captured by both instruments. However, the last two measurements with the UAV agreed at 9 m, but not at 1 m. The measurement at 03:00 UTC showed in fact a strong gradient, but the 1 m measurement was underestimated by the onboard sensor of the hexacopter resulting in a gradient half the magnitude of the one at the tower. Afterwards, the gradient was inverted and not as strong as before, but again an underestimation of the 1 m concentration was found. Uncertainties occurred

mainly because of a horizontal gradient, which is likely in case of a strong vertical gradient and in addition because both instruments measured the gradient with a time difference and not simultaneously. Calculation of the RMSE over the six flights led to ±0.05 ppm for 1 m and ±0.024 ppm for 9 m, respectively. From the tower, values before and after the flight were taken and the average was calculated to compare to the values measured with the hexacopter. The higher difference at the surface was probably caused by the higher variability of methane emissions. Overall, this agreement between tower and UAV was a reasonable result and especially for nighttime measurements sufficient because vertical gradients showed even the fivefold of concentration differences.

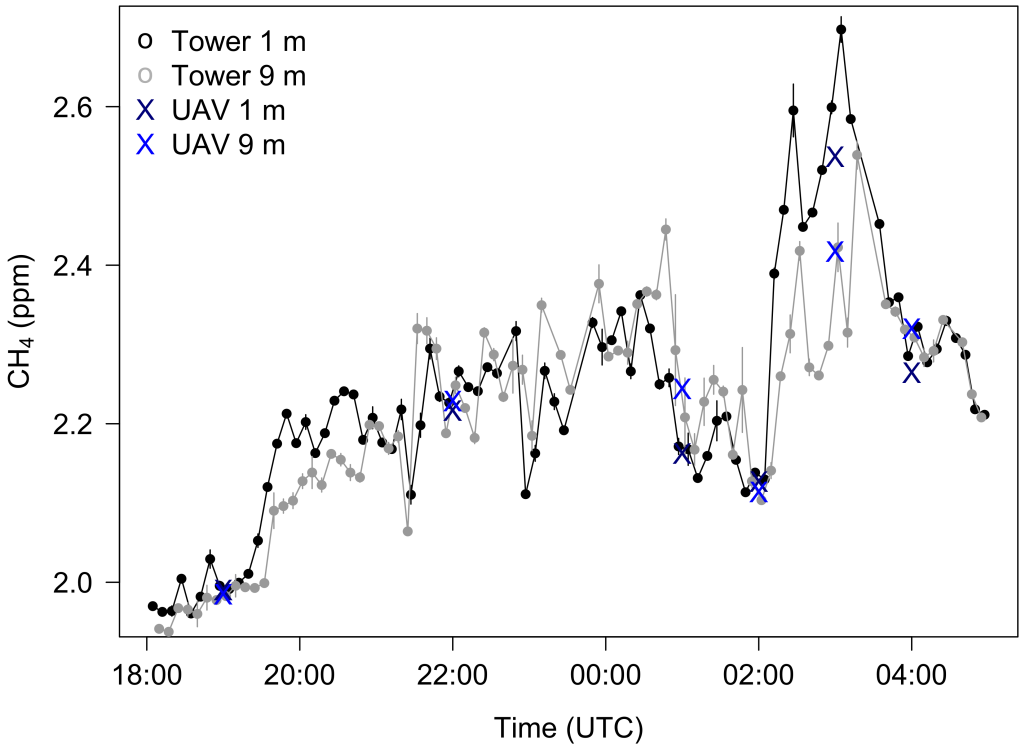

Fig. 5.5: Methane measurements taken from the tower and hexacopter between 19:00 and 04:00 UTC from 6 to 7 July 2016. Points indicate measurements at the tower and crosses mark the concentration measured with the hexacopter.

5.5 Combination of Measurements

Combining all the different necessary variables measured with the hexacopters, wind estimation and methane concentrations were the ones requiring the most attention.

The thermocouple and humidity sensor are small and lightweight and had no

influence on the other investigated variables. They were placed below a rotor to ensure a continuous flow around the sensors increasing their response time. Therefore, discontinuities were found while hovering because the measurements were rather representative for the volume around the multicopter than for a point.

The wind estimation carried out during hovering showed good agreement with the tower having a RMSE of 14.5° and 0.7 m s^{-1} for wind direction and speed, respectively. These values were determined using a moving average of 10 s. Applying a 20 s moving average, values of 12.5° and 0.6 m s^{-1} are similar to those obtained by Neumann and Bartholmai (2015) for hovering. The advantage of the approach of this study is that no wind tunnel experiments are necessary and that the experimental flights are easy to reproduce. Since the estimated errors were a result of only a 5 min flight, further experiments and comparisons would be necessary to confirm these values. The experimentally determined relationship between TAS and the tilt angle is only valid for this hexacopter configuration and up to a speed of 7 m s^{-1}.
Although the multicopter-based wind estimation was biased, measurements show similar results and the results of the other instruments showed differences too. Wind speed differed up to about 1 m s^{-1} and direction up to 50° above 50 m. Below this height, influences of topography, land use and horizontal distance as well as averaging time were more pronounced and differences larger. Horizontal distance to the multicopter was 370 m for lidar and 540 m for sodar, while they had averaging times of 1 min and 10 min, respectively, compared to the 10 s moving average of the multicopter. Lothon et al. (2014), for example, found similar biased differences dependent on horizontal distance and land use during the BLLAST campaign. In addition, low wind speeds (< 1 m s^{-1}) lead to higher variability in wind direction as seen for lidar data. This is because the wind is not well coupled to the meso-scale flow, which is often leading to variable wind directions (Anfossi et al., 2005; Mahrt, 2010). The same is true for multicopter-based wind direction at 10 m during the nighttime flights, which mainly occurred during wind speeds of less than 2 m s^{-1}. With regard to wind estimation from horizontal flights, this is especially important because flying with a specific speed requires a certain tilt angle. If this angle is significantly larger than the wind induced angle, determination of wind contribution to the angle could be more difficult depending on the accuracy of measuring the angle.
Hovering close to the ground led to limitations in the estimation of wind from the flight control sensors. The propeller's downwash caused motion of air be-

neath the multicopter. These were compensated by changing the tilt angle, but did not reflect actual wind conditions below a height of 5–6 m a.g.l. The effect was stronger during calm conditions because the jet of perturbed air did not advect away effectively. For the same reason, the data collected during descent were not used to estimate wind conditions because the multicopter moved through its own downwash.

With regard to methane measurements, both the tube-based approach and the onboard sensor showed a good performance during nighttime flights when comparing to the ground-based reference measurements. The presented results of the hexacopter-based approaches confirmed that extending measurements from towers have advantages, because of a more flexible measurement height and location.

The advantage of the tube-based approach was an averaged methane concentration at several levels with an accuracy better than 0.007 ppm and at the same time the one-minute variability was known. Although this was partly caused by the propellers stiring air, it was also partly due to the variable concentration transported to the measurement site. Palomaki et al. (2017) demonstrated in an experiment that wind speed at 30 cm above the multicopter is 0.5 m s^{-1} due to spinning rotors. According to Alvarado et al. (2017) this influence is negligible at a distance of 40–45 cm above the multicopter. In addition, no influence of the tube on the tilt angle could be detected while hovering at 10, 25 and 50 m. A negligible influence of payload was also found by Neumann and Bartholmai (2015). To each height, the multicopter had to lift more weight, but the autopilot compensated this with the spinning speed of the propellers, which was significantly higher on the side where the tube was mounted. Therefore, it is recommended to mount the tube in the center for a better flight performance. Besides, non-gusty wind conditions are favorable to reduce the wind load on the tube. Therefore, meteorological measurements were not affected by the methane measurements.

In contrast, the onboard sensor approach was more flexible, because it was not limited to the length of the tube and so vertical profiles beyond the nocturnal boundary layer were achievable (see chapter 7). Additionally, a continuous profile with data every 2 m resulted in detailed information about the actual distribution of methane and meteorological measurements. So, specific layers could be identified within the measurement height and it became obvious that the methane concentration did not decrease linearly with height but that the distribution was more complex. However, there was only one profile each hour and no variability within a shorter time. But this could be overcome with more

flights. Another limitation was that the onboard sensor was not as reliable as the Picarro analyzer. Almost half of the data did not pass the quality check criteria in the post-processing caused due to noise on the signal. But it has to be pointed out that the onboard methane sensor is still a prototype and more testing is necessary to improve its long-term stability (Golston et al., 2017). Until now, it is not routinely used as the Picarro analyzer.
Altogether, the latter was preferable because the NBL height and the flux could be determined and therefore the information value was higher.

6 UAV-based Estimation of Evapotranspiration based on the Surface Energy Balance

With regard to the second objective of this thesis, estimation of evapotranspiration rates over a typical grassland site in the foothills of the Bavarian Alps in southern Germany is focused. To this end, interrelations between hydrometeorological variables and surface characteristics were investigated. Therefore, spatial and temporal information about meteorological conditions and radiation as well as surface parameters like vegetation cover and surface roughness are necessary.

In a first step statistical methods as spatial correlation and principle component analysis were applied to get information about the relationship between surface and hydrometeorological variables and their importance in the energy balance. In a second step, spatial and temporal evapotranspiration rates and thus the turbulent latent heat fluxes were estimated by calculating the residual term of the energy balance when net radiation, ground heat and sensible heat fluxes are given.

6.1 Flight Setup and Data

For the hexacopter-based estimation of evapotranspiration, horizontal flights were performed over the grassland site in DE-Fen covering an area of 350 m x 150 m, while three long straight lines with a distance of 50 m were flown in east–west direction. In total, 20 flights were available for analysis at 5, 10 and 15 m a.g.l. Those data were interpolated to a regular grid with 135 x 3 grid cells spanning the extent of the flight tracks by using the Inverse Distance Weighting method (see chapter 4.1). In Fig. 6.1, both the flight track and the interpolated grid are shown.
All necessary variables based on multicopter measurements for further analyses were interpolated, which were air, potential and land surface tempera-

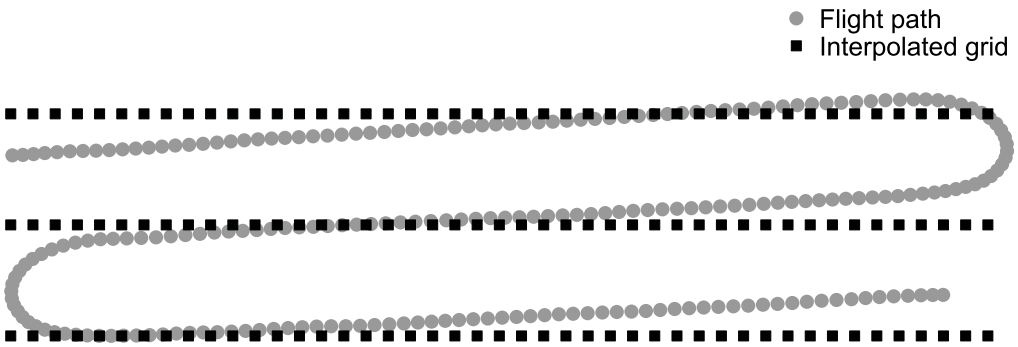

Fig. 6.1: Flight track of horizontal pattern (grey points) and interpolated grid by using the Inverse Distance Weighting method (black squares). The flight track was aligned to the topography and thus parallel to the street and not in east–west direction as the interpolated grid.

ture, relative and specific humidity, wind speed and direction and air pressure. Additional variables as soil temperature and moisture from the SoilNet measurements and NDVI (Normalized Difference Vegetation Index) from satellite imagery were interpolated to the same grid. Since EC station and SoilNet data had a time resolution of 30 min and 15 min, data points with the least time difference to the flights were used.

6.2 Correlation Between Flights

As a first overview about differences among the variables, the Pearson's correlation coefficient was calculated to get information about spatial patterns. For each variable, all flights were correlated with each other and the correlation indices were shown in a correlation matrix.

During the course of day, hydrometeorological variables showed partly high spatial differences over the grassland site in the foothills of the Bavarian Alps. This was not only caused by varying sun radiation, but also changing land cover situations.

Correlation of investigated variables between all the flights revealed a significant pattern variability (Fig. 6.2). Each flight was correlated with all other flights and coded with two numbers separated by "_". The first number stands for the day in July and the second for the flying height in meters. Thus, flight "4_10" were done on 4 July at 10 m a.g.l., "5_5" on 5 July at 5 m, etc. A list of flights was provided in Tab. 6.1. Looking at the meteorological variables air temperature, relative humidity and wind, both positive (in blue) and negative

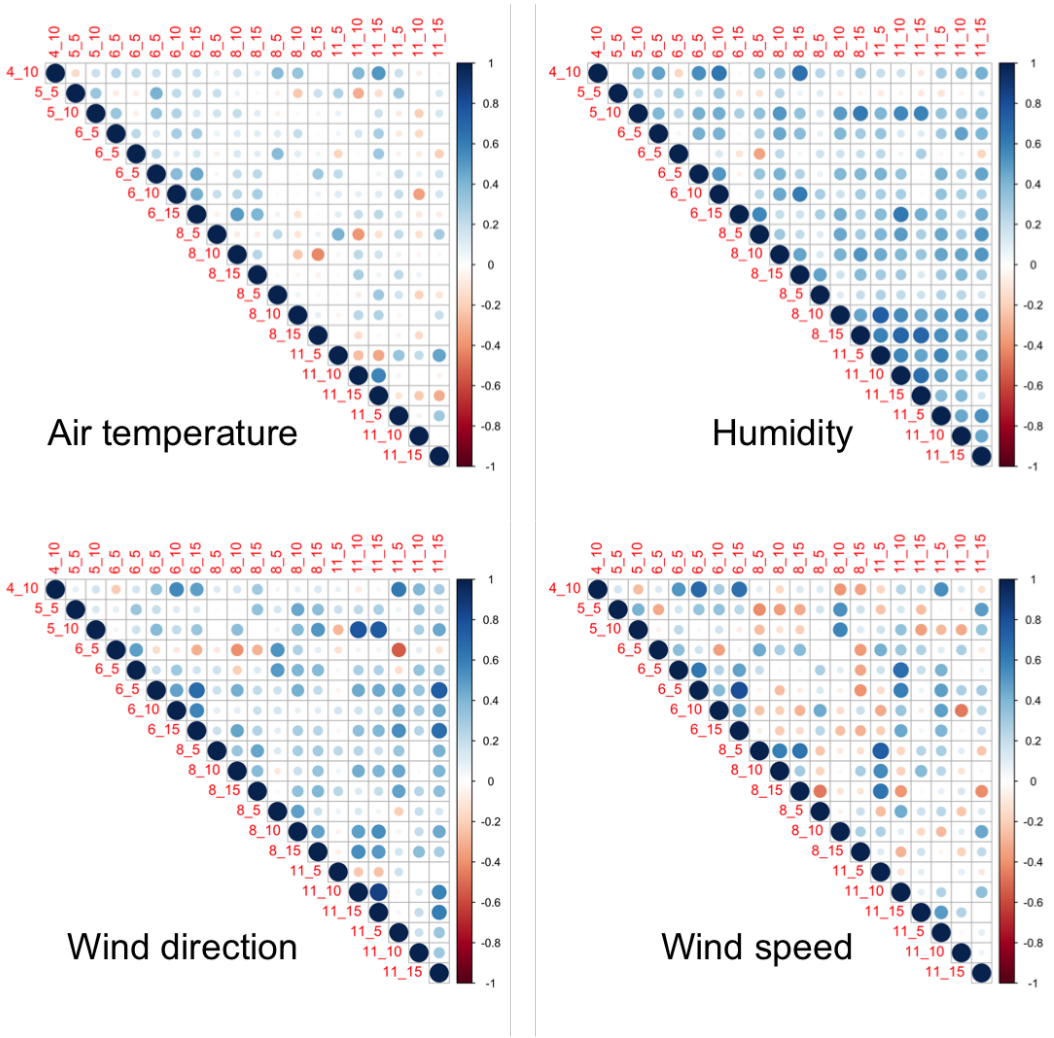

Fig. 6.2: Correlation matrices of meteorological variables between all horizontal flights above the grassland site in DE-Fen. Each flight was coded with the day in July (4, 5, 6, 8, 11) as the first number and the flying height (5, 10, 15 in m a.g.l.) as the second number. Hour of day was neglected, but the order of flights is shown chronologically. Blue points represent a high positive correlation while red points stand for high negative correlation. The diameter of the points indicated the magnitude of correlation with a larger diameter for a higher correlation.

(in red) correlations occurred. But altogether the correlation was not so high between the flights with values mainly between -0.5 and 0.5. The assumption was that consecutive flights correlated higher compared to flights with a greater time difference, when stationarity could be assumed. This can be seen, for example, for humidity for flights on the 11 July 2016. Correlation of air temperature was the lowest comparing with other variables. This was likely caused by fluctuations through turbulent processes. For wind direction it has to be mentioned that data were aggregated to 30° classes and it was accounted for

Tab. 6.1: Overview about the horizontal flights above the grassland site in DE-Fen. Time is given in UTC and height in m a.g.l.

Flight	Day	Time	Height	Flight	Day	Time	Height
1	4 July	13:20	10 m	11	8 July	9:10	15 m
2	5 July	13:35	5 m	12	8 July	10:50	5 m
3	5 July	13:45	10 m	13	8 July	11:00	10 m
4	6 July	13:20	5 m	14	8 July	11:10	15 m
5	6 July	14:35	5 m	15	11 July	7:35	5 m
6	6 July	16:30	5 m	16	11 July	8:45	10 m
7	6 July	16:40	10 m	17	11 July	8:55	15 m
8	6 July	16:50	15 m	18	11 July	11:00	5 m
9	8 July	8:50	5 m	19	11 July	11:10	10 m
10	8 July	9:00	10 m	20	11 July	11:50	15 m

the jump between 360° and 0°. Without this correction, the correlation would be more negative although the predominating wind direction was northwest to northeast.

Looking at land surface temperature and soil temperature and soil moisture correlation was significantly higher than for meteorological variables between the flights (Fig. 6.3). The overall correlation was predominantly in the range of 0.6 to 0.7 and more than 0.8 when considering flights during the same day. From 4 to 6 July, LST correlated positively and flights on the 8 July correlated with those on the 11 July. Those also correlated negatively with flights on 4 to 6 July, but only low correlation with 8 July. This change in LST might be caused by changing vegetation height due to mowed grass. Since the grass was used for pasture not the whole site was mowed at the same time. In addition, at a small part in the southeast of the grassland, the mowed grass was left on the ground for drying to hay.
For soil temperature and moisture, the correlation looked similar and all days correlated highly except on 11 July. On that day correlation was also very high, but not compared to the other days. An explanation could be that mowing the grass had an influence to the pattern of soil variables, too. Another explanation could be that no rain occurred during the whole measurement period and therefore, the soil dried further from day to day as seen from the SoilNet data. While at the beginning a pattern with wetter spots could be identified this was less pronounced on 11 July. In addition, the soil moisture pattern itself changed from 8 to 11 July, which was also the case for soil temperature. The course of the day was more pronounced for soil temperature than for moisture.

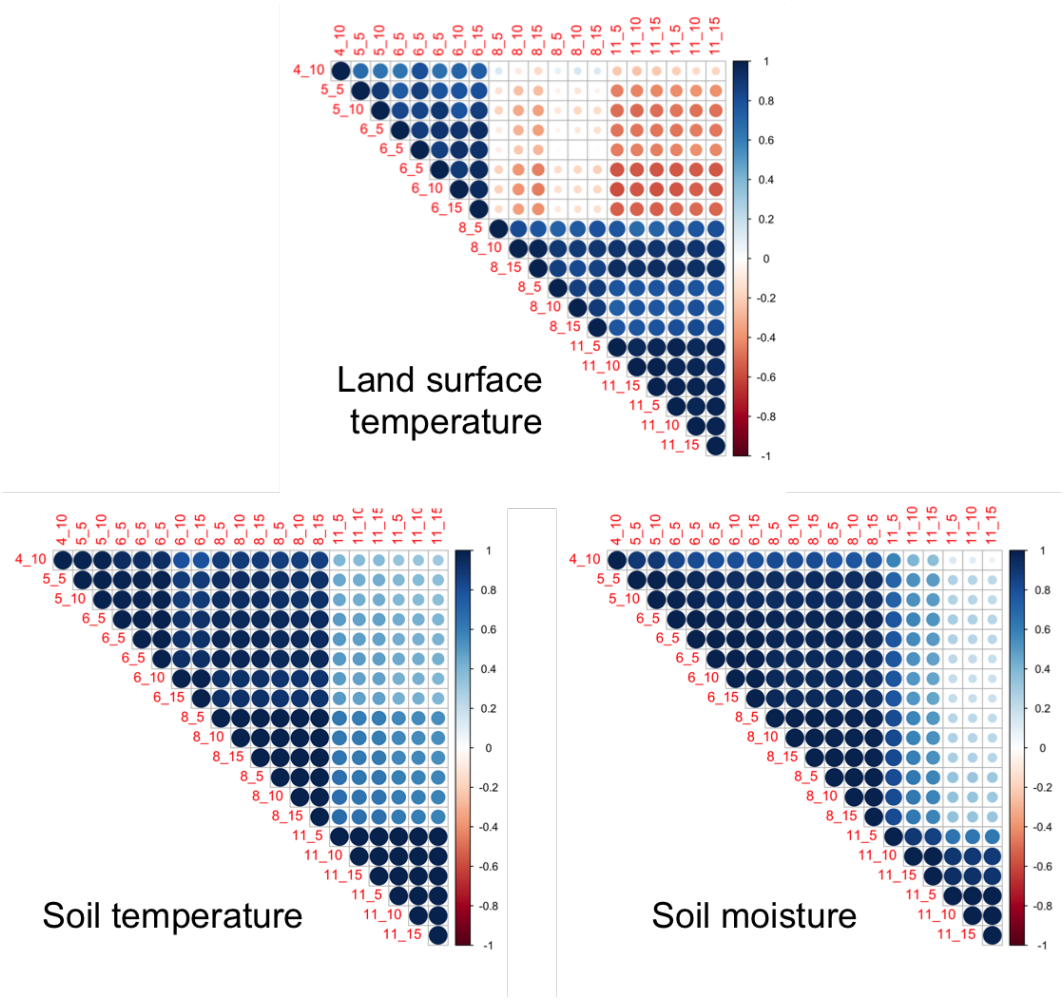

Fig. 6.3: Correlation matrices of surface and soil variables between all horizontal flights above the grassland site in DE-Fen. Representation is the same as Fig. 6.2.

6.3 Variability of Hydrometeorological Variables

In addition to the correlation of investigated variables between the flights, the horizontal and temporal variability of air, surface and soil temperature was investigated in more detail (Fig. 6.4). Air temperature was calculated to potential temperature relative to the pressure at the ground to compare the three different flying heights. But since there was only a difference of 10 m, the change was within the temperature's accuracy. Flights were plotted in chronological order and the variability of each flight is shown with a boxplot. More information about the boxplot is given in the figure's caption. The horizontal variability was highest for LST followed by T_{soil} and then T_{pot} as it was assumed. LST variability was on the one hand dependent on sun radiation and on the other hand on vegetation cover and height, respectively. Soil temperature was affected by the amount of energy going into the ground and the soil

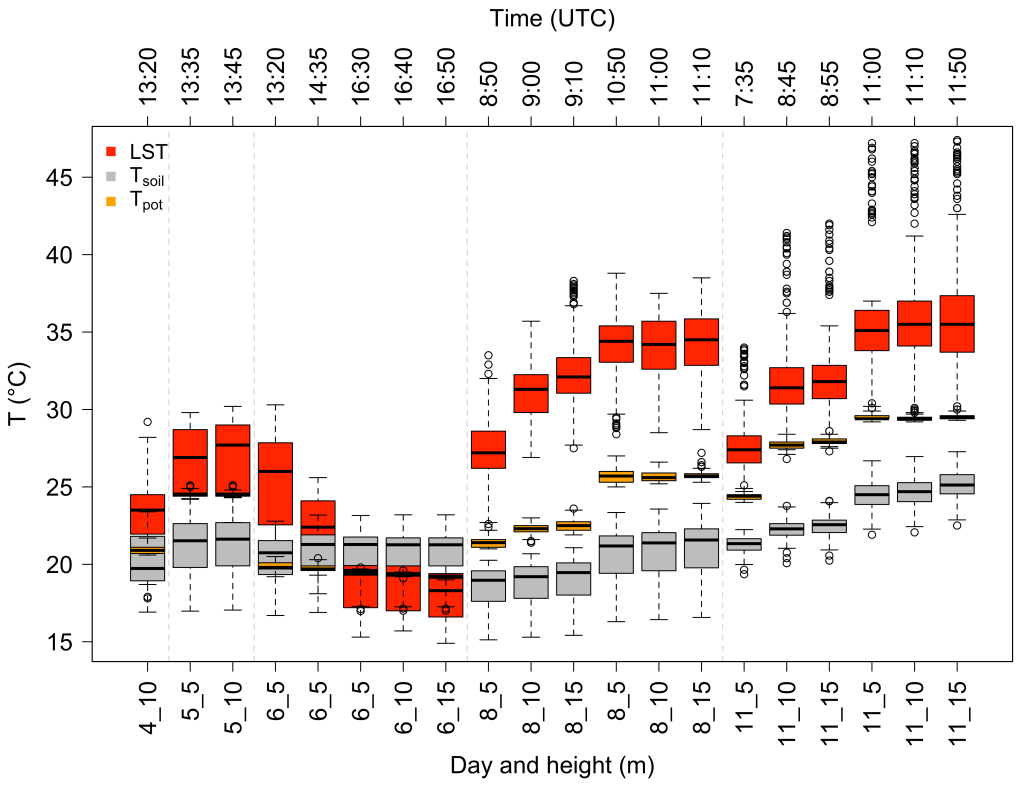

Fig. 6.4: Horizontal and temporal variability of surface, soil and potential temperature represented as boxplots for each flight. Potential temperature's unit was converted from K to °C for easier comparison. At the lower x-axis the flights were coded with their day of July and flying height and at the upper x-axis the measurement time in UTC. The colored boxes contain 50 % of the data and represent the interquartile range with the median as a black line. The dashed lines show maximum and minimum values in case those values are within the 1.5 interquartile range. Values outside this range (outliers) are represented with circles. The light grey dashed lines separate the days.

moisture. Therefore, variability decreased with drying of the soil as seen in the difference between 11 July and the other days. However, temperature in the air showed the least variability because turbulent mixing plays an important role. The air close to the ground was heated from energy transport through sensible and latent heat fluxes and thus through turbulent exchange. This transport of energy is less effective than radiation (from the sun) or conduction (in the soil). Additionally, air is moving all the time leading to mixing and therefore lower variability. This would be different in case of varying land covers.

Considering the variability of these temperatures, standard deviations were calculated to investigate their variability in more detail (Fig. 6.5). Values ranged from 0.1 K for potential temperature in the evening to almost 5 °C for LST at noon. In order to also show the deviations of T_{pot}, a secondary y-axis was plotted with values one order of magnitude smaller. The results showed that

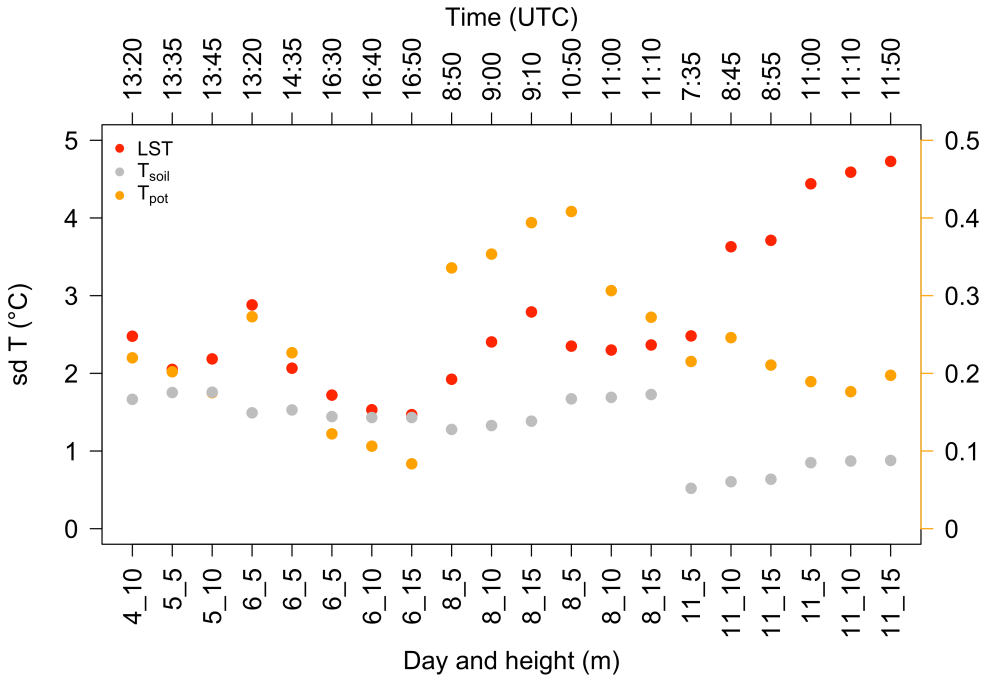

Fig. 6.5: Standard deviation (sd) of surface (LST), soil (T_{soil}) and potential (T_{pot}) temperature from horizontal flights during the measurement period. Flights were ordered chronologically as in Fig. 6.4. Since the standard deviation of T_{pot} was one magnitude smaller, the values are shown at the secondary y-axis in orange.

spatial variability changed in magnitude during the measurement period. This was not only caused by atmospheric conditions, but also vegetation height and soil moisture. While the soil temperature's standard deviation was relatively constant from 4 to 8 July compared to other temperatures, it decreased on 11 July when soil moisture had decreased too. This was the day when LST showed the highest horizontal variability with almost 5 °C. This was likely caused by the dried grass lying on the ground. The highest potential temperature variability occurred on 8 July when solar radiation reached its maximum. For successive flights, variability only changed within measurement accuracy for LST and T_{pot}, while constant values for T_{soil} can be traced back to the time resolution of 15 min. Within this time, two horizontal flights were done with the multicopter.

As already mentioned, the horizontal pattern of LST changed during the measurement period, while in particular the southeast corner of the area stood out, where high LST was observed on 11 July (Fig. 6.6). Soil moisture or more accurate the volumetric water content decreased during the measurements, especially over the last few days. Taking one flight at the beginning of the period (6 July, 16:50 UTC) soil moisture was predominantly between 40 and 50 %.

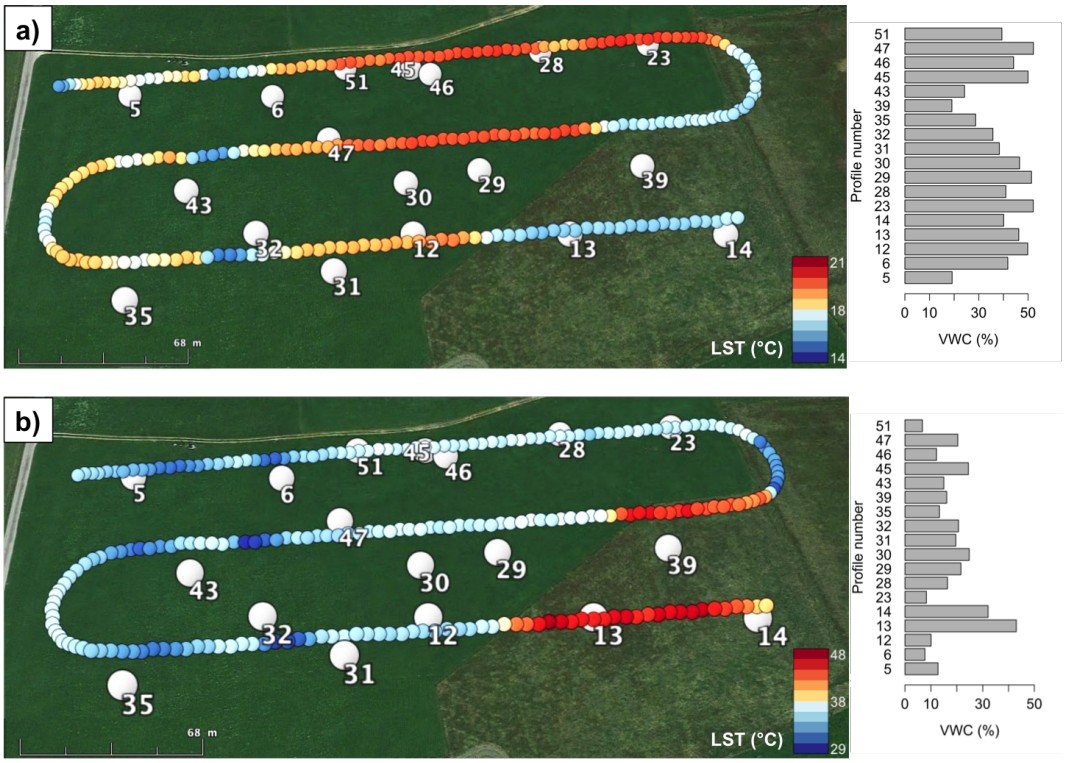

Fig. 6.6: Land surface temperature (LST) along the horizontal flight track over the soil moisture network. a) Flight at 15 m a.g.l. on 6 July at 16:50 UTC and b) flight at 10 m a.g.l. on 11 July at 11:10 UTC. Volumetric water content (VWC) is shown for the same time with sensor locations close to the flight track. Legend values for LST are not the same because the horizontal pattern was focused and not the magnitude of LST, which was mainly influenced by sun radiation.

Lower values occurred in the west and southeast of the site. LST was lower in the southeast, but cooler areas also occurred in the west towards the street. This was likely due to differences in vegetation height, which was in agreement with visual observations at the site. Comparing those results with data from the end of the measurement period (11 July, 11:10 UTC), LST was higher due to higher incoming radiation and the horizontal LST pattern reversed. Soil moisture decreased to around 20 %, which was expected due to predominating fair weather without rain. Interestingly, soil moisture remained higher in the southeast (profile 13 and 14), where the dried cut grass was lying. An explanation could be that evapotranspiration was reduced due to the fact that the ground was covered with dead vegetation and served as a barrier. But on the other hand, the proximity to the small stream could have an influence on soil moisture, too.

6.4 Importance of Hydrometeorological Variables

After analyzing the variability of investigated variables in space and time, the most important variables acting in the surface energy balance were investigated. For this, the interpolated data of measured variables were used as input variables for the principle component analysis. On the one hand, correlation and PCA were applied to get an overview about relationships within flights and variables and on the other hand to investigate interactions in the energy balance.

So far, the horizontal and temporal variability of hydrometeorological variables was shown and how drivers as sun radiation or vegetation height influenced those variables. Using the principle component analysis, the importance of these variables can be identified with regard to the surface energy balance (Fig. 6.7a). Results showed that most important variables were air temperature and humidity followed by wind and LST. Soil variables explained the lowest variability of the data set and thus had less contribution. The first two principle components explained 69.5 % of the total variability, which were plotted as x- and y-axis, respectively. The length of the vectors of each variable represents the contribution to the variability of the data set. This contribution to the corresponding component was calculated by using cosine angles between x-/ y-axis and the vectors. The smaller the angle, the higher the correlation becoming uncorrelated for orthogonal vectors. Correlation between the variables can be calculated the same way.

In addition, another PCA was done including the energy balance components net radiation, sensible and latent heat flux as well as the Bowen ratio, air pressure and long-term incoming radiation (Fig. 6.7b). Ground heat flux and long-term outgoing radiation were not included because of redundant information to the radiation and land surface temperature, respectively. Short-wave terms were neglected because no horizontal variability was available, only point information from the EC station. The explained variability based on the first two components was reduced to 61.1 % and the overall contribution of each variable decreased. Vectors of variables from the first PCA were similar, while the additional variables contributed predominantly to the first component. Interestingly, the Bowen ratio did not contribute significantly although it is just the ratio between the sensible and latent heat flux, but was the most important variable for the fourth component. LE and R_{net} contributed to the first and

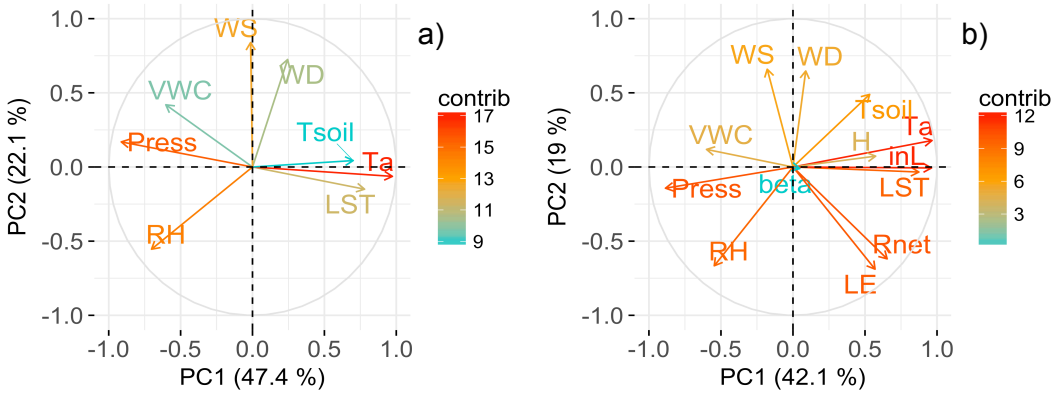

Fig. 6.7: Principle component analyses of a) hydrometeorological variables and b) hydrometeorological variables and all energy balance components. Only the first two principle components are shown, the first on the x-axis and the second on the y-axis. Included variables were air temperature (Ta), relative humidity (RH), wind speed (WS) and direction (WD), land surface temperature (LST), soil moisture (VWC) and temperature ($Tsoil$), air pressure ($Press$), net radiation ($Rnet$), sensible (H) and latent (LE) heat flux, long-wave incoming radiation (inL) and Bowen ratio (beta). The color-coded legend represent the contribution of each variable to the variability of the data set.

second component, while pressure, sensible heat flux, and long-wave radiation mainly added to the first component.

6.5 Estimation of Turbulent Heat Fluxes

Finally, in the last step the energy balance components were estimated by using both multicopter data from horizontal flights as well as EC station data (Fig. 6.8).

Spatial energy balance components based on multicopter flights were averaged over the covered flight area to compare it to EC data. The approach of Kustas et al. (1989) for the resistance to heat transfer kB^{-1} led to the best agreement of sensible heat flux estimations with EC station data, in which the added resistance to heat transfer was not constant as suggested by Bastiaanssen et al. (1998). The ground heat flux is shown estimated as a fixed ratio of net radiation, which resulted in more accurate values than based on NDVI dependent calculations. EC station derived energy balance measurements were corrected for energy balance closure applying the Bowen ratio method, in which the Bowen ratio was kept constant. Since two ground heat flux measurements were available around the EC station, those values were averaged when compared

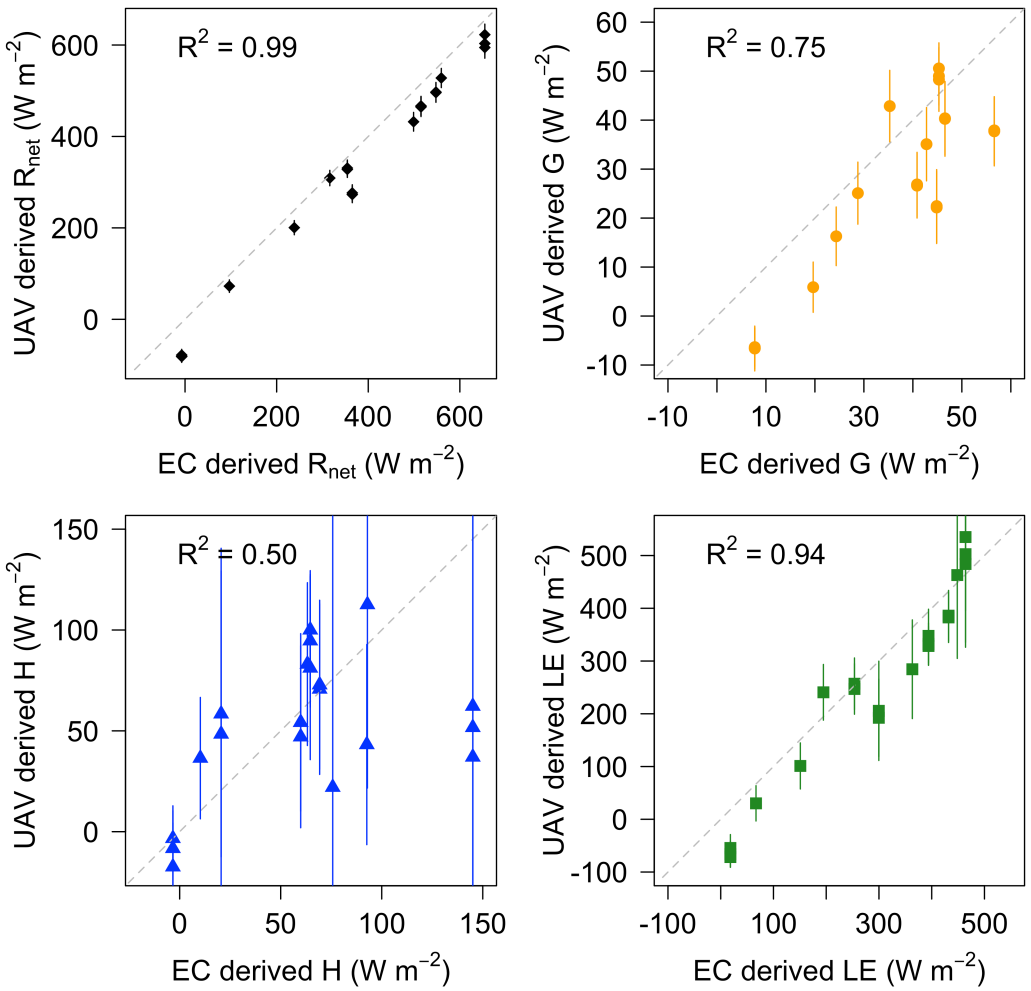

Fig. 6.8: Surface energy balance components net radiation (R_{net}) in black, ground heat (G) in orange, sensible heat (H) in blue and latent heat (LE) flux in green derived from EC station and multicopter data. Error bars give the range of uncertainty from error propagation results. The grey dashed lines represent the 1:1 ratio between the components.

to the UAV-derived flux.

The best performance showed the estimation of the net radiation with a R^2 of 0.99 and a RMSE of 55.2 Wm^{-2}. Altogether, the UAV-derived values were underestimated with small errors based on the error propagation, in which accuracies of albedo, LST, air temperature and humidity were included. The ground heat flux was predominantly underestimated too, while comparison led to a R^2 of 0.75 and a RMSE of 13.4 Wm^{-2}. But since the ground heat flux represents a fixed percentage of the net radiation, which was underestimated with multicopter data, it was not surprising that G was underestimated as well. Its error estimation included uncertainty of the percentage as well as of R_{net}. Considering the sensible heat flux, results looked differently. The R^2 was

Tab. 6.2: Statistical parameters of net radiation (R_{net}), ground heat (G), sensible heat (H) and latent heat (LE) flux derived from UAV data. Parameters are: average over all flights (average), mean error from error propagation (mean error), coefficient of determination (R^2), root-mean-square error (RMSE) and mean absolute error (MAE). All parameters have the unit Wm^{-2}, except R^2, which is dimensionless.

	R_{net}	G	H	LE
Average	336	27.3	52.3	256.4
Mean error	18.5	6.3	66.3	70.1
R^2	0.99	0.75	0.5	0.94
RMSE	55.2	13.4	44.2	61.2
MAE	50.6	11.9	32.2	54.1

with 0.5 the lowest value and fluxes were both over- and underestimated. Error propagation including LST, T_a, wind speed and vegetation height, which led to higher values compared to R_{net} and G and the RMSE was 44.2 Wm^{-2}. Estimation of the latent heat flux showed high agreement with R^2 of 0.94 and a RMSE of 61.2 Wm^{-2}. Most of the values were again underestimated but some overestimation occurred too. This was unexpected, because LE was calculated as the residual from the other energy balance components and the sensible heat flux did not match with EC-derived sensible heat flux all the time. The predominating underestimation was explainable due to the overall lower availability of energy. Error propagation included uncertainties of all other components R_{net}, G and H. An overview about statistical parameters of the UAV-derived energy balance components was provided in Tab. 6.2.

Looking at the energy balance components derived from each flight, their temporal variability and uncertainty can been seen (Fig. 6.9). While estimated uncertainties of net radiation and ground heat flux were similar between the flights, the uncertainties of the sensible heat flux varied depending on meteorological conditions. Thus, the same was true for the latent heat flux because its error included the one from the sensible heat flux. However, the relative LE error was smaller because the flux was higher. Four flights could be identified with relative high uncertainties; the first three on 8 July and the first on 11 July. The last three on 11 July had also higher values, but were below 100 Wm^{-2}. Those high uncertainties occurred when horizontal variability of H was lower compared to other flights. In addition, input variables showed a higher mean temperature gradient between surface and air and at the same time a lower mean wind speed. This indicated that sun radiation intensive weather conditions and calm wind conditions cannot be represented as good as less sunny

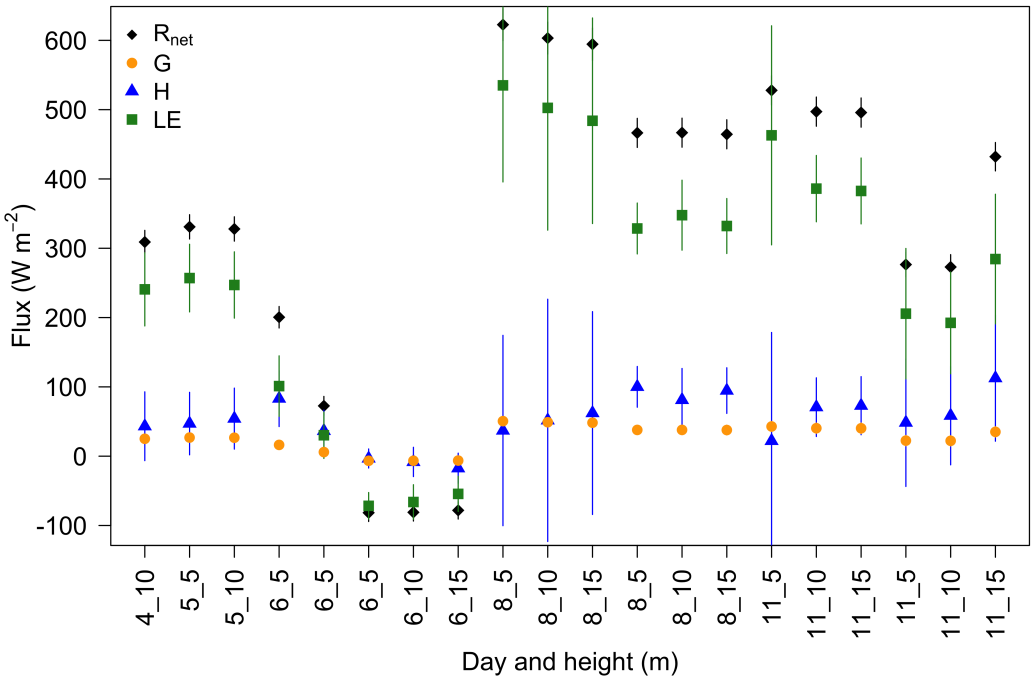

Fig. 6.9: UAV-derived surface energy balance components net radiation (R_{net}) in black, ground heat (G) in orange, sensible heat (H) in blue and latent heat (LE) flux in green in chronological order. Error bars give the range of uncertainty from error propagation results. Values below 10 Wm^{-2} cannot be shown because the size of the data point exceeds the error bar.

and less calm conditions. But since the data availability was limited, this was a qualitative result.

Instantaneous latent heat fluxes were converted to daily evapotranspiration rates according to the equations in chapter 4.2. This resulted in values of 2 mm on 6 July, 4 mm on 4 and 11 July and 5 mm on 5 and 8 July. Negative latent heat fluxes were excluded since the fluxes were directed to the surface. Taking into consideration the precipitation amount of about 1100 mm at Fendt per year (Soltani et al., 2017), which corresponds to about 3 mm d^{-1}, the ET rate exceeded the precipitation amount and led to a drying of the soil. But it has to be considered that according to the climate diagram of Wielenbach (Fig. 2.2), about half of the yearly precipitation occurs between May and September leading, on average, to a higher amount than 3 mm d^{-1} in July.

6.6 Summary and Discussion

The presented results showed that hexacopter-based measurements are a good and flexible alternative to other instrumentation for the estimation of eva-

potranspiration. The investigated grassland site was assumed to be mainly homogeneous but variability of the surface properties and meteorological conditions above the surface were found. Those changed predominantly depending on weather conditions and day of time, but also with grassland management as mowing grass as animal feed. Therefore, it was important to include as many changes as possible for analyzing the variability and energy balance components. Having such an equipped multicopter as presented here, those kind of measurements and estimations is also possible above other land use types.

The flight pattern used for investigations was suitable for the purpose of measurements and the covered area was large enough to identify significant differences both in the air and on the surface. Although interpolation of values was necessary for comparison of flights, mean and standard deviation were the same or at least within the sensor's accuracy. So, averaging and thus smoothing of the data for each grid point did not decrease the informative value.
Cuxart et al. (2016) were also measuring above a grassland site using a multicopter and found similar values for standard deviations of LST, but higher values for T_a. According to Mahrt (2000), those heterogeneities can be traced back to surface roughness and are only visible below the "blending height". Above this height, the influence of surface heterogeneities vanishes or drops below a threshold. The height of the roughness layer is dependent on the surface roughness leading to a higher altitude for rougher surfaces, but weather conditions are important, too. In order to identify the blending height above the grassland site, measurements at higher altitudes would have been necessary. According to the standard deviation of measured meteorological variables, there was no difference between 5, 10 and 15 m a.g.l. Taking the flight track back to the starting point into account, which was at the safety altitude of 25 m a.g.l., standard deviation of both air temperature and humidity decreased significantly. Therefore, this indicated that 25 m had to be close to the blending height. According to Foken (2008), the blending height is in the range of 30 to 100 m.

Uncertainty of energy balance components was based on the one hand on multicopter-based measurements of hydrometeorological variables and on the other hand on variables, which were not measured spatially. LST and wind speed seemed to be the most critical hydrometeorological variables because they had a high impact on calculating the energy balance and especially the sensible heat flux. At the same time, their accuracy was lower compared to, for example, permanently installed instruments at the EC station, which led to a higher error of the fluxes. The parameter r_{ah} was highly dependent on wind

speed and decreased as wind speed increased independent on the temperature gradient between surface and air (Hatfield et al., 1983). Both air temperature and wind speed showed a high impact on the PCA calculation, too.
The not spatially measured variables included vegetation height, albedo and short-wave incoming and outgoing radiation. Vegetation height is likely to be the most important one because it affects the other two; albedo directly and radiation through albedo indirectly. Additionally, vegetation height highly differed over the period of measurement days, which influenced the surface roughness. Especially for H estimations, surface roughness plays a significant role (Jackson, 1985).
Although, the difference between T_{aero} and LST was taken into account by including kB^{-1} into the sensible heat flux estimation, a two-source energy balance model leads to more accurate results, because the temperature of soil and vegetation is calculated separately and then weighted according to vegetation coverage (Li et al., 2009). The difference between T_{aero} and LST can reach 2 °C for homogeneous vegetation and 10 °C for partially vegetated areas (Kustas and Norman, 1996).
On the other hand, Brenner et al. (2017) investigated the difference between one-source and two-source energy balance models and found out that the agreement with EC station fluxes was better with the two-source model, but the improvement was low compared to the effort of additional measurements.

Comparison of multicopter-based energy balance estimation to EC station data showed an overall promising agreement, although the estimation of the sensible heat flux had high errors and R^2 was the lowest with 0.5. Excluding the four flights with highest errors (see Fig. 6.9), statistical parameters of sensible heat flux improved. RMSE decreased by almost 50 % to 23.7 Wm^{-2}, MAE decreased to 19.1 Wm^{-2} and R^2 increased to 0.6 instead of 0.5. While the RMSE was about 80 % of the averaged H, this value dropped to about 40 % after excluding the four flights.
Other UAV-based studies, in which the residual energy balance method was applied showed similar results when comparing estimated fluxes to EC station derived fluxes (Hoffmann et al., 2016; Ortega-Farías et al., 2016; Brenner et al., 2017, 2018). Net radiation showed the best agreement followed by the latent heat flux, while ground and sensible heat flux were more difficult to determine. This was also the case when using a two-source model.
But the lower agreement of sensible heat fluxes were not only caused by the multicopter data, but also by the EC station data. With an energy balance closure of 68 %, the remaining surplus of energy was about one third of the

available energy. This value was also found by Soltani et al. (2017) for the same location with data spanning over two years. According to Finnigan et al. (2003), a closure of 70 % is typical, especially for measurements in complex topography, although the footprint area is homogeneous. Another influence on the comparison was the differing spatial extent of the footprint and flying area. Multicopter flights were done over the soil moisture and temperature network, which is part of the EC station's footprint area, but not during predominating wind directions from north. In fact, flights directly over the footprint area would have influenced the EC measurement itself.

If not all variables are measured for calculating the energy balance components, some assumptions may be necessary. For example the short-wave solar radiation is determinable by using information about the solar constant, the solar inclination angle, the geographic location, the time of the year, the elevation and atmospheric transmissivity (Li et al., 2009). Having more detailed information about the NDVI and not only one NDVI map before the measurements, ground heat flux estimates profit from vegetation to bare soil ratio. This is also important for sensible heat flux estimations applying a two-source energy balance model. The leaf area index (LAI), which describes the density of vegetation per unit area, gives additional information for those estimates (e.g., Kustas et al., 2012). Using satellite-based data with a horizontal grid resolution of 30 m (e.g. Landsat), both NDVI and LAI as well as albedo are determinable (Yang et al., 2017), but operation of UAVs with cameras in the visible and near-infrared spectra provide a good alternative.

7 UAV-based Agricultural Methane Emission Estimates and Influences of Meteorological Conditions

The third and last objective of this thesis addresses the influences of meteorological conditions, such as air temperature, humidity and wind, and transport processes at local to regional scales on the methane concentration in a stable nocturnal boundary layer. To this end, methane emissions are estimated based on hexacopter measurements and the advantages to other measurements are shown.

First, the two different approaches measuring methane concentrations based on multicopter platforms are presented. Afterwards, vertical profiles of meteorological variables and methane concentrations are shown. From this, nocturnal stability and methane fluxes were calculated. In the last step, information about the footprint and transport processes is given.

7.1 The Two Used Approaches

In order to investigate the interactions between meteorological variables, transport processes and methane concentration on local to regional scales, two different approaches were tested.
During the ScaleX campaign in 2015, a tube was connecting the hexacopter F550 and methane analyzer (Picarro), focusing the feasibility of hexacopter-based vertical gradients of methane concentration in a stable nocturnal boundary layer. Those investigations were frequently done by measuring every 15 min for almost seven hours using hover flights at three different levels (10, 25, 50 m) with a hover time of 60 s.
For the ScaleX campaign in 2016, an onboard open-path methane sensor (see chapter 3.3.3) was used to investigate the vertical methane distribution through

the whole nocturnal boundary layer up to 150 m. At the same time, meteorological variables were measured, too. Using the onboard sensor in 2016, measurements were done every full hour starting before sunset until after sunrise the following day. Besides, data of 2016 were applied for sensible heat and methane flux estimation leading to a vertically integrated and temporally averaged value. The nocturnal methane flux was estimated on the one hand by using multicopter data and on the other hand based on ground-based instrumentation at the 9 m tower. To this end, the nocturnal boundary layer height had to be determined first by using potential temperature for the multicopter approach and a ceilometer for the ground-based one. Since no vertical profile throughout the NBL was available using the ground-based data, the average between ground and above the NBL (background concentration) was taken assuming linear decrease with height within the NBL. Sensible heat flux based on multicopter data was compared to EC data at the tower, which had an output of half hourly surface fluxes. But using the EC method, nighttime fluxes were more difficult to determine than during daytime and therefore, data for comparison were limited.

7.2 Vertical Gradients and Meteorological Conditions

During the ScaleX campaigns in 2015 and 2016, two different hexacopter-based approaches were tested to get information about the vertical distribution of methane concentrations depending on meteorological conditions. The results are shown separately for the campaigns in the following.

ScaleX 2015 Considering the vertical methane profiles up to 50 m a.g.l., gradients were detectable during stable atmospheric conditions after sunset (Fig. 7.1). Data are shown for six flights with one-hour intervals beginning at 19:32 UTC and ending at 00:32 UTC. According to the potential temperature profiles, a stable stratification of the atmosphere developed after sunset indicated by increasing potential temperature with height. Its difference reached 5–6 K between ground and 50 m. Thus, this overall stable stratification led to the reduced vertical mixing and methane sources in the surrounding caused a concentration rise of 0.3 ppm after sunset within six hours. The mean background concentration measured during this campaign was 1.9 ppm. The concentration increased at each height with time, while accumulation started from the ground. Vertical gradients were already visible right after sunset, were in-

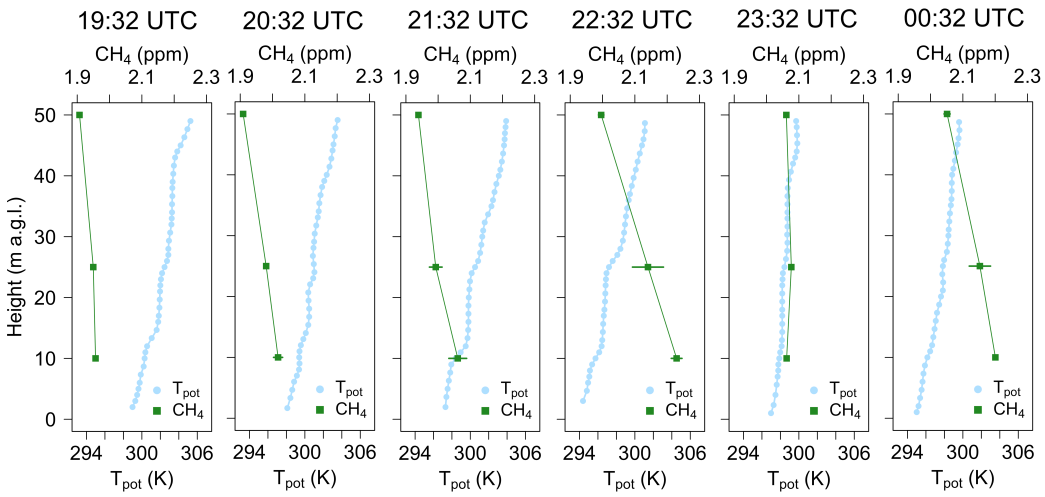

Fig. 7.1: Vertical potential temperature (T_{pot}) profiles in blue and methane concentrations in green during six hours from 19:32 UTC (left) to 00:32 UTC (right) in the night 21 to 22 July 2015. T_{pot} was averaged at hovering levels and smoothed with a moving average (3 s). Error bars of methane concentration show the standard deviation for each measurement averaged over 60 s. A standard deviation of 0.01 ppm or less cannot be shown because the size of the data point exceeds the error bar.

tensifying until the measurement at 22:32 UTC, weakening afterwards and then intensifying again at 00:32 UTC. This variability in varying gradients was in agreement with changing meteorological conditions. Mean concentrations averaged over all measurements at each level were 2.091 ppm (10 m), 2.049 ppm (25 m), and 1.976 ppm (50 m).

According to the continuous measurements at the tower, the CH_4 concentration increased close to the ground even before sunset. The strongest increase was seen at all heights between 21:32 and 22.32 UTC with 0.25 ppm at 10 m, 0.15 ppm at 25 m, and 0.06 ppm at 50 m. Afterwards (23:32 UTC), concentration decreased at 10 and 25 m and increased at 50 m, leading to almost the same concentration at all heights (about 2.07 ppm).

Variations in agreement with a stabilization of the NBL were observed from the vertical potential temperature profiles. The stability of the atmosphere increased especially between 25 and 50 m until 22:32 UTC, while CH_4 accumulated in the NBL. Below 25 m, the atmosphere was slightly stable to neutral. In the following hour (23:32 UTC), a destabilization in the lowest 50 m of the atmosphere was detected and afterwards stable conditions developed again. This destabilization occurred simultaneously to the mixing of methane at all heights followed by a reestablished methane gradient. The results indicated a developing surface layer up to 25 m a.g.l. where methane accumulated, but

exchange with air above was not completely inhibited likely due to the fact that turbulence was not totally suppressed.

Wind in this night was mostly from west to northwest with low speed between 1–2 m s^{-1} and up to 3 m s^{-1} in 50 m (Fig. 7.2) and is shown for the same times as in Fig. 7.1. During the first two hours, wind direction was roughly the same with height showing a variability of about 50° (W to NW), while wind speed was about 2–3 m s^{-1}. Afterwards, wind speed was lower at 10 and

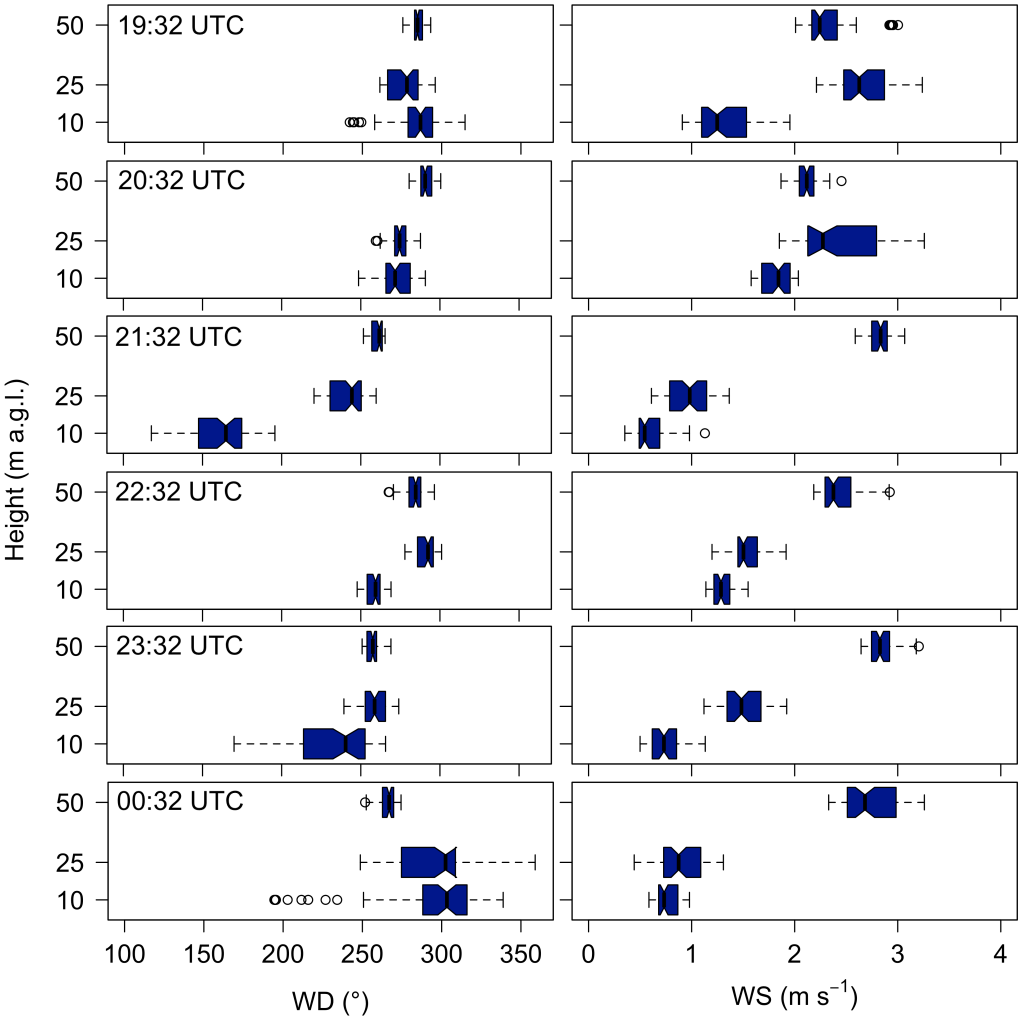

Fig. 7.2: Variability of wind direction (left) and speed (right) during 60 s hovering at 10, 25 and 50 m a.g.l. for flights between 19:32 UTC and 00:32 UTC in the night 21 to 22 July 2015. The blue box contains 50 % of the data and represents the interquartile range with the median as a black line. The dashed lines show maximum and minimum values in case those values are within the 1.5 interquartile range. Values outside this range (outliers) are represented with circles.

25 m. Mean wind direction stayed between west and northwest at 25 and 50 m, while at 10 m it changed from south (21:32 UTC) to west (22:32 UTC) and

back to southwest (23:32 UTC). So, southern directions were accompanied by a methane decrease, lower wind speeds and higher potential temperature. In contrast to that, at 22:32 UTC wind speed was higher than 1 m s^{-1} and potential temperature was 4–5 K lower than the hour before and after. During the last flight, wind direction changed back to northwest with high variability of about 100° at 10 m and 25 m, which was not seen at 25 m before. This higher variability occurred mostly during low wind speeds of 1–1.5 m s^{-1}.

ScaleX 2016 In the night from 6 to 7 July 2016, vertical methane concentrations were measured with the Pro X-3 up to 150 m, while with the smaller hexacopter F550 meteorological variables were determined. The first data of meteorological variables are available from 18:08 UTC, which was more than one hour before sunset (19:14 UTC). Even at that time, a stable layer was detectable from the ground up to about 50 m and with neutral conditions above (Fig. 7.3a). This stable layer increased its vertical extent up to 100–110 m until about midnight (00:01 UTC). One hour later, the stable layer close to the ground and especially the layer between 60 m and 80 m intensified their stability, while above neutral conditions remained. The potential temperature change between ground and above 80 m was 6 K. Afterwards, the stable layer increased again and during the last flight (04:00 UTC), which was half an hour after sunrise (03:26 UTC), only stable stratification could be detected throughout the whole vertical profile.
On the basis of the warming rate during the night, this development can be seen too (Fig. 7.3b). At the beginning of the night, the air cooled down over the whole profiles with successive flights, which was even more pronounced close to the ground. Between 23:07 and 00:01 UTC, conditions remained similar, but afterwards the cooling was 1–1.5 K in the stable layer. A warming of almost 1 K was detected below 50 m between 02:00 and 03:00 UTC and a cooling of more than 1 K afterwards. In the residual layer above the NBL, potential temperature also decreased but on average only about 0.3 K h^{-1}. Although methane data were also available each hour, not all measurements passed the post-processing and therefore, only six out of the eleven flights could be analyzed (Fig. 7.3c). At the beginning of the night, methane was well mixed with height, only at about 100 m an increase was detected. Three hours later, the CH_4 concentration increased 0.2 ppm up to 80 m and about 0.1 ppm above that height. According to the CH_4 tower measurements nearby, the concentration increased almost continuously in this time. The same is true for the next three hours, when no hexacopter-based data were available. But at about 00:30 UTC, methane concentration decreased, which was also recorded by the

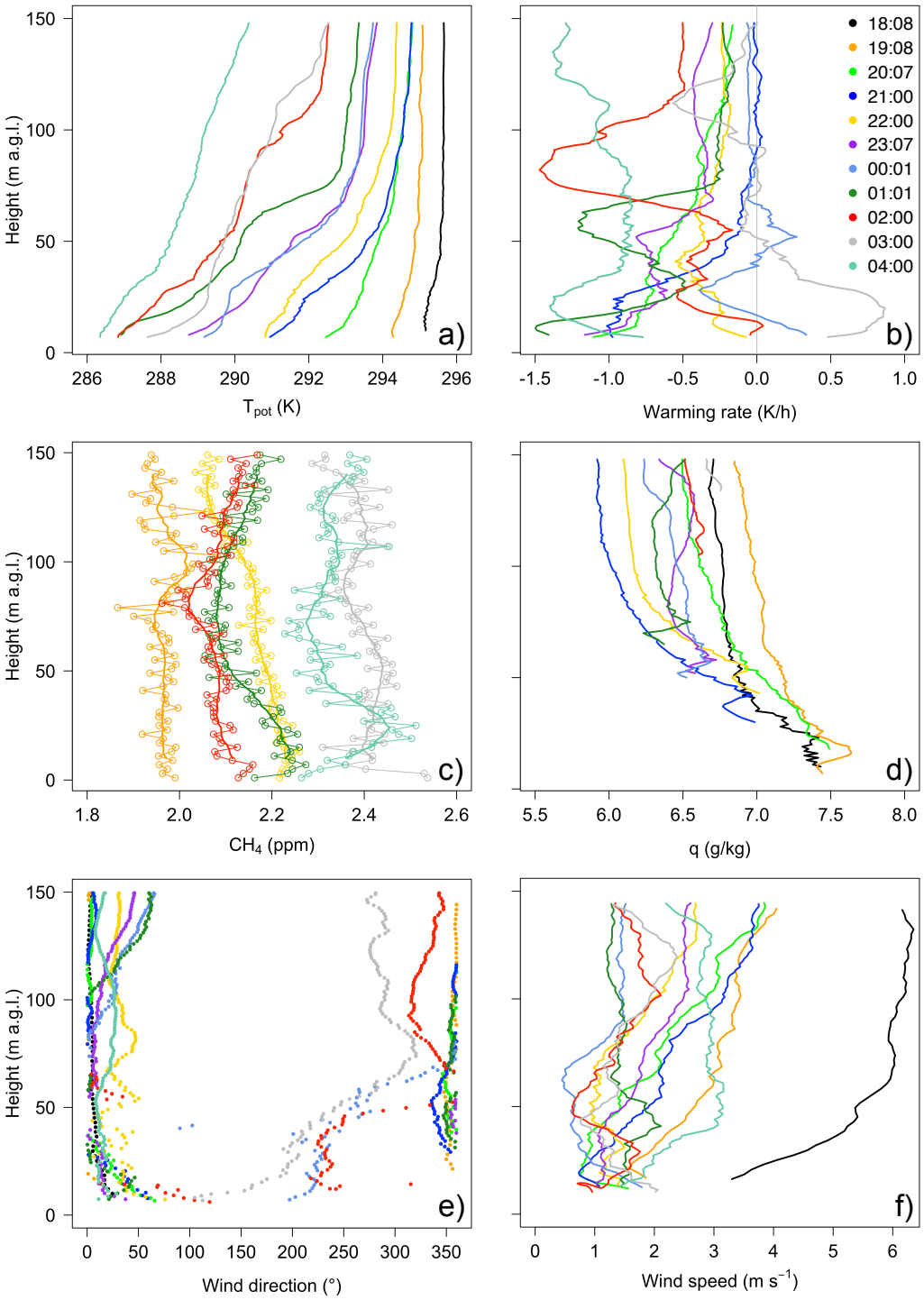

Fig. 7.3: Vertical profiles of meteorological conditions and methane concentrations in the night of 6 to 7 July 2016. a) shows the potential temperature (T_{pot}) in K, b) the warming rate in K h^{-1}, c) methane concentrations for data, which passed the post-processing, d) specific humidity (q) in g kg^{-1} for relative humidity up to 65 %, e) wind direction in °, and f) wind speed in m s^{-1}.

hexacopter flight at 01:01 UTC. While between 50 and 100 m the concentration decreased, it increased above 100 m and stayed constant below 30 m. During the next hour, concentration decreased further (about 0.05–0.1 ppm) below 100 m and increased up to 0.3 ppm at all heights between 02:00 and 03:00 UTC. During the last flight, a slight decrease was observed. However, a concentration rise of 0.3–0.4 ppm over night was detected with about 2.3 ppm after sunrise and about 1.9–2 ppm before sunset the previous day.
Bringing together the atmospheric stratification and methane concentration, the increase in the first half of the night was explainable with accumulated source emissions under stable atmospheric conditions leading to a concentration increase. The change afterwards was observed for both temperature and methane. Further intensification of the stable layer at 01:00 UTC did not lead to an immediate increase in CH_4 concentration, but in the following hour methane could accumulate leading to the sharp increase at 03:00 UTC.
Considering humidity changes over the night (Fig. 7.3d), specific humidity (q) was 7.5 g kg^{-1} close to the ground and decreasing with height (about 7 g kg^{-1}) at the beginning of the night. Humidity increased above 50 m during the next hour and decreased less than 0.5 g kg^{-1} during the following hour. At 21:00 UTC, specific humidity decreased significantly to 6 g kg^{-1} above 100 m but less closer to the ground. In the following hours, humidity increased again and was relatively constant between 23:07 and 02:00 UTC followed by increasing values with the passing of time. This was expected due to ongoing evaporation from the surface.
In order to find the origin of the "disturbing" air mass, wind direction (Fig. 7.3e) and wind speed (Fig. 7.3f) were analyzed. Before sunset, wind speed was 2 m s^{-1} near the ground speeding up to 4 m s^{-1} at 150 m. After sunset, wind speed decreased to 1–2 m s^{-1}. Until 01:01 UTC, wind direction was predominantly from north throughout the whole profile, except at 00:01 UTC when wind direction changed to southwest below 60 m. The same occurred at 02:00 and 03:00 UTC with a wind direction change to south and southwest up to 50–70 m. Wind speed was low at that time. After sunrise, wind direction changed to north again and wind speed increased to 3 m s^{-1}.

Analyzing meteorological variables and methane together, the strong increase in methane concentration was simultaneous with a wind direction change from north to south. At the same time, wind speed was lower coming from southerly directions. The increase in concentration with wind direction and stability changes was also observed during the campaign in 2015 and could be caused by emissions from the dairy farms. These conclusions were supported by near-

surface continuous methane concentration measurements and data analyses from RASS for temperature and wind profiles (Schäfer et al., 2016).

7.3 Nocturnal Stability and Flux Estimation

As mentioned before, the nocturnal boundary layer varied over time in the night of 6 to 7 July 2016. For ten of the eleven flights, a NBL height was determined, but for the last flight after sunrise this was not possible because the NBL height was higher than 150 m (Tab. 7.1). Before sunset (19:14 UTC), a NBL was detectable indicating the already started cooling from the ground because no energy was coming from the sun anymore. As time progressed, this stable layer grew in the vertical up to 100 m and was disturbed by another air mass at 01:01 UTC. The NBL height decreased to 85 m and increased again afterwards until after sunrise when the layer was higher than 150 m.

Tab. 7.1: Nocturnal boundary layer heights, potential temperature change with height and Richardson (Ri) number determined with multicopter flights in the night of 6 to 7 July 2016.

Time (UTC)	**NBL height (m)**	T_{pot} **(K)/ 100 m**	**Ri number**
18:08	60 m	1	0.01
19:08	80 m	1	0.06
20:07	70 m	3	0.13
21:00	90 m	4.3	0.27
22:00	100 m	3.7	-0.07
23:07	100 m	5.2	0.55
00:01	100 m	4.6	-0.15
01:01	85 m	7.7	0.27
02:00	120 m	4.9	0.19
03:00	130 m	3.8	0.11
04:00	$>$ 150 m	-	-

Looking at the vertical temperature change within the NBL, differences of more than 7 K per 100 m were found. This means that with height potential temperature increased of more than 7 K within 100 m, which led to very stable atmospheric conditions. At the beginning of the night, the change was 1 K, but increased in the following hours until 01:01 UTC and decreased afterwards with sunrise approaching.

The magnitude of stability can be also seen on the basis of the Richardson number within the NBL indicating stable atmospheric conditions for values between 0 and 0.25 and very stable conditions for values $>$ 0.25, which is the critical number. According to the calculated values, a stable stratification

was predominating during the night and most pronounced at 23:07 UTC. The decrease of the Richardson number at 22:00 UTC was likely caused by the decreasing potential temperature gradient. In the second half of the night, the critical Ri number was only exceeded at 01:01 UTC when the NBL height dropped from 100 m to 85 m. At this time, potential temperature gradient was still around 4 K, but wind speed was lower and wind direction changed to southwest near the ground.

Looking at the sensible heat flux estimation based on the multicopter data, both positive and negative fluxes were observed in the night of 6 to 7 July 2016. As an example, three time periods with each two successive flights were chosen. The potential temperature did not change above the NBL height in those examples minimizing the presence of advection. Negative values represent fluxes from the atmosphere to the surface and positive values in the other direction. The first pair of flights was at 21:00 and 22:00 UTC (Fig. 7.4). Close to the ground, the sensible heat flux was -17 Wm^{-2} and decreasing with height until it reached zero above the NBL at about 90 m. The second flux was almost constant with height and showed values between 0 and -5 Wm^{-2}, while the third flux was positive in the first 20 m (5 Wm^{-2}) and negative afterwards with values between -5 and -10 Wm^{-2} below the NBL height. Half hourly surface sensible heat fluxes were -11 and -6 Wm^{-2} (18:00 and 18:30 UTC) and -3 Wm^{-2} (01:30 UTC) from the EC measurements at the tower (6 m). At 9 m, sensible heat fluxes were around -8 Wm^{-2} between 21:00 and 23:00 UTC and -21 Wm^{-2} at 02:30 UTC. Unfortunately, more values were not available and therefore not directly comparable. However, the values before midnight were similar, but multicopter estimates resulted positive values after midnight, which was not the case for measurements at the tower. Since methane concentrations from only six flights passed the post-processing, a flux estimation was not possible throughout the whole night. For the flight after sunrise, no NBL height could be detected, which led to four methane fluxes estimated from multicopter data (Tab. 7.2). As for the sensible heat flux, positive values are directed from the surface to the atmosphere and a negative flux the other way round. Methane accumulation, and thus a positive flux, was found until 22:00 UTC and slightly negative fluxes afterwards until 02:00 UTC. The flux between 02:00 and 03:00 UTC were positive and the highest of the estimations (6.9 $\mu g\ m^{-2}\ s^{-1}$). Ground-based fluxes did not compare well, because fluxes were higher or even had a reversed sign depending on the height at the tower taken for the estimates. In addition, methane concentration was assumed to decrease linearly with height and NBL heights were overestimated.

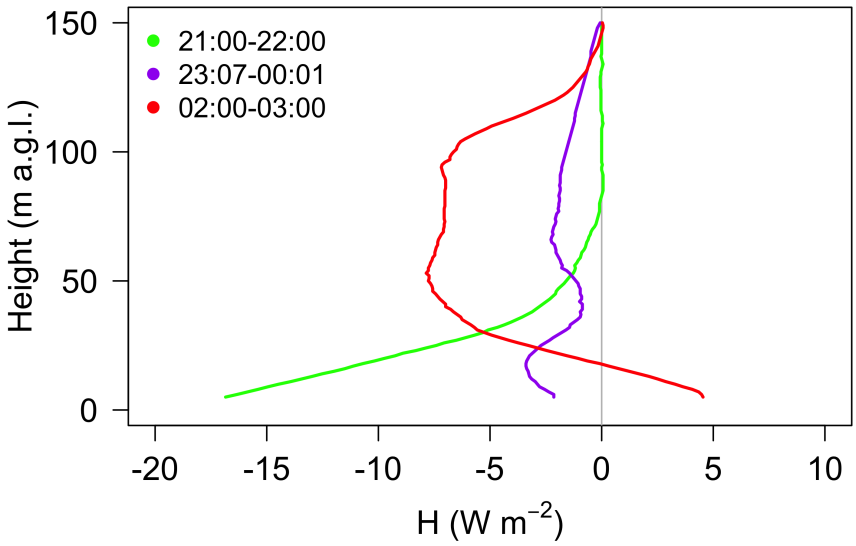

Fig. 7.4: Vertically integrated as well as spatially and temporally averaged sensible heat fluxes (H) by using multicopter data for the night of 6 to 7 July 2016.

Tab. 7.2: Nocturnal methane fluxes based on multicopter and ground-based data in the night of 6 to 7 July 2016. Times were chosen according to the data availability from the multicopter flights. Fluxes based on ground-based instrumentation could not be estimated for all times because the NBL height was missing. In addition, two flux values were calculated; the first using data at 1 m and the second using data at 9 m at the tower.

Time (UTC)	**Flux from CH_4 profile (μg m^{-2} s^{-1})**	**Flux from CH_4 tower (μg m^{-2} s^{-1})**
19:08-22:00	1.12	-
22:00-01:01	-0.28	-
01:01-02:00	-1.2	-5.5/ -8
02:00-03:00	6.9	9.7/ -5.8

As for the sensible heat flux, both positive and negative fluxes were found throughout the night. Data indicated that at the beginning of the night accumulation of methane in the NBL was predominating accompanied by an increasing vertical T_{pot} gradient, which was disturbed by another air mass coming from southerly directions. These conditions reversed again one to two hours before sunrise. The wind direction change during the night was likely caused by the Alpine pumping, which is a meso-scale mountain-valley wind system.

7.4 Transport and Footprint

To get information about where the measured air masses were coming from and which surfaces contributed to the estimated methane fluxes, a transport and a footprint model were applied.
Information about transport processes were derived by using the HYSPLIT model for backward trajectories (Draxler and Hess, 1998; Stein et al., 2015). The input data set used in this study was the GDAS (Global Data Assimilation System) with a resolution of 0.5°. Air temperature, relative humidity, the three wind components and air pressure are provided as three-dimensional information. Other variables as radiation, precipitation, etc. only have surface values.
Backward trajectories were used to get an idea where the measured air mass was several hours before and to derive wind speed and direction of this air mass at the measurement region (Fig. 7.5). In the beginning of the night, wind direction was from north with a speed of about 3.5 m s^{-1}, which turned towards northeast and slowed down to about 1 m s^{-1} with time until 23:00 UTC. Looking at the long-term trajectories six hours back, air masses actually were coming from northwest, which is consistent with the overall weather situation. After midnight, wind direction changed to south and west with low wind speeds close to the ground. At the same time, air masses were coming from westerly directions and changed to northerly directions after sunrise with increasing wind speed. As a result, wind speed and direction estimated by the HYSPLIT model corresponded to the measurements at the investigation site.

The Flux Footprint Prediction parameterization was used to get the main contribution area of the estimated fluxes (Kljun et al., 2015). Considering the footprint estimation, meteorological conditions as well as surface characteristics were included, but not where the measured air mass was originally located some hours ago. But a combination of the trajectories and footprints provided

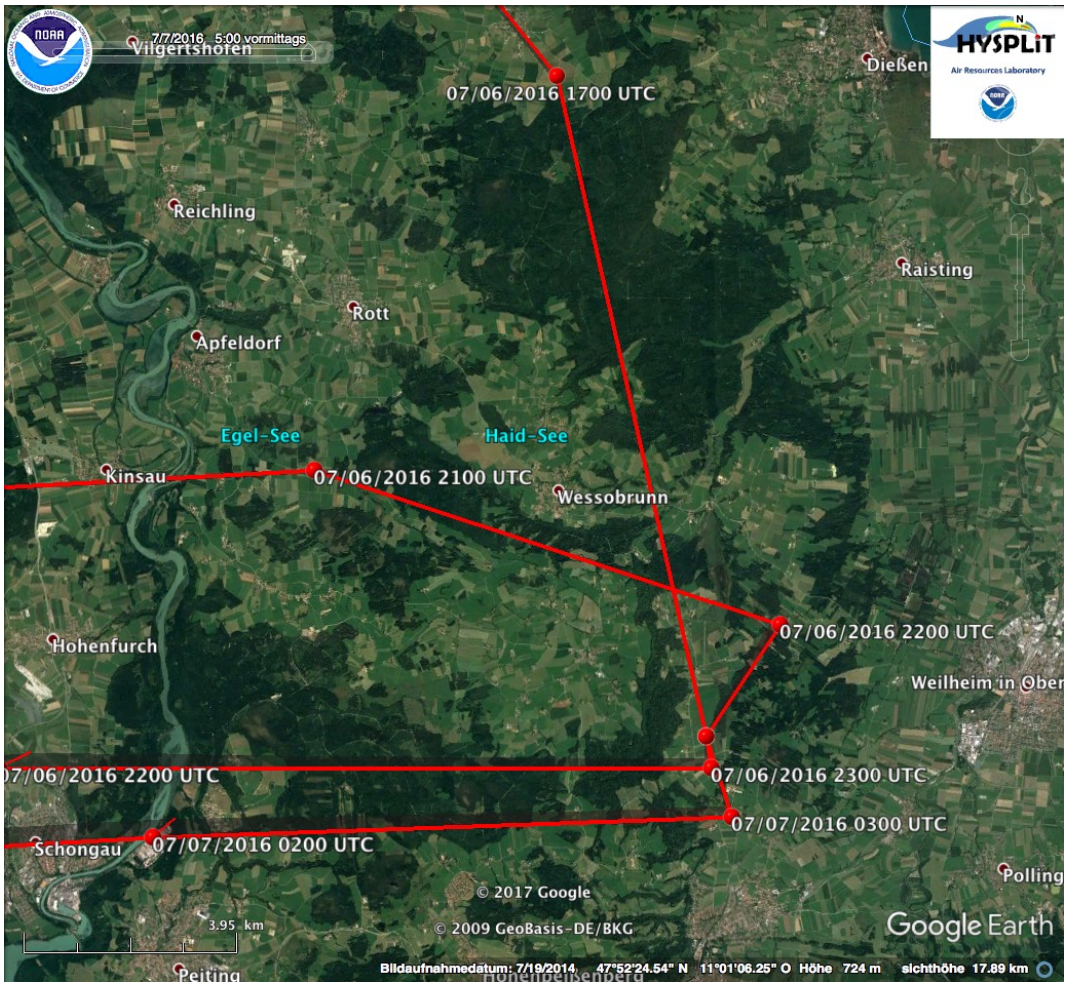

Fig. 7.5: HYSPLIT backwards trajectories for the night of 6 to 7 July 2016. At each trajectory the time and date is given in one hour steps. The red point without a label represents the investigation area DE-Fen, where all trajectories end.

a more detailed picture.

The two-dimensional footprint area was given as upwind distance and cross-wind distance (Fig. 7.6) corresponding to the x-axis and y-axis both with units of meters. In the figure, the footprint area was divided into four areas. The inner ellipsoid represents 20 % of the footprint area, the next larger one 40 %, then 60 % and the outer ellipsoid 80 %. Depending on the input variables, the shape and size of the ellipsoid changes and in addition the distance to the measurement point, which is located at the origin (0,0) of the coordinate system. So, those ellipsoids represent the footprint at one height but differ at other heights. Using different values for the NBL height and wind speed, the footprint contribution area changes, too. It has to be pointed out that due to the vertical profile measurements not only one footprint could be considered but at each height a corresponding one. Therefore, the actual footprint of the

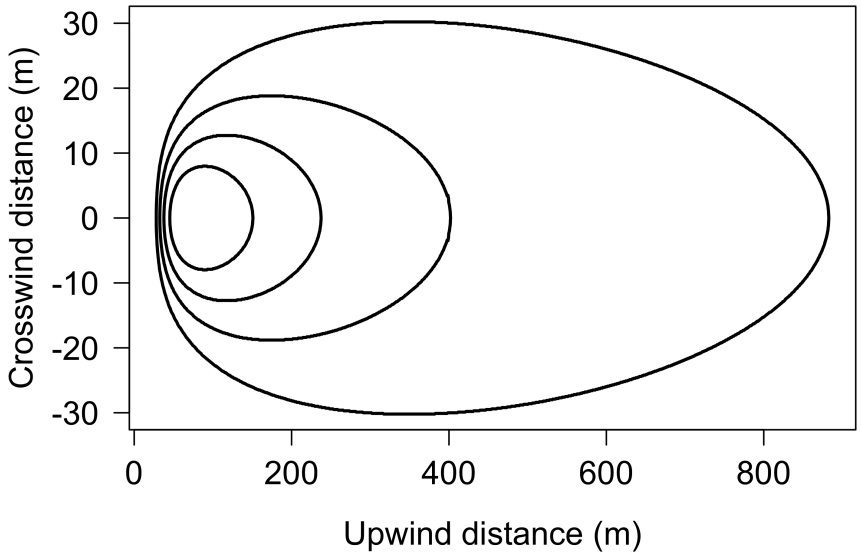

Fig. 7.6: Schematic cumulative footprint area. The inner ellipsoid represents 20 % of the whole footprint area, then 40 %, 60 %, and 80 %. The corresponding measurement is at the origin (0,0) of the coordinate system. A positive x-axis corresponds to the direction towards the wind.

estimated flux was a cumulative footprint from several heights.
In order to better see from which area the maximum contribution was coming, the footprint function of the crosswind integrated footprint (m^{-1}) was plotted against the upwind distance (Fig. 7.7a). This means that along the horizontal line through zero on the y-axis, the contribution was integrated for each upwind distance and plotted against it. Higher values correspond to an area with more contribution compared to others.

As an example, Fig. 7.7a shows the footprint function with $NBL_z = 100\ m$ and $WS_{mean} = 2\ m\ s^{-1}$. The distance with maximum contribution to the footprints ranged between 90 and 1400 m, while smaller values indicated a measurement height closer to the ground. In addition, the footprint area increased with increasing measurement height. While most of the contribution was coming within a distance of 1000 m at a measurement height of 20 m, the distance was more the 10 km at 80 m measurement height. The closest distance of contribution was also affected by measurement height, for example at 80 m the highest contribution was coming from 500 m and for other heights between 10 and 200 m in upwind direction.
Furthermore, the contribution to the footprint from several heights can be represented in relation to the maximum contribution (Fig. 7.7b). So, the area below each curve represents 100 % contribution and is related to the upwind

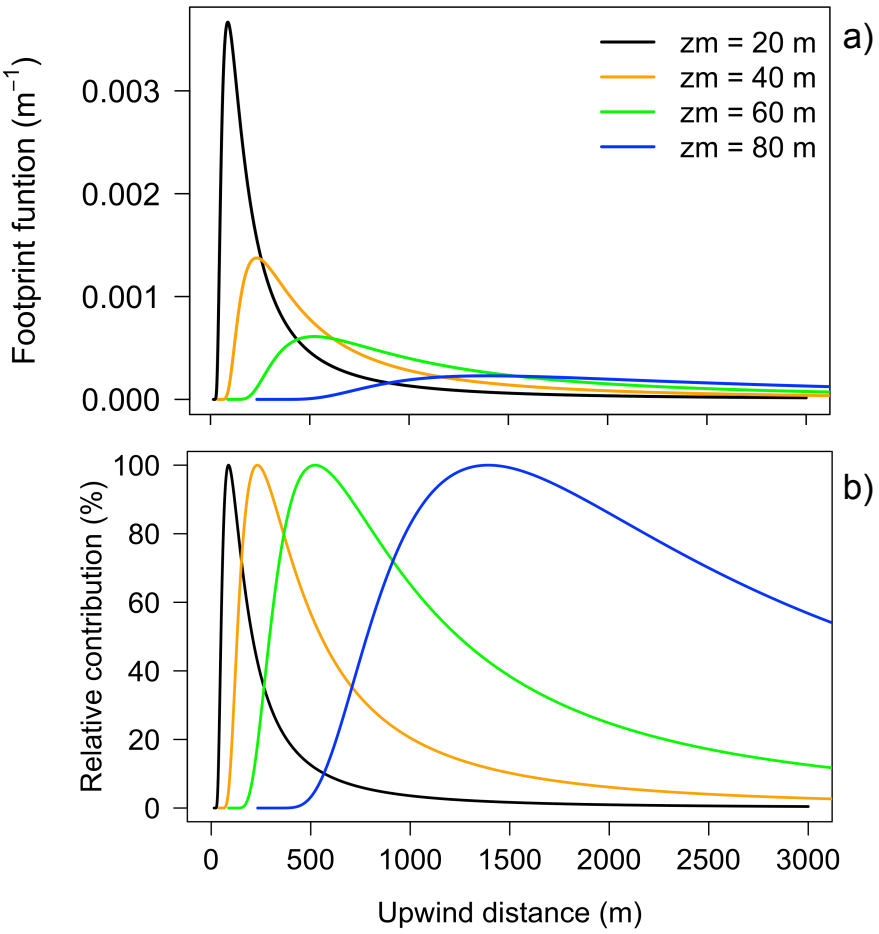

Fig. 7.7: a) Footprint function of the crosswind integrated footprint (m^{-1}) for a NBL height of 100 m and a mean wind speed of 2 m s^{-1}. b) Relative contribution (%) of upwind distance to footprint for measurements at several height.

distance (x-axis). For example, a contribution of 50 % is coming from an area, which is 250 m long, in upwind direction, while the length of the area is increasing with measurement height. This indicates that half of the contribution could be traced back to less than 10 % of the upwind distance of the footprint.

In order to get the cumulative footprint for one vertical profile, the contribution at each upwind distance with a resolution of 100 m was summed up. Then the contribution at the discrete distance levels was related to the maximum contribution to obtain the relative impacts of all footprints to the cumulative footprint. Comparing the different input variables of NBL height and mean wind speed, 90 % of the contribution was explained by an upwind distance between 500 and 1300 m. The "extreme" examples are shown in Fig. 7.8. A decreasing NBL height led to a smaller contribution area and the same was true for decreasing wind speed. The area with the highest contribution was between

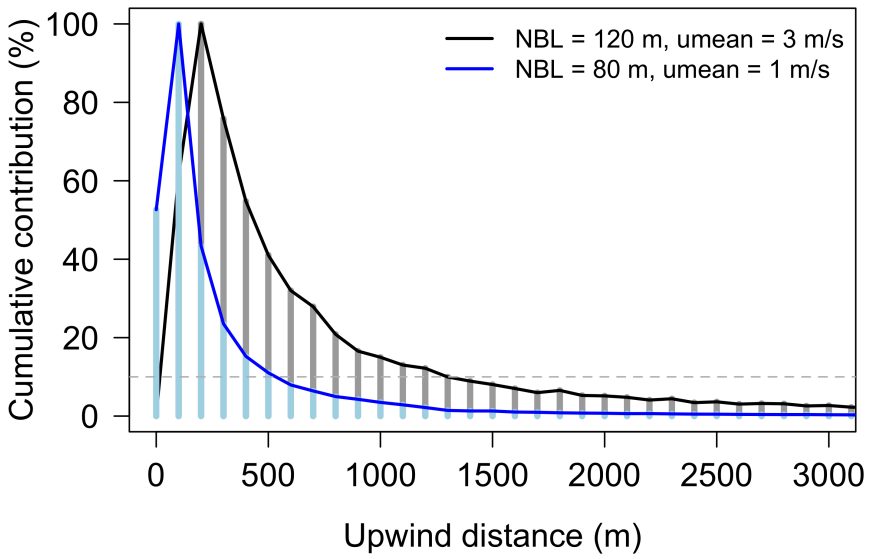

Fig. 7.8: Two cumulative footprints for one vertical profile with different input variables. The black line indicates values of $NBL_z = 120\ m$ and $WS_{mean} = 3\ m\ s^{-1}$ and the blue line $NBL_z = 80\ m$, $WS_{mean} = 1\ m\ s^{-1}$. Above the horizontal dashed grey line the contribution to the cumulative footprint is 90 %.

100 and 200 m in upwind direction. The shift of the curves was more influenced by wind speed than by NBL height. Since those two curves represent the variability in atmospheric conditions, which were measured by the multicopter during the night, this shows the range the footprints may have had. But this is only true considering the other input variables as realistic.

Taking the trajectories and footprints for the night from 6 to 7 July 2016 together, main sources of methane were likely within a radius of about 500–1500 m from the measurement site independent on wind direction (Fig. 7.9). Looking to the north of the site, predominating land uses were grassland and agricultural fields, to the west and east forest and to the south grassland and fields, but also dairy farms. As a result, higher methane concentrations occurred with southern wind directions and therefore the farms acted as major methane sources as suspected from investigations from the previous summer. But since accumulation was found during northerly winds too, the farms further to the north and northwest likely had an impact as well, but also grassland and agricultural fields. Accumulation during northerly winds could be an indicator for the underestimation of the size of the footprints during stable atmospheric conditions.

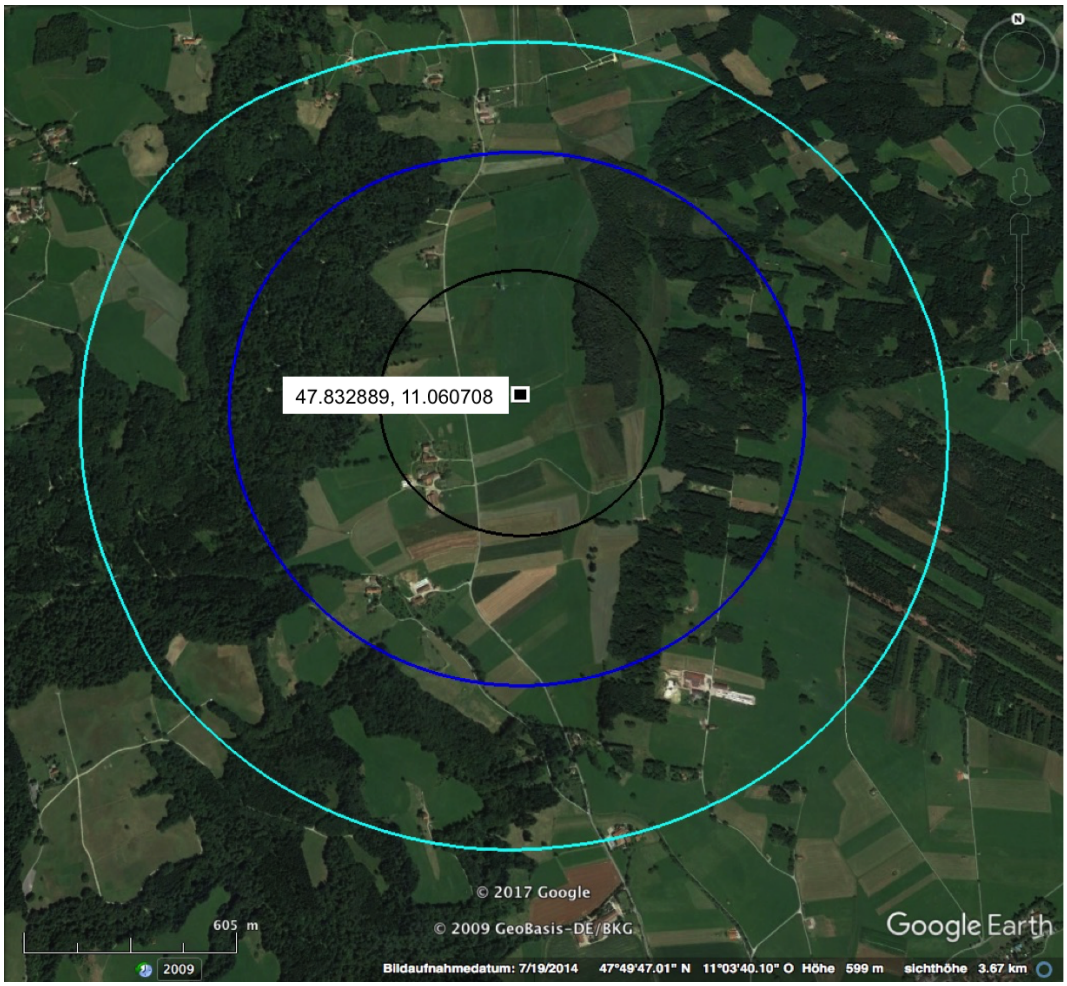

Fig. 7.9: Major contribution areas to cumulative footprints to flux estimation. The black circle has a radius of 500 m around the measured profile, the blue 1000 m and the light blue 1500 m.

7.5 Summary and Discussion

The results of measuring meteorological conditions and methane concentrations at the same time showed that multicopter platforms provide a suitable tool for nocturnal methane emission estimates. Two different approaches were tested, while the second was preferable for further investigations and estimates. Only because meteorology and the air constituent of interest (i.e. methane) were measured simultaneously, estimation of emissions was achieved. In addition, localization of the measured air masses was possible by using a transport and footprint model. Using those kind of measurements, emission estimates are also possible for other surfaces with methane sources and sinks.

ScaleX 2015 Methane concentration increases close to the ground were found below a nocturnal inversion. Using a tethered balloon instead of a multicopter, Choularton et al. (1995) detected a concentration drop of 0.05 to 0.075 ppm

from the inversion layer to the layer above. This was in agreement with the multicopter measurements at 10 and 25 m a.g.l. being below 0.1 ppm in the first half of the night while a stable stratification occurred.
The vertical range of measurements was limited by the payload capacity of the multicopter and the lateral extent of the measurements was restricted by electricity availability for the methane analyzer. Using a tethered balloon, Denmead et al. (2000) pointed to the problem that it was difficult to adapt to varying NBL heights with fixed installed sampling lines. This shortcoming can be overcome with the multicopter because hovering heights can be easily changed in the flight plan. A limitation of the setup used in this study was that the vertical range of 50 m is usually not enough to cover the whole NBL height. To overcome this limitation, a multicopter with a higher payload would be necessary with the ability of carrying a longer tube or an onboard methane sensor. Apart from that, the vertical extension of meteorological measurements to the NBL height without the tube would be beneficial for interpretation, although no methane data would be available.

The combination of the wind and concentration measurements suggest that the significant methane increase between 21:32 UTC and 22:32 UTC was caused by emissions from the dairy farms (about 150–200 dairy cows) to the west of the measurement location (about 700 m distance). Actually, the methane mixing ratio started to increase around 22:00 UTC, when wind direction changed from more southern to predominating western directions (250–300°) with wind speeds of around 1.5 m s^{-1}. Below 25 m, the atmosphere was mixed as seen from the vertical potential temperature profile. Taking into account these conditions, dispersion of a methane plume is low. According to Dämmgen et al. (2012), an emission rate of 14.5 g h^{-1} cow^{-1} can be assumed. This value was estimated for dairy cows in Bavaria (Germany) based on the IPCC (2006). Depending on the width of the methane plume(s) (100–500 m) coming from the farms, the methane concentration increase of about 0.15 ppm in half an hour would lead to emissions from about 90–450 cows. In comparison to the actual number of dairy cows, measured methane concentrations were plausible. For further investigation, an approach similar to that of Hacker et al. (2016) would be suitable to calculate emission rates by flying upwind and downwind of the farms and measuring the vertical and horizontal extent of the plume.

ScaleX 2016 A comparison of concentration gradients from 2015 and 2016 was hardly feasible because the time frames of available data did not match. But in both years, stable conditions led to methane accumulation, which was also dependent on wind conditions. In contrast, disturbances in atmospheric layering

reduced the methane concentration. Those disturbances were explainable with the cold air drainage from the Alps, the already mentioned Alpine pumping (Lugauer and Winkler, 2005; Graf et al., 2016). This phenomenon occurs on up to 20 % of the days each year under synoptic calm conditions. During summer its main purpose is ventilation. Therefore, it still needs to be investigated for more nights how methane concentrations develop under such conditions.

Looking at the flux estimation of sensible heat and methane, some limitations have to be considered. Starting with the former, both positive and negative sensible heat fluxes were estimated at nighttime, which were similar to the ones calculated with the EC method at 6 and 9 m. The same is true for fluxes estimated around sunset by Bonin et al. (2013). Since the NBL height was an essential part in estimating the flux, its uncertainty highly affected the magnitude of the flux. Therefore, it is advised for further campaigns to plan successive flights within a shorter time period of about 10–15 min when stationary atmospheric conditions are rather available. Within that time span, potential temperature in the residual layer is assumed to be constant since its cooling rate is about 0.2 K h^{-1} (Ha and Mahrt, 2003). Nonetheless, one hour difference between two flights is a reasonable time period during daytime (Reuder et al., 2016). In addition, determination of the NBL height based on potential temperature profile is one approach (Choi et al., 2011), while other mentioned methods lead to different results in the order of ±10 m.
For determination of methane fluxes, NBL height was crucial too, because this is the height up to which the flux was integrated. In case no concentration change above the NBL height occurred, the difference was zero and did not add up to the flux.
According to the German methane emission rates, 67 Mio. tonnes CO_2-equivalent (about 3 Mio. tonnes CH_4) were emitted from the agricultural sector in 2015. Normalizing this to the whole agricultural area of 184332 km^2, this leads to a methane flux of 0.5 μg m^{-2} s^{-1} (UBA, 2017a,b) and is similar to the estimated values in this thesis. Pattey et al. (2006) and Stieger et al. (2015) found values of methane fluxes in the same order of magnitude during nighttime while measuring above a forest and emissions from a dairy farm, respectively. Both also pointed out that especially advection and intermittent turbulent processes were a problem when calculating nocturnal methane fluxes. Horizontal advection has to be considered in case the footprint area is not homogeneous and so the flux is not only a result of a single land cover. Besides, intermittent turbulence is caused by topography when local wind systems build up as for example cold air drainage. In addition, entrainment mixing at

the nocturnal inversion layer occurs in case the inversion is not strong enough to prevent mixing between NBL and residual layer (Culf et al., 1999), which also happened during the presented flights.
Consequently, meteorological conditions in the investigated night were not ideal for the determination of methane fluxes, but the magnitude of fluxes was similar to other studies. These kind of measurements are important in order to use the results for scaling emissions in models up to the regional scale (Pattey et al., 2006). It was reported in several studies that using the NBL method emission rates are similar as in inventories stated (Emeis, 2008; Harper et al., 2011; Stieger et al., 2015).

Comparing the multicopter-based methane flux estimates with the ones from tower and ceilometer measurements, it was obvious that without having the whole profile or at least a few measurement points the uncertainty of the fluxes were even higher. Although it was assumed that methane concentration decreased linearly with height to the background concentration, the measured concentration at the tower was crucial for the result. Since concentrations were highly variable during nighttime, which was also found by Pattey et al. (2006), this even led to a reversed estimated flux. In addition, the NBL height measured by the ceilometer was higher and changed several hundreds of meters within one hour. Therefore, an overestimated NBL height is likely to lead to an overestimated methane flux.
From this point of view, the multicopter measurements were necessary in order to improve the estimates of methane fluxes.

Concerning the transport processes, footprint estimation showed uncertainties too. Since there is no footprint model optimized for stable atmospheric conditions, the flux footprint prediction parameterization (Kljun et al., 2015) was used because it was easy to apply, did not need many input variables and tended to have reasonable results even for stable stratification (Wittebol, 2009; Glazunov et al., 2016; Heidbach et al., 2017). Compared to large eddy simulations (LES), the FFP model underestimates the footprint area (Glazunov et al., 2016), but LES is not easy to apply. With regard to the extent of the estimated nocturnal footprints this is reasonable because for stable stratification the footprint extends several kilometers towards the upwind distance, which was recorded by several studies (Stull, 1988; Beswick et al., 1998; Göckede et al., 2004; Harper et al., 2011; Bamberger et al., 2014; Stieger et al., 2015). The underestimation is likely explained by the fact that input variables could not be chosen according to stable conditions. Both the friction velocity and deviation of lateral wind speed could be even smaller than the used values.

In addition, the roughness length was not considered but mean wind speed instead. According to Schmid (1997) the effect of the roughness becomes less important as the measurement height increases. But with regard to forested areas those would increase the roughness significantly and therefore could reduce the size of the footprint. To account for the uncertainty of the NBL height and mean wind speed, ensemble calculations were done in order to get lower and upper limits of the footprint extent.

As for the campaign in 2015, there was only a small data set for methane measurements available for analysis in 2016, but it showed that the onboard sensor was working and the application for nocturnal vertical profiles was reasonable. But further investigations with the senor are possible and necessary.
During daytime for example, vertical profiles showed that the atmosphere was not totally mixed even under unstable conditions. While methane concentration was similar with height close to the ground, this was not the case above 80 m a.g.l. It seemed that a methane plume was transported from west to the investigation area, but due to the slope and relatively high wind speeds this was not mixed downwards to the ground and therefore only seen at higher altitudes. Looking for sources within a few kilometers to the west, there are actually dairy farms. So, daytime investigations are another application with the onboard sensor but then it would be also necessary to measure all the meteorological variables with this hexacopter. From the payload point of view this is not the limiting factor but rather the short possible flying time in case horizontal and vertical flights are needed, for example, to measure the extent of the methane plume.

8 Conclusions and Outlook

This thesis elaborated the advantages of a hexacopter-based approach to investigate interactions between the atmosphere and the land surface. Based on two scientific topics, these advantages were identified and presented.

First, the results demonstrated the feasibility of a multicopter-based approach to detach measurements of meteorological variables and methane concentrations from fixed towers to achieve mobile and flexible investigations. Especially for difficult-to-access regions, sensible ecosystems or locations where high towers are prohibited, multicopter-based measurements could be a suitable alternative. An adaptation of the flight pattern to the used sensors was necessary to ensure that it is appropriate for all simultaneously measured variables. Otherwise, further calculations would not be possible. Consequently, the demonstration of the feasibility was the requirement towards addressing the two scientific objectives of the this thesis.

Second, estimation of energy balance components and their input variables' variability were derived from hexacopter measurements. Daily ET rates resulted in reasonable values over the test site, i.e. a grassland site in the foothills of the Bavarian Alps. Although those measurements took place at an area with a well-developed infrastructure, a hexacopter platform offers high potential for measurements in sensible ecosystems and only remotely accessible regions. In contrast to satellite and aircraft remote sensing data, hexacopters provide a high spatio-temporal resolution and flexibility in data acquisition. So, the repeatability is possible within stationary conditions in the atmosphere. Besides, hexacopter-derived ET estimations are also possible during cloudy weather conditions when satellite data are not available.
While spatial variations were mainly caused by soil and vegetation cover inhomogeneities, temporal variations were mainly influenced by weather and time of the day. Since no rain occurred during the period of investigations, soil moisture decreased with time. This and changing weather conditions led to spatial and temporal variability of meteorological, surface and soil variables.
The measurements took place below the blending height in order to observe spatial inhomogeneities. Above the blending height those inhomogeneities are

smoothed with no differentiation of the internal boundary layers. This height provides information for up- and down-scaling processes in meteorological, hydrological and climate models.
The major driving variables of the energy balance were on the one hand solar radiation, acting as energy source, and on the other hand the land surface with vegetation cover and surface temperature. Those variables had a high impact according to PCA results. But this is only valid for the investigated area and is likely different for other areas depending on topography, land use and geographical location. So, the higher the influence on the estimation, the more pronounced the uncertainty in the error estimation. For example, wind speed was among the more important variables and the relatively high uncertainty of its calculation led to high error bars. For regions, where wind speed is even more important like in a deep valley, this could be a greater challenge.
All in all, the application of hexcopters for *ET* estimations provides a flexible alternative to satellite data with the possibility of repeating the measurements within a short time period (stationary conditions) and at the same time having a good horizontal resolution within a few meters.

Third, the vertical distributions of nocturnal methane concentrations above an agricultural area under stable atmospheric conditions were focused by using two different approaches based on hexacopter platforms. With information about both methane and meteorological conditions, the estimation of methane emissions was achieved. Comparing the measured methane concentration to ground-based reference instrumentation, both methods revealed good agreement. While the onboard sensor provides more flexible applications than the tube-based measurements, the advantage of the tube is the possibility of varying the gas of interest by exchanging the ground-based analyzer. But compared to the approach of using tethered balloons instead, the hexacopter's operation is easier and more flexible in terms of flying location and vertical profile setup.
Looking at the flux estimation itself, the hexacopter-based approach is more reliable compared to ground-based instrumentation. The highly variable near surface methane concentration within the first 10 m was influencing the flux estimation and led to both over- and underestimated fluxes. Besides, without the vertical information, it is more difficult to differentiate between local and regional sources.
Due to the stable atmospheric conditions during night, measurements throughout the whole NBL are necessary. This is important to determine the height of the NBL and to detect wind direction changes within the profile, which is important in terms of footprint analysis. The changing wind direction, for

example, led to highly variable methane fluxes and so meteorological conditions are important for interpretation. Footprint estimations further showed that most of the contribution to the methane fluxes was coming from local sources within a radius of 1–2 km. Therefore, methane point sources with high emissions have a significant influence on the nocturnal flux, which led to higher values than in the emission inventories.
Altogether, hexacopter-based investigations of nocturnal methane distributions and emission estimates showed good results. Multicopters provide a mobile and flexible tool for vertical and horizontal investigations. Its operation is transferable to other purposes and land use types as well. Since the whole vertical profiles are addressed with this method, more information is collected than with ground-based measurements. In addition, the measurements of necessary variables is possible simultaneously.

Generally, the topics of this thesis dealt with land surface-atmosphere exchange, which was one of the focused aspects of the ScaleX campaigns organized by the KIT/IMK-IFU. Within the framework of those campaigns, hexacopter-based measurements could be tested and possibilities for operation of UAVs were identified. In the end, particular contributions to the two ScaleX campaigns were the following:

- Extending tower-based measurements of meteorological variables, as air temperature, relative humidity and wind, in the vertical in order to fill the gap between ground-based instrumentation and remote sensing techniques/ aircraft measurements with focus at heights of 10 to around 60 m (see chapter 5),

- Identification of horizontal gradients of hydrometeorological variables above a grassland site in the foothills of the Bavarian Alps, which was assumed to be homogeneous (see chapter 6),

- Estimation of spatial variability of surface energy balance components in the footprint area of the EC station to compare hexacopter-based estimates with direct measurements as the EC method (see chapter 6),

- Feasibility of two mobile methods based on hexacopter platforms for vertical methane measurements to investigate the whole extent of the NBL with simultaneous meteorological measurements (see chapter 7),

- Nocturnal flux estimation of sensible heat and methane as extension to EC measurements, which are challenged under stable stratification, and to verify agricultural methane emission rates (see chapter 7),

- Suitable data for comparison with model simulations and as information for up-scaling processes (see chapter 6 and 7).

It could be shown that UAVs provide a flexible and manageable flying system for different kinds of research questions and results matched the ones acquired with other instrumentation. More measurements are necessary to identify weather and seasonal variations in land surface-atmoshpere interactions. In addition, the multicopters were only operated above a grassland site, but other land uses as forests or peatlands are important and interesting as well. UAVs provide a suitable alternative especially for difficult-to-access regions, sensible ecosystems and locations where high towers are prohibited.
Until now, continuous UAV-based measurements are difficult to manage and flying time of especially multicopters is still limited to 30–45 min the most. But further miniaturization of sensors and improved batteries could overcome these existing limitations.

Data acquired by UAVs are also suitable for model comparison and evaluation. As mentioned in the last chapter, there is still no flux footprint model available, which is optimized for stable atmospheric conditions. The used FFP model of this study can be applied for stable conditions, but specific limitations occur. For example, the Monin-Obukhov similarity theory is only valid when turbulent processes are predominating. But during nighttime, turbulence can be intermittent and accordingly the theory is not applicable. Therefore, models adapted to these conditions would be beneficial for future investigations with regard to greenhouse gas emissions. Scale interrelations may occur as a major problem because during day the footprint is affected by local sources, while during nighttime the footprint can be larger consisting of both local and regional sources.
Given the resolution of the multicopter-based measurements, large eddy simulation results driven by reanalysis data can match the scale of those observations. So, hourly UAV data of profiles from meteorological variables can be compared to the model output in order to investigate its performance and to see whether the model is able to simulate the course of day. Furthermore, meteorological effects above different land use types could be simulated by generating multicopter-based meteorological data over, for example, grassland and forest aiming at simulating the effects of land use change to meteorological conditions based on large eddy simulation.

For future applications of the described multicopters, additional measurements of course would be beneficial. While a lot of data were available for spatial ener-

gy balance estimation, especially vegetation characteristics were missing. Even a camera for visible imagery would be beneficial to know surface characteristics for interpretation of measured LST. Together with near-infrared information, the NDVI could be determined. To get these information georeferenced and with a similar resolution as other data, a few hundreds of grams are necessary as additional payload.
Further investigations could go in the direction of turbulence measurements. It was possible to determine wind speed and direction from the attitude and GPS data, so turbulence might be possible as well. Faster sensors to determine the attitude and position are maybe needed as well as further data as spinning speed of propellers and current. In addition, it could be easier to use a smaller multicopter because its inertia is smaller and so its reaction to surrounding conditions faster. Turbulence and fast air temperature as well as humidity would allow the direct measurement of turbulent sensible and latent heat fluxes. The dew point mirror used in Metzger et al. (2012) is fast enough for this kind of measurements.

All in all, UAVs provide a feasible alternative to existing measurement methods for various scientific applications in the PBL. Their operation is especially valuable because interactions between different scales can be addressed, which are useful for up-scaling and down-scaling processes. UAVs provide a flexible and beneficial method for those investigations and can be adapted to a great variety of research questions.

References

Abdi, H. and Williams, L. J.: Principal component analysis, Wiley Interdisciplinary Reviews: Computational Statistics, 2, 433–459, doi:10.1002/wics.101, 2010.

Altstädter, B., Platis, A., Wehner, B., Scholtz, A., Wildmann, N., Hermann, M., Käthner, R., Baars, H., Bange, J., and Lampert, A.: ALADINA-an unmanned research aircraft for observing vertical and horizontal distributions of ultrafine particles within the atmospheric boundary layer, Atmospheric Measurement Techniques, 8, 1627, 2015.

Alvarado, M., Gonzalez, F., Fletcher, A., and Doshi, A.: Towards the development of a low cost airborne sensing system to monitor dust particles after blasting at open-pit mine sites, Sensors, 15, 19 667–19 687, 2015.

Alvarado, M., Gonzalez, F., Erskine, P., Cliff, D., and Heuff, D.: A Methodology to Monitor Airborne PM10 Dust Particles Using a Small Unmanned Aerial Vehicle, Sensors, 17, 343, doi:10.3390/s17020343, 2017.

Andersen, T., Scheeren, B., Peters, W., and Chen, H.: A UAV-based active AirCore system for measurements of greenhouse gases, Atmospheric Measurement Techniques, 11, 2683–2699, doi:10.5194/amt-11-2683-2018, 2018.

Anderson, M. C., Norman, J. M., Diak, G. R., Kustas, W. P., and Mecikalski, J. R.: A two-source time-integrated model for estimating surface fluxes using thermal infrared remote sensing, Remote sensing of environment, 60, 195–216, 1997.

Andrews, A. E., Kofler, J. D., Trudeau, M. E., Williams, J. C., Neff, D. H., Masarie, K. A., Chao, D. Y., Kitzis, D. R., Novelli, P. C., Zhao, C. L., Dlugokencky, E. J., Lang, P. M., Crotwell, M. J., Fischer, M. L., Parker, M. J., Lee, J. T., Baumann, D. D., Desai, A. R., Stanier, C. O., De Wekker, S. F. J., Wolfe, D. E., Munger, J. W., and Tans, P. P.: CO2, CO, and CH4 measurements from tall towers in the NOAA Earth System Research Laboratory's Global Greenhouse Gas Reference Network: Instrumentation, uncertainty analysis, and recommendations for future high-accuracy greenhouse

gas monitoring efforts, Atmospheric Measurement Techniques, 7, 647–687, doi:10.5194/amt-7-647-2014, 2014.

Astuti, G., Giudice, G., Longo, D., Melita, C. D., Muscato, G., and Orlando, A.: An overview of the "Volcan Project": An UAS for exploration of volcanic environments, Unmanned Aircraft Systems, pp. 471–494, doi:10.1007/978-1-4020-9137-7_25, 2008.

Aubinet, M., Vesala, T., and Papale, D., eds.: Eddy covariance: a practical guide to measurement and data analysis, Springer Science & Business Media, 2012.

Baklanov, A., Grimmond, C. S. B., Carlson, D., Terblanche, D., Tang, X., Bouchet, V., Lee, B., Langendijk, G., Kolli, R. K., and Hovsepyan, A.: From urban meteorology, climate and environment research to integrated city services, Urban Climate, 23, 330–341, doi:10.1016/j.uclim.2017.05.004, 2018.

Bakwin, P. S., Tans, P. P., Hurst, D. F., and Zhao, C.: Measurements of carbon dioxide on very tall towers: results of the NOAA/CMDL program, Tellus B: Chemical and Physical Meteorology, 50, 401–415, 1998.

Baldocchi, D. D.: Assessing the eddy covariance technique for evaluating carbon dioxide exchange rates of ecosystems: past, present and future, Global Change Biology, 9, 479–492, 2003.

Baldocchi, D. D., Hincks, B. B., and Meyers, T. P.: Measuring biosphere-atmosphere exchanges of biologically related gases with micrometeorological methods, Ecology, 69, 1331–1340, 1988.

Bamberger, I., Stieger, J., Buchmann, N., and Eugster, W.: Spatial variability of methane: Attributing atmospheric concentrations to emissions, Environmental Pollution, 190, 65–74, 2014.

Banta, R. M., Pichugina, Y. L., Kelley, N. D., Hardesty, R. M., and Brewer, W. A.: Wind energy meteorology: insight into wind properties in the turbine-rotor layer of the atmosphere from high-resolution Doppler lidar, Bulletin of the American Meteorological Society, 94, 883–902, 2013.

Barlow, J., Best, M., Bohnenstengel, S. I., Clark, P., Grimmond, S., Lean, H., Christen, A., Emeis, S., Haeffelin, M., Harman, I. N., et al.: Developing a research strategy to better understand, observe, and simulate urban atmospheric processes at kilometer to subkilometer scales, Bulletin of the American Meteorological Society, 98, ES261–ES264, 2017.

Båserud, L., Reuder, J., Jonassen, M. O., Kral, S. T., Paskyabi, M. B., and Lothon, M.: Proof of concept for turbulence measurements with the RPAS SUMO during the BLLAST campaign, Atmospheric Measurement Techniques, 9, 4901, 2016.

Bastiaanssen, W. G. M., Menenti, M., Feddes, R., and Holtslag, A.: A remote sensing surface energy balance algorithm for land (SEBAL). 1. Formulation, Journal of Hydrology, 212, 198–212, 1998.

Beekmann, M., Prévôt, A. S., Drewnick, F., Sciare, J., Pandis, S. N., Denier van der Gon, H., Crippa, M., Freutel, F., Poulain, L., Ghersi, V., et al.: In situ, satellite measurement and model evidence on the dominant regional contribution to fine particulate matter levels in the Paris megacity, Atmospheric chemistry and physics, 15, 9577–9591, doi:10.5194/acp-15-9577-2015, 2015.

Bergamaschi, P., Houweling, S., Segers, A., Krol, M., Frankenberg, C., Scheepmaker, R. A., Dlugokencky, E., Wofsy, S. C., Kort, E. A., Sweeney, C., Schuck, T., Brenninkmeijer, C., Chen, H., Beck, V., and Gerbig, C.: Atmospheric CH4 in the first decade of the 21st century: Inverse modeling analysis using SCIAMACHY satellite retrievals and NOAA surface measurements, Journal of Geophysical Research: Atmospheres, 118, 7350–7369, doi:10.1002/jgrd.50480, 2013.

Berger, B. W., Davis, K. J., Yi, C., Bakwin, P. S., and Zhao, C. L.: Long-term carbon dioxide fluxes from a very tall tower in a northern forest: Flux measurement methodology, Journal of Atmospheric and Oceanic Technology, 18, 529–542, 2001.

Berman, E. S., Fladeland, M., Liem, J., Kolyer, R., and Gupta, M.: Greenhouse gas analyzer for measurements of carbon dioxide, methane, and water vapor aboard an unmanned aerial vehicle, Sensors and Actuators B: Chemical, 169, 128–135, 2012.

Beswick, K., Simpson, T., Fowler, D., Choularton, T., Gallagher, M., Hargreaves, K., Sutton, M., and Kaye, A.: Methane emissions on large scales, Atmospheric Environment, 32, 3283–3291, 1998.

Bluestein, H., McCaul Jr., E., and Byrd, G.: Thermodynamic measurements under a wall cloud, Monthly Weather Review, 118, 794–799, 1990.

Bogena, H., Herbst, M., Huisman, J., Rosenbaum, U., Weuthen, A., and Vereecken, H.: Potential of wireless sensor networks for measuring soil water content variability, Vadose Zone Journal, 9, 1002–1013, 2010.

Bonin, T., Chilson, P., Zielke, B., and Fedorovich, E.: Observations of the early evening boundary-layer transition using a small unmanned aerial system, Boundary-Layer Meteorology, 146, 119–132, doi:10.1007/s10546-012-9760-3, 2013.

Brady, J. M., Stokes, M. D., Bonnardel, J., and Bertram, T. H.: Characterization of a quadrotor unmanned aircraft system for aerosol-particle-concentration measurements, Environmental Science & Technology, 50, 1376–1383, doi:10.1021/acs.est.5b05320, 2016.

Brenner, C., Thiem, C. E., Wizemann, H.-D., Bernhardt, M., and Schulz, K.: Estimating spatially distributed turbulent heat fluxes from high-resolution thermal imagery acquired with a UAV system, International Journal of Remote Sensing, 38, 3003–3026, doi:10.1080/01431161.2017.1280202, 2017.

Brenner, C., Zeeman, M., Bernhardt, M., and Schulz, K.: Estimation of evapotranspiration of temperate grassland based on high-resolution thermal and visible range imagery from unmanned aerial systems, International Journal of Remote Sensing, 0, 1–34, doi:10.1080/01431161.2018.1471550, 2018.

Brosy, C., Krampf, K., Zeeman, M., Wolf, B., Junkermann, W., Schäfer, K., Emeis, S., and Kunstmann, H.: Simultaneous multicopter-based air sampling and sensing of meteorological variables, Atmospheric Measurement Techniques, 10, 2773–2784, doi:10.5194/amt-10_2773-2017, 2017.

Brownlow, R., Lowry, D., Thomas, R. M., Fisher, R. E., France, J. L., Cain, M., Richardson, T. S., Greatwood, C., Freer, J., Pyle, J. A., MacKenzie, A. R., and Nisbet, E. G.: Methane mole fraction and δ13C above and below the trade wind inversion at Ascension Island in air sampled by aerial robotics, Geophysical Research Letters, 43, doi:10.1002/2016GL071155, 2016.

Brugger, P., Banerjee, T., De Roo, F., Kröniger, K., Qubaja, R., Rohatyn, S., Rotenberg, E., Tatarinov, F., Yakir, D., Yang, F., and Mauder, M.: Effect of Surface Heterogeneity on the Boundary-Layer Height: A Case Study at a Semi-Arid Forest, Boundary-Layer Meteorology, pp. 1–18, doi:10.1007/s10546-018-0371-5, 2018.

Brutsaert, W.: A theory for local evaporation (or heat transfer) from rough and smooth surfaces at ground level, Water Resources Research, 11, 543–550, 1975.

Calhoun, R., Heap, R., Princevac, M., Newsom, R., Fernando, H., and Ligon, D.: Virtual towers using coherent Doppler lidar during the Joint Urban 2003 dispersion experiment, Journal of Applied Meteorology and Climatology, 45, 1116–1126, doi:10.1175/JAM2391.1, 2006.

Chang, C.-C., Wang, J.-L., Chang, C.-Y., Liang, M.-C., and Lin, M.-R.: Development of a multicopter-carried whole air sampling apparatus and its applications in environmental studies, Chemosphere, 144, 484–492, 2016.

Chávez, J. L., Neale, C. M., Prueger, J. H., and Kustas, W. P.: Daily evapotranspiration estimates from extrapolating instantaneous airborne remote sensing ET values, Irrigation Science, 27, 67–81, 2008.

Choi, W., Faloona, I., McKay, M., Goldstein, A., and Baker, B.: Estimating the atmospheric boundary layer height over sloped, forested terrain from surface spectral analysis during BEARPEX, Atmospheric Chemistry and Physics, 11, 6837–6853, 2011.

Choularton, T., Gallagher, M., Bower, K., Fowler, D., Zahniser, M., Kaye, A., Monteith, J., and Harding, R.: Trace Gas Flux Measurements at the Landscape Scale Using Boundary-Layer Budgets [and Discussion], Philosophical Transactions of the Royal Society of London A: Mathematical, Physical and Engineering Sciences, 351, 357–369, 1995.

Ciais, P., Sabine, C., Bala, G., Bopp, L., Brovkin, V., Canadell, J., Chhabra, A., DeFries, R., Galloway, J., Heimann, M., et al.: Carbon and other biogeochemical cycles, in: Climate change 2013: the physical science basis. Contribution of Working Group I to the Fifth Assessment Report of the Intergovernmental Panel on Climate Change, pp. 465–570, 2013.

Corrigan, C. E., Roberts, G. C., Ramana, M. V., Kim, D., and Ramanathan, V.: Capturing vertical profiles of aerosols and black carbon over the Indian Ocean using autonomous unmanned aerial vehicles, Atmospheric Chemistry and Physics, 8, 737–747, 2008.

Culf, A. D., Fisch, G., Malhi, Y., Costa, R. C., Nobre, A. D., Marques Filho, A. D. O., Gash, J. H., and Grace, J.: Carbon dioxide measurements in the nocturnal boundary layer over Amazonian forest, Hydrology and Earth System Sciences Discussions, European Geosciences Union, 3, 39–53, 1999.

Cuxart, J., Wrenger, B., Martínez-Villagrasa, D., Reuder, J., Jonassen, M. O., Jiménez, M. A., Lothon, M., Lohou, F., Hartogensis, O., Dünnermann, J., Conangla, L., and Garai, A.: Estimation of the advection effects induced by surface heterogeneities in the surface energy budget, Atmospheric Chemistry and Physics, 16, 9489–9504, doi:10.5194/acp-16-9489-2016, 2016.

Dämmgen, U., Rösemann, C., Haenel, H.-D., and Hutchings, N. J.: Enteric methane emissions from German dairy cows, Landbauforschung - vTI Agriculture and Forestry Research, 62, 21–31, 2012.

Davis, K. J., Bakwin, P. S., Yi, C., Berger, B. W., Zhao, C., Teclaw, R. M., and Isebrands, J.: The annual cycles of CO2 and H2O exchange over a northern mixed forest as observed from a very tall tower, Global Change Biology, 9, 1278–1293, 2003.

de Boer, G., Palo, S., Argrow, B., LoDolce, G., Mack, J., Gao, R.-S., Telg, H., Trussel, C., Fromm, J., Long, C. N., Bland, G., Maslanik, J., Schmid, B., and Hock, T.: The Pilatus unmanned aircraft system for lower atmospheric research, Atmospheric Measurement Techniques, 9, 1845–1857, doi:10.5194/amt-9-1845-2016, 2016.

Dean, J. F., Middelburg, J. J., Röckmann, T., Aerts, R., Blauw, L. G., Egger, M., Jetten, M. S. M., de Jong, A. E. E., Meisel, O. H., Rasigraf, O., Slomp, C. P., in't Zandt, M. H., and Dolman, A. J.: Methane Feedbacks to the Global Climate System in a Warmer World, Reviews of Geophysics, 56, 207–250, doi:10.1002/2017RG000559, 2018.

Denmead, O., Raupach, M., Dunin, F., Cleugh, H., and Leuning, R.: Boundary layer budgets for regional estimates of scalar fluxes, Global Change Biology, 2, 255–264, 1996.

Denmead, O., Leuning, R., Griffith, D., Jamie, I., Esler, M., Harper, L., and Freney, J.: Verifying inventory predictions of animal methane emissions with meteorological measurements, Boundary-Layer Meteorology, 96, 187–209, 2000.

Dlugokencky, E. J., Nisbet, E. G., Fisher, R., and Lowry, D.: Global atmospheric methane: budget, changes and dangers, Philosophical Transactions of the Royal Society of London A: Mathematical, Physical and Engineering Sciences, 369, 2058–2072, 2011.

Draxler, R. R. and Hess, G. D.: An overview of the HYSPLIT_4 modelling system for trajectories, Australian Meteorological Magazine, 47, 295–308, 1998.

Durre, I., Vose, R. S., and Wuertz, D. B.: Overview of the integrated global radiosonde archive, Journal of Climate, 19, 53–68, doi:10.1175/JCLI3594.1, 2006.

Emeis, S.: Examples for the determination of turbulent (sub-synoptic) fluxes with inverse methods, Meteorologische Zeitschrift, 17, 3–11, 2008.

Emeis, S., Schäfer, K., and Münkel, C.: Observation of the structure of the urban boundary layer with different ceilometers and validation by RASS data, Meteorologische Zeitschrift, 18, 149–154, 2009.

Emeis, S., Schäfer, K., Münkel, C., Friedl, R., and Suppan, P.: Evaluation of the Interpretation of Ceilometer Data with RASS and Radiosonde Data, Boundary-Layer Meteorology, 143, 25–35, 2012.

Finnigan, J. J., Clement, R., Malhi, Y., Leuning, R., and Cleugh, H. A.: A Re-Evaluation of Long-Term Flux Measurement Techniques Part I: Averaging and Coordinate Rotation, Boundary-Layer Meteorology, 107, 1–48, doi:10.1023/A:1021554900225, 2003.

Foken, T.: Micrometeorology, Springer-Verlag Berlin Heidelberg, 2. edn., 2008.

Foken, T.: Angewandte Meteorologie – Mikrometeorologische Methoden, Springer-Verlag Berlin Heidelberg, 2016.

Foken, T. and Leclerc, M.: Methods and limitations in validation of footprint models, Agricultural and Forest Meteorology, 127, 223–234, 2004.

Freney, E. J., Sellegri, K., Canonaco, F., Colomb, A., Borbon, A., Michoud, V., Doussin, J.-F., Crumeyrolle, S., Amarouche, N., Pichon, J.-M., Bourianne, T., Gomes, L., Prevot, A. S. H., Beekmann, M., and Schwarzenböeck, A.: Characterizing the impact of urban emissions on regional aerosol particles: airborne measurements during the MEGAPOLI experiment, Atmospheric Chemistry and Physics, 14, 1397–1412, doi:10.5194/acp-14-1397-2014, 2014.

Gillespie, A.: Land Surface Temperature, pp. 314–319, Springer New York, doi:10.1007/978-0-387-36699-9_79, 2014.

Glazunov, A., Rannik, Ü., Stepanenko, V., Lykosov, V., Auvinen, M., Vesala, T., and Mammarella, I.: Large-eddy simulation and stochastic modeling

of Lagrangian particles for footprint determination in the stable boundary layer, Geoscientific Model Development, 9, 2925–2949, 2016.

Göckede, M., Rebmann, C., and Foken, T.: A combination of quality assessment tools for eddy covariance measurements with footprint modelling for the characterisation of complex sites, Agricultural and Forest Meteorology, 127, 175–188, 2004.

Golston, L. M., Tao, L., Brosy, C., Schäfer, K., Wolf, B., McSpiritt, J., Buchholz, B., Caulton, D. R., Pan, D., Zondlo, M. A., Yoel, D., Kunstmann, H., and McGregor, M.: Lightweight mid-infrared methane sensor for unmanned aerial systems, Applied Physics B, 123, 170, doi:10.1007/s00340-0176734-6, 2017.

Graf, M., Kossmann, M., Trusilova, K., and Mühlbacher, G.: Identification and Climatology of Alpine Pumping from a Regional Climate Simulation, Frontiers in Earth Science, 4, 5, doi:10.3389/feart.2016.00005, 2016.

Greatwood, C., Richardson, T. S., Freer, J., Thomas, R. M., MacKenzie, A. R., Brownlow, R., Lowry, D., Fisher, R. E., and Nisbet, E. G.: Atmospheric Sampling on Ascension Island Using Multirotor UAVs, Sensors, 17, 1189, doi:10.3390/s17061189, 2017.

Guzinski, R., Anderson, M. C., Kustas, W. P., Nieto, H., and Sandholt, I.: Using a thermal-based two source energy balance model with time-differencing to estimate surface energy fluxes with day–night MODIS observations, Hydrology and Earth System Sciences, 17, 2809–2825, doi:10.5194/hess-17-2809-2013, 2013.

Ha, K.-J. and Mahrt, L.: Radiative and turbulent fluxes in the nocturnal boundary layer, Tellus A, 55, 317–327, doi:10.1034/j.1600-0870.2003.00031.x, 2003.

Hacker, J. M., Chen, D., Bai, M., Ewenz, C., Junkermann, W., Lieff, W., McManus, B., Neininger, B., Sun, J., Coates, T., et al.: Using airborne technology to quantify and apportion emissions of CH4 and NH3 from feedlots, Animal Production Science, 56, 190–203, doi:10.1071/AN15513, 2016.

Hammann, E., Behrendt, A., Le Mounier, F., and Wulfmeyer, V.: Temperature profiling of the atmospheric boundary layer with rotational Raman lidar during the HD(CP)2 Observational Prototype Experiment, Atmospheric Chemistry and Physics, 15, 2867–2881, 2015.

Harper, L., Denmead, O., and Flesch, T.: Micrometeorological techniques for measurement of enteric greenhouse gas emissions, Animal Feed Science and Technology, 166, 227–239, 2011.

Hatfield, J., Perrier, A., and Jackson, R.: Estimation of evapotranspiration at one time-of-day using remotely sensed surface temperatures, Agricultural Water Management, 7, 341–350, 1983.

Hausmann, P., Sussmann, R., and Smale, D.: Contribution of oil and natural gas production to renewed increase in atmospheric methane (2007–2014): top–down estimate from ethane and methane column observations, Atmospheric Chemistry and Physics, 16, 3227–3244, 2016.

Heidbach, K., Schmid, H. P., and Mauder, M.: Experimental evaluation of flux footprint models, Agricultural and Forest Meteorology, 246, 142–153, 2017.

Hennemuth, B. and Lammert, A.: Determination of the Atmospheric Boundary Layer Height from Radiosonde and Lidar Backscatter, Boundary-Layer Meteorology, 120, 181–200, doi:10.1007/s10546-005-9035-3, 2006.

Hoffmann, H., Nieto, H., Jensen, R., Guzinski, R., Zarco-Tejada, P., and Friborg, T.: Estimating evaporation with thermal UAV data and two-source energy balance models, Hydrology and Earth System Sciences, 20, 697–713, 2016.

Holland, G. J., McGeer, T., and Youngren, H.: Autonomous aerosondes for economical atmospheric soundings anywhere on the globe, Bulletin of the American Meteorological Society, 73, 1987–1998, 1992.

Idso, S. B., Jackson, R. D., and Reginato, R. J.: Estimating Evaporation: A Technique Adaptable to Remote Sensing, Science, 189, 991–992, doi:10.1126/science.189.4207.991, 1975.

Inoue, J., Curry, J. A., and Maslanik, J. A.: Application of Aerosondes to melt-pond observations over Arctic sea ice, Journal of Atmospheric and Oceanic technology, 25, 327–334, 2008.

IPCC: 2006 IPCC guidelines for national greenhouse gas inventories, chap. 10, URL `http://www.ipcc-nggip.iges.or.jp/public/2006gl/pdf/4_Volume4/V4_10_Ch10_Livestock.pdf`, 2006.

Jackson, R. D.: Evaluating evapotranspiration at local and regional scales, Proceedings of the IEEE, 73, 1086–1096, 1985.

Jackson, R. D., Reginato, R. J., and Idso, S. B.: Wheat canopy temperature: a practical tool for evaluating water requirements, Water resources research, 13, 651–656, 1977.

Junkermann, W.: An ultralight aircraft as platform for research in the lower troposphere: system performance and first results from radiation transfer studies in stratiform aerosol layers and broken cloud conditions, Journal of Atmospheric and Oceanic Technology, 18, 934–946, 2001.

Kalma, J. D., McVicar, T. R., and McCabe, M. F.: Estimating land surface evaporation: A review of methods using remotely sensed surface temperature data, Surveys in Geophysics, 29, 421–469, 2008.

Keeling, C. D.: Rewards and penalties of monitoring the Earth, Annual Review of Energy and the Environment, 23, 25–82, 1998.

Khan, A., Schaefer, D., Tao, L., Miller, D. J., Sun, K., Zondlo, M. A., Harrison, W. A., Roscoe, B., and Lary, D. J.: Low power greenhouse gas sensors for unmanned aerial vehicles, Remote Sensing, 4, 1355–1368, 2012.

Kirschke, S., Bousquet, P., Ciais, P., Saunois, M., Canadell, J. G., Dlugokencky, E. J., Bergamaschi, P., Bergmann, D., Blake, D. R., Bruhwiler, L., et al.: Three decades of global methane sources and sinks, Nature Geoscience, 6, 813–823, 2013.

Kljun, N., Rotach, M. W., and Schmid, H. P.: A Three-Dimensional Backward Lagrangian Footprint Model For A Wide Range Of Boundary-Layer Stratifications, Boundary-Layer Meteorology, 103, 205–226, doi:10.1023/A:1014556300021, 2002.

Kljun, N., Calanca, P., Rotach, M. W., and Schmid, H. P.: A simple two-dimensional parameterisation for Flux Footprint Prediction (FFP), Geoscientific Model Development, 8, 3695–3713, doi:10.5194/gmd-8-3695-2015, 2015.

Konrad, T., Hill, M., Rowland, J., and Meyer, J.: A small, radio-controlled aircraft as a platform for meteorological sensors, Appl. Phys. Lab. Tech. Digest, 10, 11–19, 1970.

Korhonen, K., Giannakaki, E., Mielonen, T., Pfüller, A., Laakso, L., Vakkari, V., Baars, H., Engelmann, R., Beukes, J. P., Van Zyl, P. G., Ramandh, A., Ntsangwane, L., Josipovic, M., Tiitta, P., Fourie, G., Ngwana, I., Chiloane, K., and Komppula, M.: Atmospheric boundary layer top height in

South Africa: measurements with lidar and radiosonde compared to three atmospheric models, Atmospheric Chemistry and Physics, 14, 4263–4278, doi:10.5194/acp-14-4263-2014, 2014.

Kottek, M., Grieser, J., Beck, C., Rudolf, B., and Rubel, F.: World map of the Köppen-Geiger climate classification updated, Meteorologische Zeitschrift, 15, 259–263, 2006.

Kotthaus, S., Halios, C. H., Barlow, J. F., and Grimmond, C. S. B.: Volume for pollution dispersion: London's atmospheric boundary layer during ClearfLo observed with two ground-based lidar types, Atmospheric Environment, accepted, 2018.

Krampf, K.: Windmessungen mit unbemannten Flugobjekten anhand von Daten der internen Lageregelung am Beispiel eines Hexacopters – Machbarkeitsstudie und Untersuchung der atmosphärischen Grenzschicht, Masterarbeit, Ruprecht-Karls Universität Heidelberg, 2017.

Kraus, H.: Die Atmosphäre der Erde – Eine Einführung in die Meteorologie, Springer-Verlag Berlin Heidelberg, 2004.

Kunstmann, H., Schneider, K., Forkel, R., and Knoche, R.: Impact analysis of climate change for an Alpine catchment using high resolution dynamic downscaling of ECHAM4 time slices, Hydrology and Earth System Sciences Discussions, 8, 1031–1045, 2004.

Kunstmann, H., Krause, J., and Mayr, S.: Inverse distributed hydrological modelling of Alpine catchments, Hydrology and Earth System Sciences Discussions, 10, 395–412, 2006.

Kunz, M., Lavric, J. V., Gerbig, C., Tans, P., Neff, D., Hummelgård, C., Martin, H., Rödjegård, H., Wrenger, B., and Heimann, M.: COCAP: a carbon dioxide analyser for small unmanned aircraft systems, Atmospheric Measurement Techniques, 11, 1833–1849, doi:10.5194/amt-11-1833-2018, 2018.

Kustas, W. and Norman, J.: Use of remote sensing for evapotranspiration monitoring over land surfaces, Hydrological Sciences Journal, 41, 495–516, 1996.

Kustas, W. P. and Daughtry, C. S. T.: Estimation of the soil heat flux/net radiation ratio from spectral data, Agricultural and Forest Meteorology, 49, 205–223, 1990.

Kustas, W. P., Choudhury, B. J., Moran, M. S., Reginato, R. J., Jackson, R. D., Gay, L. W., and Weaver, H. L.: Determination of sensible heat flux over sparse canopy using thermal infrared data, Agricultural and Forest Meteorology, 44, 197–216, 1989.

Kustas, W. P., Alfieri, J. G., Anderson, M. C., Colaizzi, P. D., Prueger, J. H., Evett, S. R., Neale, C. M., French, A. N., Hipps, L. E., Chávez, J. L., Copeland, K. S., and Howell, T. A.: Evaluating the two-source energy balance model using local thermal and surface flux observations in a strongly advective irrigated agricultural area, Advances in Water Resources, 50, 120–133, doi:10.1016/j.advwatres.2012.07.005, 2012.

Li, Z.-L., Tang, R., Wan, Z., Bi, Y., Zhou, C., Tang, B., Yan, G., and Zhang, X.: A review of current methodologies for regional evapotranspiration estimation from remotely sensed data, Sensors, 9, 3801–3853, 2009.

Li, Z.-L., Tang, B.-H., Wu, H., Ren, H., Yan, G., Wan, Z., Trigo, I. F., and Sobrino, J. A.: Satellite-derived land surface temperature: Current status and perspectives, Remote Sensing of Environment, 131, 14–37, doi:10.1016/j.rse.2012.12.008, 2013.

Liu, H. and Foken, T.: A modified Bowen ratio method to determine sensible and latent heat fluxes, Meteorologische Zeitschrift, 10, 71–80, doi:10.1127/0941-2948/2001/0010-0071, 2001.

Liu, W., Hong, Y., Khan, S. I., Huang, M., Vieux, B., Caliskan, S., and Grout, T.: Actual evapotranspiration estimation for different land use and land cover in urban regions using Landsat 5 data, Journal of Applied Remote Sensing, 4, 041 873–041 873, doi:10.1117/1.3525566, 2010.

Lugauer, M. and Winkler, P.: Thermal circulation in South Bavaria–climatology and synoptic aspects, Meteorologische Zeitschrift, 14, 15–30, 2005.

Mahrt, L.: Surface heterogeneity and vertical structure of the boundary layer, Boundary-Layer Meteorology, 96, 33–62, doi:10.1023/A:1002482332477, 2000.

Martin, S., Bange, J., and Beyrich, F.: Meteorological profiling of the lower troposphere using the research UAV "M2AV Carolo", Atmospheric Measurement Techniques, 4, 705–716, 2011.

Marx, A., Kunstmann, H., Schüttemeyer, D., and Moene, A.: Uncertainty analysis for satellite derived sensible heat fluxes and scintillometer measurements over Savannah environment and comparison to mesoscale meteorological simulation results, Agricultural and Forest Meteorology, 148, 656–667, 2008.

Mateling, M. E., Lazzara, M. A., Keller, L. M., Weidner, G. A., and Cassano, J. J.: Alexander Tall Tower! A Study of the Boundary Layer on the Ross Ice Shelf, Antarctica, Journal of Applied Meteorology and Climatology, 57, 421–434, doi:10.1175/JAMC-D-17-0017.1, 2018.

Mathieu, N., Strachan, I., Leclerc, M., Karipot, A., and Pattey, E.: Role of low-level jets and boundary-layer properties on the NBL budget technique, Agricultural and Forest Meteorology, 135, 35–43, doi:10.1016/j.agrformet.2005.10.001, 2005.

Mauder, M., Cuntz, M., Drüe, C., Graf, A., Rebmann, C., Schmid, H. P., Schmidt, M., and Steinbrecher, R.: A strategy for quality and uncertainty assessment of long-term eddy-covariance measurements, Agricultural and Forest Meteorology, 169, 122–135, 2013.

McCabe, M. F. and Wood, E. F.: Scale influences on the remote estimation of evapotranspiration using multiple satellite sensors, Remote Sensing of Environment, 105, 271–285, 2006.

McGeer, T. and Holland, G.: Small autonomous aircraft for economical oceanographic observations on a wide scale, Oceanography, 6, 129–135, 1993.

McPherson, R. A.: A review of vegetation—atmosphere interactions and their influences on mesoscale phenomena, Progress in Physical Geography, 31, 261–285, 2007.

Metzger, S., Junkermann, W., Mauder, M., Beyrich, F., Butterbach-Bahl, K., Schmid, H. P., and Foken, T.: Eddy-covariance flux measurements with a weight-shift microlight aircraft, Atmospheric Measurement Techniques, 5, 1699, 2012.

Metzger, S., Junkermann, W., Mauder, M., Butterbach-Bahl, K., y Widemann, B. T., Neidl, F., Schäfer, K., Wieneke, S., Zheng, X., Schmid, H. P., and Foken, T.: Spatially explicit regionalization of airborne flux measurements using environmental response functions, Biogeosciences, 10, 2193, 2013.

Mikhailov, E. F., Mironova, S., Mironov, G., Vlasenko, S., Panov, A., Chi, X., Walter, D., Carbone, S., Artaxo, P., Heimann, M., Lavric, J., Pöschl, U., and Andreae, M. O.: Long-term measurements (2010–2014) of carbonaceous aerosol and carbon monoxide at the Zotino Tall Tower Observatory (ZOTTO) in central Siberia, Atmospheric Chemistry and Physics, 17, 14 365–14 392, doi:10.5194/acp-17-14365-2017, 2017.

Miles, N. L., Richardson, S. J., Davis, K. J., Lauvaux, T., Andrews, A. E., West, T. O., Bandaru, V., and Crosson, E. R.: Large amplitude spatial and temporal gradients in atmospheric boundary layer CO2mole fractions detected with a tower-based network in the US upper Midwest, Journal of Geophysical Research: Biogeosciences, 117, doi:10.1029/2011JG001781, 2012.

Mitchell, J. F. B., Johns, T. C., Gregory, J. M., and Tett, S. F. B.: Climate response to increasing levels of greenhouse gases and sulphate aerosols, Nature, 376, 501–504, 1995.

Mitchell, J. F. B., Karoly, D. J., Hegerl, G. C., Zwiers, F. W., Allen, M. R., Marengo, J., et al.: Detection of Climate Change and Attribution of Causes, in: Climate change 2001: the physical science basis. Contribution of Working Group I to the Third Assessment Report of the Intergovernmental Panel on Climate Change, p. 881, 2001.

Morillas, L., García, M., Nieto, H., Villagarcia, L., Sandholt, I., Gonzalez-Dugo, M., Zarco-Tejada, P., and Domingo, F.: Using radiometric surface temperature for surface energy flux estimation in Mediterranean drylands from a two-source perspective, Remote sensing of environment, 136, 234–246, 2013.

Muller, C. L., Chapman, L., Grimmond, C. S. B., Young, D. T., and Cai, X.: Sensors and the city: a review of urban meteorological networks, International Journal of Climatology, 33, 1585–1600, doi:10.1002/joc.3678, 2013.

Münkel, C.: Mixing height determination with lidar ceilometers - Results from Helsinki Testbed, Meteorologische Zeitschrift, 16, 451–459, doi:10.1127/0941-2948/2007/0221, 2007.

Nathan, B. J., Golston, L. M., O'Brien, A. S., Ross, K., Harrison, W. A., Tao, L., Lary, D. J., Johnson, D. R., Covington, A. N., Clark, N. N., and Zondlo, M. A.: Near-field characterization of methane emission variability

from a compressor station using a model aircraft, Environmental Science & Technology, 49, 7896–7903, doi:10.1021/acs.est.5b00705, 2015.

Neumann, P. P. and Bartholmai, M.: Real-time wind estimation on a micro unmanned aerial vehicle using its inertial measurement unit, Sensors and Actuators A: Physical, 235, 300–310, 2015.

Nisbet, E.: Earth monitoring: Cinderella science, Nature, 450, 789–790, 2007.

Nisbet, E. and Weiss, R.: Top-down versus bottom-up, Science, 328, 1241–1243, 2010.

Nisbet, E. G., Dlugokencky, E. J., and Bousquet, P.: Methane on the rise – again, Science, 343, 493–495, 2014.

Norman, J. M. and Becker, F.: Terminology in thermal infrared remote sensing of natural surfaces, Remote Sensing Reviews, 12, 159–173, 1995.

Oke, T. R.: Boundary Layer Climates, Routledge, 1987.

Ortega-Farías, S., Ortega-Salazar, S., Poblete, T., Kilic, A., Allen, R., Poblete-Echeverría, C., Ahumada-Orellana, L., Zuñiga, M., and Sepúlveda, D.: Estimation of energy balance components over a drip-irrigated olive orchard using thermal and multispectral cameras placed on a helicopter-based unmanned aerial vehicle (UAV), Remote Sensing, 8, 638, 2016.

Palomaki, R. T., Rose, N. T., van den Bossche, M., Sherman, T. J., and De Wekker, S. F.: Wind estimation in the lower atmosphere using multi-rotor aircraft, Journal of Atmospheric and Oceanic Technology, 34(5), 1183–1191, doi:10.1175/JTECH-D-16-0177.1, 2017.

Papoulis, A.: Probability Random Variables and Stochastic Processes, McGraw-Hill, New York, 1984.

Pasquill, F.: Some aspects of boundary layer description, Quarterly Journal of the Royal Meteorological Society, 98, 469–494, 1972.

Pattey, E., Strachan, I. B., Desjardins, R. L., and Massheder, J.: Measuring nighttime CO2 flux over terrestrial ecosystems using eddy covariance and nocturnal boundary layer methods, Agricultural and Forest Meteorology, 113, 145–158, 2002.

Pattey, E., Strachan, I. B., Desjardins, R. L., Edwards, G. C., Dow, D., and MacPherson, J. I.: Application of a tunable diode laser to the measurement

of CH4 and N2O fluxes from field to landscape scale using several micrometeorological techniques, Agricultural and Forest Meteorology, 136, 222–236, 2006.

Pillai, D., Gerbig, C., Ahmadov, R., Rödenbeck, C., Kretschmer, R., Koch, T., Thompson, R., Neininger, B., and Lavrié, J.: High-resolution simulations of atmospheric CO 2 over complex terrain–representing the Ochsenkopf mountain tall tower, Atmospheric Chemistry and Physics, 11, 7445–7464, doi:10.5194/acp-11-7445-2011, 2011.

Price, J. C.: The potential of remotely sensed thermal infrared data to infer surface soil moisture and evaporation, Water Resources Research, 16, 787–795, 1980.

Rango, A.: Application of remote sensing methods to hydrology and water resources, Hydrological Sciences Journal, 39, 309–320, 1994.

Rango, A., Laliberte, A., Herrick, J. E., Winters, C., Havstad, K., Steele, C., and Browning, D.: Unmanned aerial vehicle-based remote sensing for rangeland assessment, monitoring, and management, Journal of Applied Remote Sensing, 3, 033 542–033 542, 2009.

Reid, W. V., Bréchignac, C., and Lee, Y. T.: Earth system research priorities, Science, 325, 245–245, 2009.

Reuder, J., Brisset, P., Jonassen, M., Müller, M., and Mayer, S.: The Small Unmanned Meteorological Observer SUMO: A new tool for atmospheric boundary layer research, Meteorologische Zeitschrift, 18, 141–147, 2009.

Reuder, J., Båserud, L., Jonassen, M. O., Kral, S. T., and Müller, M.: Exploring the potential of the RPA system SUMO for multipurpose boundary-layer missions during the BLLAST campaign, Atmospheric Measurement Techniques, 9, 2675–2688, doi:10.5194/amt-9-2675-2016, 2016.

Roedel, W. and Wagner, T.: Physik unserer Umwelt: Die Atmosphäre, Springer, Berlin Heidelberg, 4. edn., 2011.

Santer, B. D., Wigley, T. M. L., and Jones, P. D.: Correlation methods in fingerprint detection studies, Climate Dynamics, 8, 265–276, doi:10.1007/BF00209666, 1993.

Sasakawa, M., Shimoyama, K., Machida, T., Tsuda, N., Suto, H., Arshinov, M., Davydov, D., Fofonov, A., Krasnov, O., Saeki, T., Koyama, Y., and

Maksyutov, S.: Continuous measurements of methane from a tower network over Siberia, Tellus B, 62, 403–416, 2010.

Saunois, M., Jackson, R., Bousquet, P., Poulter, B., and Canadell, J.: The growing role of methane in anthropogenic climate change, Environmental Research Letters, 11, 120 207, 2016.

Schäfer, K., Emeis, S., Hoffmann, H., and Jahn, C.: Influence of mixing layer height upon air pollution in urban and sub-urban areas, Meteorologische Zeitschrift, 15, 647–658, doi:10.1127/0941-2948/2006/0164, 2006.

Schäfer, K., Zeeman, M., Brosy, C., Münkel, C., Fersch, B., Mauder, M., and Emeis, S.: Methane distributions and transports in the nocturnal boundary layer at a rural station, in: SPIE Remote Sensing, pp. 1000 103–1000 103, International Society for Optics and Photonics, 2016.

Schmid, H. P.: Source areas for scalars and scalar fluxes, Boundary-Layer Meteorology, 67, 293–318, 1994.

Schmid, H. P.: Experimental design for flux measurements: matching scales of observations and fluxes, Agricultural and Forest Meteorology, 87, 179–200, 1997.

Schmid, H. P.: Footprint modeling for vegetation atmosphere exchange studies: a review and perspective, Agricultural and Forest Meteorology, 113, 159–183, 2002.

Schönwiese, C.: Klimatologie, UTB Stuttgart, 3. edn., 2008.

Seibert, P., Beyrich, F., Gryning, S.-E., Joffre, S., Rasmussen, A., and Tercier, P.: Review and intercomparison of operational methods for the determination of the mixing height, Atmospheric Environment, 34, 1001–1027, 2000.

Seidel, D. J., Ao, C. O., and Li, K.: Estimating climatological planetary boundary layer heights from radiosonde observations: Comparison of methods and uncertainty analysis, Journal of Geophysical Research: Atmospheres, 115, doi:10.1029/2009JD013680, 2010.

Seidel, J., Ketzler, G., Bechtel, B., Thies, B., Philipp, A., Böhner, J., Egli, S., Eisele, M., Herma, F., Langkamp, T., Petersen, E., Sachsen, T., Schlabing, D., and Schneider, C.: Mobile measurement techniques for local and micro-scale studies in urban and topo-climatology, DIE ERDE–Journal of the Geographical Society of Berlin, 147, 15–39, 2016.

Soddell, J. R., McGuffie, K., and Holland, G. J.: Intercomparison of atmospheric soundings from the aerosonde and radiosonde, Journal of Applied Meteorology, 43, 1260–1269, 2004.

Soltani, M., Mauder, M., Laux, P., and Kunstmann, H.: Turbulent flux variability and energy balance closure in the TERENO prealpine observatory: a hydrometeorological data analysis, Theoretical and Applied Climatology, pp. 1–20, doi:10.1007/s00704-017-2235-1, 2017.

Stein, A., Draxler, R. R., Rolph, G. D., Stunder, B. J., Cohen, M., and Ngan, F.: NOAA's HYSPLIT atmospheric transport and dispersion modeling system, Bulletin of the American Meteorological Society, 96, 2059–2077, 2015.

Stephens, G. L., Miller, S. D., Benedetti, A., McCoy, R. B., McCoy Jr, R. F., Ellingson, R. G., Vitko Jr, J., Bolton, W., Tooman, T. P., Valero, F. P. J., Minnis, P., Pilewskie, P., Phipps, G. S., Sekelsky, S., Carswell, J. R., Miller, S. D., Benedetti, A., McCoy, R. B., McCoy Jr., R. F., Lederbuhr, A., and Bambhaj, R.: The Department of Energy's atmospheric radiation measurement (ARM) unmanned aerospace vehicle (UAV) program, Bulletin of the American Meteorological Society, 81, 2915–2938, 2000.

Stieger, J., Bamberger, I., Buchmann, N., and Eugster, W.: Validation of farm-scale methane emissions using nocturnal boundary layer budgets, Atmospheric Chemistry and Physics, 15, 14 055–14 069, 2015.

Stull, R.: An Introduction to Boundary Layer Meteorology, Dordrecht, 9. edn., 1988.

Tan, J., Yang, L., Grimmond, C. S. B., Shi, J., Gu, W., Chang, Y., Hu, P., Sun, J., Ao, X., and Han, Z.: Urban integrated meteorological observations: practice and experience in Shanghai, China, Bulletin of the American Meteorological Society, 96, 85–102, doi:10.1175/BAMS-D-13-00216.1, 2015.

Thom, A. S. .: Momentum, mass and heat exchange of vegetation, Quarterly Journal of the Royal Meteorological Society, 98, 124–134, 1972.

Tian, P., Cao, X., Zhang, L., Sun, N., Sun, L., Logan, T., Shi, J., Wang, Y., Ji, Y., Lin, Y., et al.: Aerosol vertical distribution and optical properties over China from long-term satellite and ground-based remote sensing, Atmospheric Chemistry and Physics, 17, 2509–2523, doi:10.5194/acp-17-2509-2017, 2017.

Turner, D., Lucieer, A., Malenovskỳ, Z., King, D. H., and Robinson, S. A.: Spatial co-registration of ultra-high resolution visible, multispectral and thermal images acquired with a micro-UAV over Antarctic moss beds, Remote Sensing, 6, 4003–4024, 2014.

Twine, T. E., Kustas, W., Norman, J., Cook, D., Houser, P., Meyers, T., Prueger, J., Starks, P., and Wesely, M.: Correcting eddy-covariance flux underestimates over a grassland, Agricultural and Forest Meteorology, 103, 279–300, 2000.

UBA: Beitrag der Landwirtschaft zu den Treibhausgas-Emissionen, access: 11.07.2017, URL `https://www.umweltbundesamt.de/daten/land-forstwirtschaft/landwirtschaft/beitrag-der-landwirtschaft-zu-den-treibhausgas#textpart-1`, 2017a.

UBA: Struktur der Flächennutzung, access: 11.07.2017, URL `https://www.umweltbundesamt.de/daten/flaechennutzung/struktur-der-flaechennutzung#textpart-1`, 2017b.

Velasco, E., Márquez, C., Bueno, E., Bernabé, R., Sánchez, A., Fentanes, O., Wöhrnschimmel, H., Cárdenas, B., Kamilla, A., Wakamatsu, S., and Molina, L. T.: Vertical distribution of ozone and VOCs in the low boundary layer of Mexico City, Atmospheric Chemistry and Physics, 8, 3061–3079, 2008.

Vesala, T., Kljun, N., Rannik, Ü., Rinne, J., Sogachev, A., Markkanen, T., Sabelfeld, K., Foken, T., and Leclerc, M.: Flux and concentration footprint modelling: State of the art, Environmental Pollution, 152, 653–666, 2008.

Villa, T. F., Gonzalez, F., Miljievic, B., Ristovski, Z. D., and Morawska, L.: An Overview of Small Unmanned Aerial Vehicles for Air Quality Measurements: Present Applications and Future Prospectives, Sensors, 16, 1072, 2016.

Wallace, J. and Hobbs, P.: Atmospheric Science – An Introductory Survey, Burlington San Diego London, 2. edn., 2006.

Watts, A. C., Ambrosia, V. G., and Hinkley, E. A.: Unmanned aircraft systems in remote sensing and scientific research: Classification and considerations of use, Remote Sensing, 4, 1671–1692, 2012.

Werth, D., Buckley, R., Zhang, G., Kurzeja, R., Leclerc, M., Duarte, H., Parker, M., and Watson, T.: Quantifying the local influence at a tall tower site in nocturnal conditions, Theoretical and applied climatology, 127, 627–642, 2017.

Wiegner, M., Emeis, S., Freudenthaler, V., Heese, B., Junkermann, W., Münkel, C., Schäfer, K., Seefeldner, M., and Vogt, S.: Mixing layer height over Munich, Germany: Variability and comparisons of different methodologies, Journal of Geophysical Research: Atmospheres, 111, doi:10.1029/2005JD006593, 2006.

Wildmann, N., Kaufmann, F., and Bange, J.: An inverse-modelling approach for frequency response correction of capacitive humidity sensors in ABL research with small remotely piloted aircraft (RPA), Atmospheric Measurement Techniques, 7, 3059–3069, 2014.

Wittebol, L.: Refinement of the nocturnal boundary layer budget method for quantifying agricultural greenhouse gas emissions, McGill University, 2009.

Wolf, B., Chwala, C., Fersch, B., Garvelmann, J., Junkermann, W., Zeeman, M., Angerer, A., Adler, B., Beck, C., B. C., Brugger, P., Emeis, S., Dannenmann, M., De Roo, F., Diaz-Pines, E., Haas, E., Hagen, M., Hajnsek, I., Jacobeit, J., Jagdhuber, T., Kalthoff, N., Kiese, R., Kunstmann, H., Kosak, O., Krieg, R., Malchow, C., Mauder, M., Merz, R., Notarnicola, C., Philipp, A., Reif, W., Reineke, S., Rödiger, T., Ruehr, N., Schäfer, K., Schrön, M., Senatore, A., Shupe, H., Völksch., I., Wanninger, C., Zacharias, S., and Schmid, H. P.: The ScaleX campaign: scale-crossing land-surface and boundary layer processes in the TERENO-preAlpine observatory, Bulletin of the American Meteorological Society, 98(6), 1217–1234, doi:10.1175/BAMS-D-15-00277.1, 2017.

Yang, Y., Qiu, J., Su, H., Bai, Q., Liu, S., Li, L., Yu, Y., and Huang, Y.: A One-Source Approach for Estimating Land Surface Heat Fluxes Using Remotely Sensed Land Surface Temperature, Remote Sensing, 9, 43, 2017.

Zacharias, S., Bogena, H., Samaniego, L., Mauder, M., Fuß, R., Pütz, T., Frenzel, M., Schwank, M., Baessler, C., Butterbach-Bahl, K., Bens, O., Borg, E., Brauer, A., Dietrich, P., Hajnsek, I., Helle, G., Kiese, R., Kunstmann, H., Klotz, S., Munch, J. C., Papen, H., Priesack, E., Schmid, H. P., Steinbrecher, R., Rosenbaum, U., Teutsch, G., , and Vereecken, H.: A network of terrestrial environmental observatories in Germany, Vadose Zone Journal, 10, 955–973, doi:10.2136/vzj2010.0139, 2011.

Zeeman, M. J., Mauder, M., Steinbrecher, R., Heidbach, K., Eckart, E., and Schmid, H. P.: Reduced snow cover affects productivity of upland temperate grasslands, Agricultural and Forest Meteorology, 232, 514–526, 2017.

Appendix

A1 Hexacopter Hardware

Tab. A1: Electronic parts with company including the hexacopters, autopilot and flight control sensors as well as measurement sensors.

Parts	**Company**
Hexacopter F550 Flame Wheel	DJI Innovations, Shenzhen, China
Hexacopter Pro X-3	Stein Elektronik, Jülich, Germany
Pixhawk	3DR, Berkeley, USA
GPS LEA-6	u-blox, Thalwil, Switzerland
MS5611-01BA03 (pressure sensor)	Measurement Specialties, Hampton, VA, USA
Telemetry Radio v2	3DR, Berkeley, USA
Remote control mx-16 HoTT	Graupner/SJ GmbH, Kirchheim unter Teck, Germany
LiPo battery, 4S, 5000 mAh	SLS XTRON, Althegnenberg, Germany
LiPo battery, 4S, 10000 mAh	SLS XTRON, Althegnenberg, Germany
Graupner E-PROPS 9x5	Graupner/SJ GmbH, Kirchheim unter Teck, Germany
Graupner E-PROPS 13x4	Graupner/SJ GmbH, Kirchheim unter Teck, Germany
UniLog2	SM Modellbau, Wielenbach, Germany
GPS-Logger 2	SM Modellbau, Wielenbach, Germany
Thermocouple	
- AD597	Analog Devices, Norwood, MA, USA
- AD627	Analog Devices, Norwood, MA, USA
- CHAL-003	Omega Engineering, Deckenpfronn, Germany
- TSRN-1SM Series	Traco Power, Ismaning/München, Germany
CSmicro LT02	Optris GmbH, Berlin, Germany
LinPicco A05 with P14	Innovative Sensor Technology IST AG, Ebnat-Kappel, Switzerland

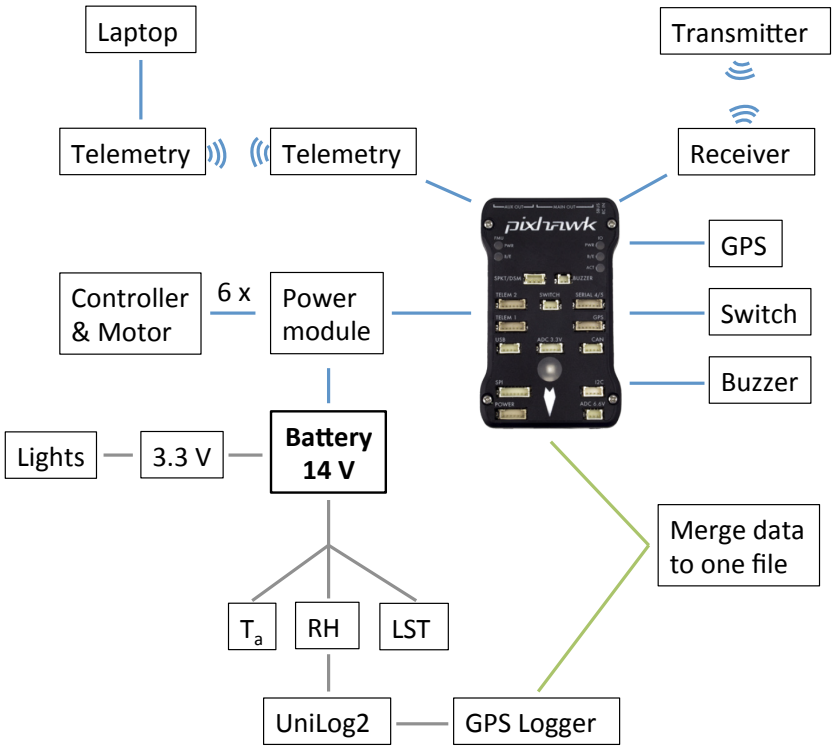

Fig. A1: Flight control connections in blue, sensor connections in grey and merging of data output in green with T_a = Air temperature, RH = relative humidity, LST = land surface temperature. Merging of data files is done with the R-script in "A2 Hexacopter Software".

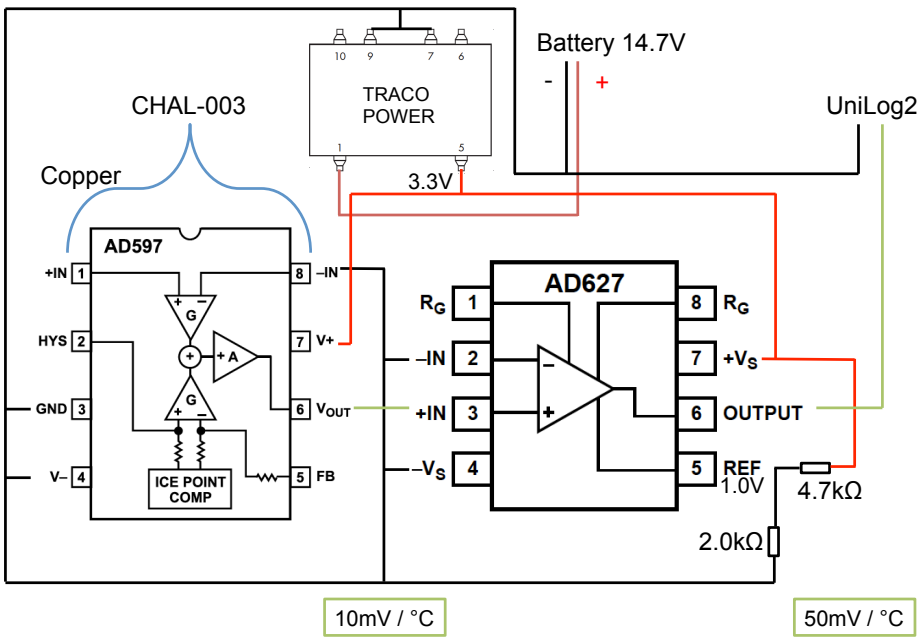

Fig. A2: Circuit diagram of the thermocouple. The used parts are specified in Tab. A1; the colors indicate connections while black is ground (-), red is + with 3.3 V and darkred is + with 14.7 V, green is output in mV, blue are the two different wires, black quadrangles represent resistors.

A2 Hexacopter Software

```
### Merge data files from pixhawk and GPS Logger
## Whenever "..." occurs the working directory has to be
    specified
setwd("...")
####### read Pixhawk
pixlist = system("ls *.log", intern=TRUE)
for (m in 1:2) # numbers depending on number of files in
    pixlist
{
setwd("...")
x = read.table(pixlist[m], skip=605, fill=TRUE, header=FALSE,
    sep=",")

# sort data and save in list, not all specified parameters
    are used for analysis
param = c("GPS","IMU","ACC1","ACC2","GYR1","GYR2","RCIN","
    RCOU","BARO","POWR","AHR2","EKF1","EKF2","EKF3","EKF4","
    CURR","MAG","MAG2","ATT","EV","PM","MODE","CTUN")
param_list = list()

for (i in param)
{
  param_list[[i]] = x[which(x$V1 == i),]
}

# Edit data: merge important parameters
####### GPS ##############################
v2 = as.matrix(param_list$GPS)
v2 = as.numeric(v2[,2])
len = length(v2[v2==1])
param_list$GPS = param_list$GPS[-c(1:len),]
num = param_list$GPS[,14]
num = round(num/1000, digits=0)
ap=ISOdatetime(1980,1,6,0,0,0, tz = "UTC")
week = param_list$GPS[,4]*7*24*3600
time = week + param_list$GPS[,3]/1000 + ap - 17 # UTC = GPS
    -17
date = format(time, "%d.%m.%Y")
time = format(time, "%H:%M:%S")
```

```
time = as.character(time)
TIME = unique(time)
char = as.character(param_list$GPS[,1])
param_list$GPS = cbind(char, time, param_list$GPS[,4:12],num
    )
colnames(param_list$GPS) = c("Param","time","Week","NSats","
    HDop","Lat","Lng","RelAlt","Alt","Spd","GCrs","TimeMS")
GPS = aggregate(param_list$GPS,by =list(param_list$GPS[,12])
    ,mean)
TIME = unique(time)
GPS = cbind(TIME[1:nrow(GPS)],GPS[,c(5:13)])

###### ATTITUDE ##############################
param_list$ATT = param_list$ATT[-c(1:len),c(1:10)]
char = as.character(param_list$ATT[,1])
num = as.character(param_list$ATT[,2])
num = as.numeric(num)
num = round(num/1000, digits=0)
param_list$ATT = cbind(char, num, param_list$ATT[,3:10])
colnames(param_list$ATT) = c("Param","TimeMS","DesRoll","
    Roll","DesPitch","Pitch","DesYaw","Yaw","ErrRP","ErrYaw")
ATT = aggregate(param_list$ATT,by=list(param_list$ATT[,2]),
    mean)

###### BARO ##############################
param_list$BARO = param_list$BARO[-c(1:len),c(1:6)]
char = as.character(param_list$BARO[,1])
num = as.character(param_list$BARO[,2])
num = as.numeric(num)
num = round(num/1000, digits=0)
Press = round(param_list$BARO[,4]/100,digits=1)
param_list$BARO = cbind(char, num, param_list$BARO[,3],Press
    ,param_list$BARO[,5:6])
colnames(param_list$BARO) = c("Param","TimeMS","Alt","Press"
    ,"Temp","CRt")
BARO = aggregate(param_list$BARO,by=list(param_list$BARO
    [,2]),mean)

###### RCIN ##############################
param_list$RCIN = param_list$RCIN[-c(1:len),]
char = as.character(param_list$RCIN[,1])
```

```
num = as.character(param_list$RCIN[,2])
num = as.numeric(num)
num = round(num/1000, digits=0)
param_list$RCIN = cbind(char, num, param_list$RCIN[,4:14])
colnames(param_list$RCIN) = c("Param","TimeMS","C1-roll","C2
    -thr","C3-pit","C4-mode","C5-yaw","C6","C7","C8","C9","
    C10","C11")
RCIN = aggregate(param_list$RCIN,by =list(param_list$RCIN
    [,2]),mean)
RCIN = cbind(RCIN[,c(1:3)],round(RCIN[,c(4:8)],digits = 0),
    RCIN[,c(9:14)])

###### CURRENT ##############################
param_list$CURR = param_list$CURR[-c(1:len),c(1:8)]
char = as.character(param_list$CURR[,1])
num = as.character(param_list$CURR[,2])
num = as.numeric(num)
num = round(num/1000, digits=0)
param_list$CURR = cbind(char, num, param_list$CURR[,3:8])
colnames(param_list$CURR) = c("Param","TimeMS","ThrOut","
    ThrInt","Volt","Curr","Vcc","CurrTot")
CURR = aggregate(param_list$CURR,by =list(param_list$CURR
    [,2]),mean)

###### RCOU ##############################
param_list$RCOU = param_list$RCOU[-c(1:len),c(1:10)]
char = as.character(param_list$RCOU[,1])
num = as.character(param_list$RCOU[,2])
num = as.numeric(num)
num = round(num/1000, digits=0)
param_list$RCOU = cbind(char, num, param_list$RCOU[,3:10])
colnames(param_list$RCOU) = c("Param","TimeMS","Chan1","
    Chan2","Chan3","Chan4","Chan5","Chan6","Chan7","Chan8")
RCOU = aggregate(param_list$RCOU,by =list(param_list$RCOU
    [,2]),mean)

###### EKF 1 ############################## Velocity, Position,
    Gyro bias
param_list$EKF1 = param_list$EKF1[-c(1:len),c(1:14)]
char = as.character(param_list$EKF1[,1])
num = as.character(param_list$EKF1[,2])
```

```
num = as.numeric(num)
num = round(num/1000, digits=0)
param_list$EKF1 = cbind(char, num, param_list$EKF1[,3:14])
colnames(param_list$EKF1) = c("Param","TimeMS","ERoll","
    EPitch","EYaw","VN","VE","VD","PN","PE","PD","GX","GY","
    GZ")
EKF1 = aggregate(param_list$EKF1,by=list(param_list$EKF1
    [,2]),mean)

####### combine all parameters
total = cbind(GPS,ATT[1:nrow(GPS),],BARO[1:nrow(GPS),],RCIN
    [1:nrow(GPS),],RCOU[1:nrow(GPS),],CURR[1:nrow(GPS),],EKF1
    [1:nrow(GPS),])
total = cbind(date[1:nrow(GPS)],TIME[1:nrow(GPS)],total[,c
    (2:9,14:21,25:27,32:36,46:51,58:62,66:68)])
colnames(total) = c("Date","Time","NSats","HDop","Lat","Lng"
    ,"RelAlt","Alt","Spd","GCrs","DesRoll","Roll","DesPitch",
    "Pitch","DesYaw","Yaw","ErrRP","ERRYaw","Alt_baro","Press
    _baro","Temp_baro","C1-roll","C2-thr","C3-pit","C4-mode",
    "C5-yaw","Rotor1","Rotor2","Rotor3","Rotor4","Rotor5","
    Rotor6","ThrInt","Volt","Curr","Vcc","CurrTot","ERoll","
    EPitch","EYaw")

####### GPS Logger
setwd("...")
ulist = system("ls␣*.txt", intern=TRUE)
ulog = read.table(ulist[m],header=FALSE,fill=TRUE,sep="\t",
    skip=1)
ulogs = ulog[1:c(nrow(ulog)-2),c
    (1:9,16:18,28:30,33:34,40:42,49:50)]     #subset the
    important columns
colnames(ulog) = c("Datum","Zeit","Geschwindigkeit","Hoehe␣
    NN","lat","Lon","Richtung","Hoehe","Steigen","X","Y","Z",
    "UL2␣Datum","UL2␣Uhrzeit","UL2␣Logzeit","UL2␣Hoehe␣ueber␣
    Start","UL2␣Steigen","Ta","Td","Ts","UL2␣Luftdruck","UL2␣
    interne␣Temperatur")
ta = 1.0432*((ulogs$Ta/1000-0.978)/0.05)+0.4899 #
    calculation of temperature
rh = 100/5000*ulogs$Td # calculation of humidity
ts = ulogs$Ts/10 # calculation of LST
Time_ul = substr(ulogs$Zeit, start=1, stop=8)
```

```
ti = strptime(Time_ul, "%H:%M:%S")-7200    #standard time:
    -3600, daylight saving time: -7200
Time_ul = substr(ti, start=12,stop=20)
ulogs = cbind(ulogs[,1],Time_ul,ulogs[,3:ncol(ulogs)],ta,rh,
    ts)
unilogs = aggregate(ulogs[,3:ncol(ulogs)],by=list(ulogs[,2])
    ,mean)

####### UniLog and Pixhawk
both = merge(total, unilogs, by.x=c("Time"),by.y=("Group.1")
    ,all=TRUE,sort=TRUE)
setwd("...")
write.table(both,file=paste(pixlist[m],".txt",sep=""),col.
    names = TRUE, row.names=FALSE, sep=",")
}
```

A3 Hexacopter Flights and Data

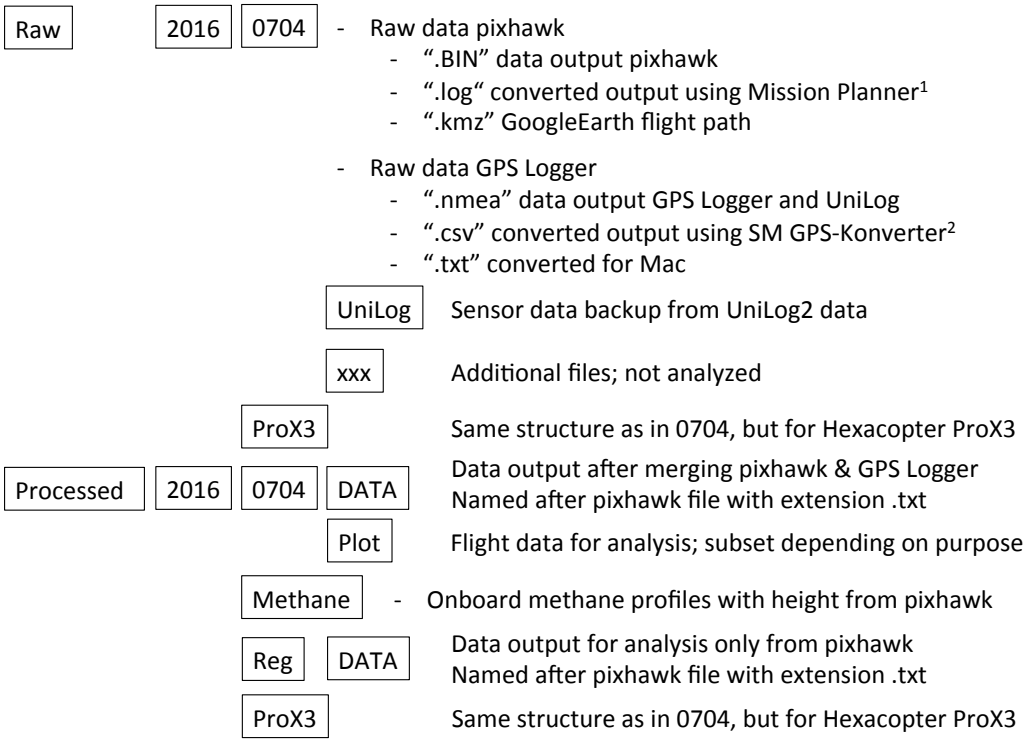

[1] https://www.sm-modellbau.de/PC-Software
[2] http://ardupilot.org/planner/docs/common-install-mission-planner.html

Fig. A3: Data structure of hexacopter flights during ScaleX 2016 with folders presented in frames and files with "-". "Readme" files are included in the folders. Access upon request. Unless stated otherwise, data is derived from hexacopter F550; data in folder "Pro X-3" is from the hexacopter Pro X-3 Lite. Data from ScaleX 2015 is also available upon request with data structure specified separately in a Readme file.

Tab. A2: Hexacopter flights during ScaleX campaign 2016. * means data were analyzed and included in the thesis. Abbreviations stand for: hor = Horizontal flight path, forest = Comparison between forest and grassland, profile = vertical profile up to 150 m, methane = vertical profiles for methane investigations with both hexacopters.

Date	**Time in UTC**	**Flight**	**Pixhawk**	**UniLog**	
04.07.16	16:09	Forest	415	24	
05.07.16	13:35	Hor 5 m	422	30	*
	13:46	Hor 10 m	423	31	*
	14:00	Hor 15 m	425	33	
06.07.16	13:20	Hor 5 m	426	34	*
	14:01	Profile	427	35	
	14:11	Forest	428	36	
	14:36	Hor 5 m	430	38	*
	15:02, 15:05	Profile, forest	431	39	
	16:28	Hor 5 m	432	40	*
	16:39	Hor 10 m	433	41	*
	16:48	Hor 15 m	434	42	*
	18:08	Methane	436	44	*
	19:08	Methane	438	46	*
	20:07	Methane	440	48	*
	21:00	Methane	441	49	*
	22:00	Methane	442	50	*
	23:07	Methane	443	51	*
	00:01	Methane	445	53	*
	01:01	Methane	446	54	*
	02:00	Methane	448	56	*
	03:00	Methane	449	57	*
	04:00	Methane	450	58	*
08.07.16	08:51	Hor 5 m	453	60	*
	09:01	Hor 10 m	454	61	*
	09:12	Hor 15 m	456	63	*
	10:00, 10:06	Profile, forest	457	64	
	10:48	Hor 5 m	458	65	*
	10:58	Hor 10 m	459	66	*
	11:07	Hor 15 m	460	67	*
	13:04, 13:10	Profile, forest	461	68	
11.07.16	07:11, 07:17	Profile, forest	463	69	
	07:34	Hor 5 m	464	70	*
	08:44	Hor 10 m	471	77	*
	08:55	Hor 15 m	472	78	*
	09:33	Hovering 9m	473	79	*
	11:01	Hor 5 m	474	80	*
	11:12	Hor 10 m	475	81	*
	11:52	Hor 15 m	477	83	*
	12:58	Forest	480	86	